Environments of Active Galaxies Over Cosmic Time

Elizabeth Frances Dodd

STRI

University of Hertfordshire

A thesis submitted for the degree of

Doctor of Philosophy

Supervisors: Prof. Martin Hardcastle, Prof. Matt Jarvis and Dr. Dan Smith

Acknowledgements

I am also very grateful to all of my friends in the STRI that have been there for me through the good and hard times. You have all made the PhD one of the most pleasant experiences of my life and I shall look back on it with fond memories.

I especially thank my family that have always supported me throughout my doctorate and have always encouraged me to follow my dreams and never ever give up. I would not be here today if it was not for your support in my academic success.

Finally, I want to say a special thank-you to my fiance, Ian Greenslade, who has always been there for me. You have supported me with your love, understanding and many home cooked meals!

Abstract

The overall aim of this thesis is to investigate the environments of AGN, in particular, the density of galaxies in the environments of radio-loud and radio-quiet AGN. This determines whether AGN trace dense environments at high redshifts and whether the environments are important in addressing the problem of radio-loud dichotomy. I extend my research by investigating whether star-formation evolves differently in high-redshift AGN environments compared to the field.

I begin by investigating the environments of 169 AGN using Spitzer data at $z \sim 1$. I investigate the source density of star-forming galaxies in the environments of radio galaxies, radio-loud quasars and radio-quiet quasars. I do not find any significant overdensity of star-forming galaxies in these environments, although I find tentative evidence for a difference in the colours of galaxies in the radio galaxy environments compared to the quasar and field environments.

I next use VIDEO data to investigate the environments of the quasars out to $z \sim 3$. Firstly, I use a training sample of QSOs and galaxies, which trains a neural network to detect QSOs in the VIDEO data. I detect 274 possible QSOs in the VIDEO data using this method. I am able to determine that the efficiency of the neural network classification is 95 per cent using the training sample. I compare these

results to a colour selection method, which detects 88 QSOs in the VIDEO data, and find that the neural network is able to detect ~ 80 per cent of the colour selected QSOs at $K_s = 21$.

I then investigate the source overdensity using a radial analysis on the environments of the VIDEO QSOs. I find a significant overdensity of galaxies in the environments of the whole QSO sample and in the environments of the radio-loud quasars compared to the radio-quiet quasars. I extend the density analysis by using a second density measure, called the spatial clustering amplitude technique, to compare the environments of the quasars with their radio luminosities, absolute magnitudes and redshifts. I do not find any significant correlations between environmental density and radio luminosity, absolute magnitude or redshift for the QSOs. I extend this research to investigate the type of galaxies found in the AGN environments. However, I do not find any significant differences between the type of galaxies found in the QSO environments and the background field.

Contents

List of Figures

List of Tables

Chapter 1

Introduction

1.1 History of Active Galactic Nucleus Observations

Active Galactic Nuclei (AGN) were first discovered by E. A. Fath in 1908 (Fath, 1909). He found the presence of strong emission lines in the galaxy NGC 1068 and commented on the fact that they were similar to those seen in planetary nebulae. However, it was not until the 1940s that more of this type of galaxy were found by Carl Seyfert (Seyfert, 1943). He found that some spiral galaxies had extraordinarily bright and point-like nuclei, which at first he thought were stars at the centre of the galaxies. Spectroscopic studies revealed that these objects possessed strong and broad emission lines in their spectra, which are from highly excited ionized gas at the centres of the galaxies.

Major advances came with construction of the first radio telescopes in the 1940s and 50s. Though the resolution of these early radio telescopes was low, it

was good enough to allow strong radio sources to be identified with individual optical objects, such as galaxies and star-like sources. One of these identifications was Cygnus A, a radio source found near a galaxy, which Baade & Minkowski (1954) found to have a redshift of 0.05. This type of AGN became known as a radio galaxy (RG).

Other radio sources that were identified were point-like objects or "quasi-stellar radio sources" which were later called quasars (Osterbrock & Bochkarev, 1989). These quasars were first identified as extragalactic sources by Schmidt in 1963 (Schmidt 1963; Schmidt et al. 1978). They were found to be highly luminous in the radio and very bright at X-ray wavelengths.

These discoveries had wide implications for the study of extragalactic astronomy. Massive black holes were first suggested to be associated with AGN by Zel'dovich & Novikov (1964) and the role AGN had in galaxy formation and evolution was first discussed by Burbidge et al. (1963). As quasars were found to be highly luminous, it was realised that they could be used as cosmological probes because they could be detected out to large distances (Hewitt & Burbidge, 1993). Between these early years and today, a vast amount of observational and theoretical work has been put into understanding the nature of these objects. This understanding will be summarised in the following sections.

1.2 Evidence for Black Holes

It was proposed early on in the study of AGN that their power source might be accretion onto a supermassive black hole (SMBH, Salpeter 1964; Zel'dovich & Novikov 1964; Lynden-Bell 1969). However, there are no direct observations of

black holes. Therefore to detect them astronomers must look at the impact that black holes have on their surroundings. One method of detecting a black hole is to use our own galaxy, the Milky Way, to see if a SMBH resides at the centre. For this astronomers require the detection of radial velocities, proper motions and accelerations of stars on small scales. There is strong evidence that at the centre of our galaxy there is a black hole with M $\sim 3 \times 10^6$ M$_\odot$ within a radius of < 10 light years which is centered on the radio source Sgr A* (Genzel et al. 2000; Schödel et al. 2003; Ghez et al. 2005). The only plausible explanation for this excess mass in the centre of the Milky Way is that there is a SMBH residing there. Unless our own galaxy is special, we would expect to find that SMBHs also reside in other galaxies.

Beyond the Milky Way, Magorrian et al. (1998) examined the mass-to-light ratios of stars in 32 galaxy bulges and found that a substantial massive dark object (MDO) was required in order for their models to reproduce the observed kinematics. They found that 97 per cent of their galaxy sample (36 galaxies) had a MDO at their centres and that the mass of the black holes correlated with the bulge of the galaxies (M$_{\mathrm{Bh}} \sim 0.006M_{\mathrm{bulge}}$), a correlation which is now known as the Magorrian relation.

1.3 Physical Properties of AGN

1.3.1 Structure of AGN

From the Magorrian relation we know that there are probably black holes found in the centre of all galaxies; however, not all galaxies are active. It is thought

to be the accretion disk that accretes material onto the black hole which creates the active nucleus. The structure of an AGN in the standard model is shown in Figure 1.1.

In the standard model the SMBH is surrounded by a thin hot accretion disk which heats up and the inner parts become a source of thermal emission with temperatures of $\sim 10^5$ K (Chen & Halpern, 1989). Just beyond the SMBH and accretion disk lies the broad line region (BLR) (Osterbrock & Mathews 1986; Nicastro 2000). This is the region where clouds of dust and gas which orbit the black hole are being ionised by the continuum from the accretion disk. They show broad absorption lines because the gas will have a spread of velocities along the line of sight which causes the spectral lines to appear broadened. See Figure 1.2 for a representative spectrum of a broad-line quasar.

It has been suggested (e.g. by Antonucci 1993) that surrounding the accretion disk there is a large dusty torus, which consists of high-density clouds that contain $\sim 10^9$ $M_\odot$ of dust and molecular gas, most of which will be comparatively hot ($\sim$ 1000K) (e.g Krolik & Begelman 1988; Nenkova et al. 2002; Deo et al. 2011). The torus abscures the broad lines and direct optical continuum from the AGN along lines of sight that pass through the torus. This model is supported by observations of broad lines revealed by optical spectropolarimetry and near-infrared spectroscopy in objects that do not show direct broad lines in the optical (e.g Goodrich & Cohen 1992): these observations show that the broad lines are intrinsically present but obscured rather than being intrinsically missing. Other evidence for the existence of the torus is provided by direct observational searched in the mid infrared (e.g. Burtscher et al. 2013).

The gas further out from the dusty torus is in the region called the Narrow-

Line Region (NLR) (Netzer & Laor, 1993). This gas does not show broad lines because the clouds are further away from the SMBH and therefore travel at slower orbital velocities. In the torus model, this material is not obscured because it is outside of the torus and so can be observed, see Section 1.6 for further details.

1.3.2 Properties of SMBHs

One method of constraining the properties of SMBHs in AGN is reverberation mapping (Blandford & McKee, 1982; Peterson, 1993). This estimates the mass of the SMBH using the variability of the optical continuum, which is generated in the accretion disk, and the time delay for photons to reach the BLR. From the emission line width of the emission-line clouds, in the broad-line regions, the velocity dispersions can be determined. Using the time delay and velocity dispersion the mass of the black hole can be estimated (Kaspi et al. 2000; Bentz et al. 2009).

Following the $M_{Bh} \sim M_{bulge}$ relation for galaxies (Magorrian et al., 1998) we would expect there to be a similar relation for AGN. McLure & Dunlop (2002) find that the black hole mass and bulge relation is $M_{Bh} = 0.0012\,M_{bulge}$ for a sample of 72 AGN, using reverberation mapping and stellar velocity dispersions to estimate the mass of the black holes. The velocity dispersion technique uses the correlation between the black hole mass and the stellar velocity dispersions for the stars in the galaxy, which is called the $M_{bh} - \sigma$ relation. McLure & Dunlop (2002) find that their black hole mass and bulge relation for their AGN sample is consistent with the relation found by Merritt & Ferrarese (2001), who used the same 32 inactive galaxies in the Magorrian sample and used the same velocity dispersion
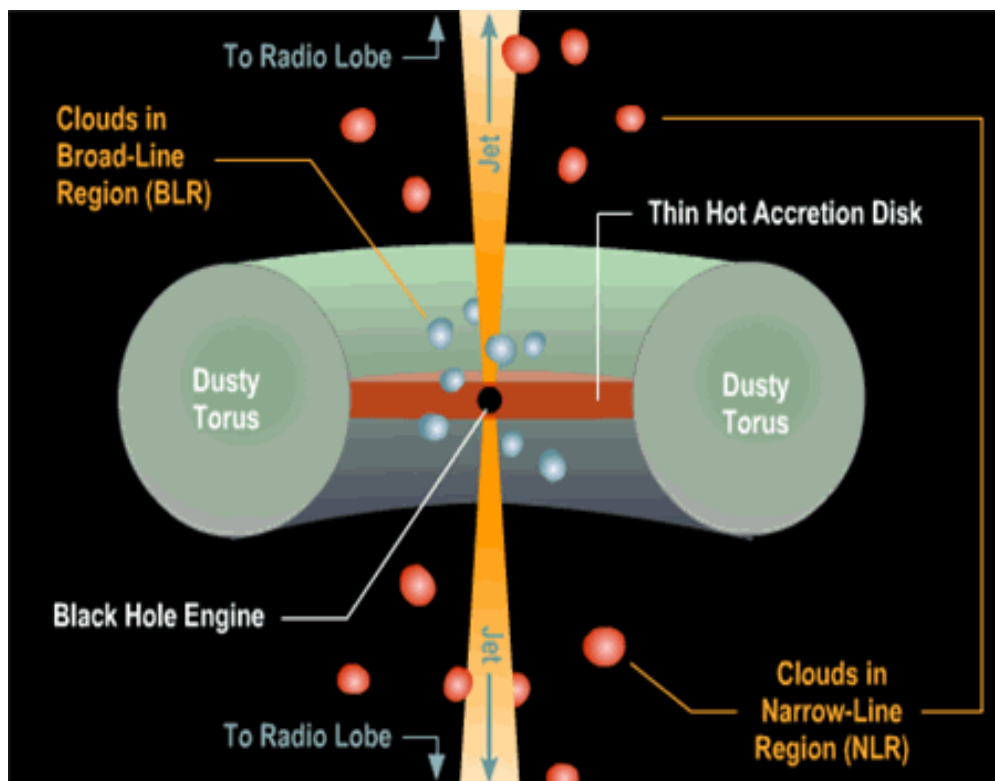
Figure 1.1: An illustration of the structure of an AGN. Image credit: Brooks/Cole Thomson Learning.
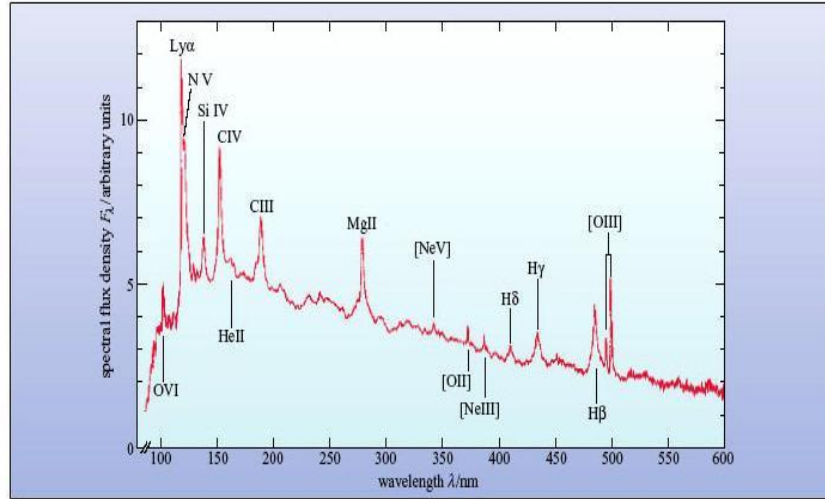
Figure 1.2: An average optical QSO spectrum that shows the broad emission lines of more than 700 quasars from the Large Bright Quasar Survey (Francis et al., 1991).

technique as McLure & Dunlop (2002). This is further evidence that SMBHs are found at the centres of active galaxies, supporting the picture presented in Section 1.2.

1.3.3 The Eddington limit and black hole masses

There is an upper limit on the accretion rate of black holes, called the Eddington luminosity, L_{Edd} (Rees, 1984). This is the maximum luminosity that can be produced by the AGN without the radiation pressure from the AGN causing the accreting gas to be dispersed. If the luminosity was greater than the Eddington

limit the radiation pressure on the electrons in accreting hydrogen atoms would be greater than the gravitational force which would cause the accretion to cease.

The radiation pressure depends directly on the luminosity and falls off as the inverse square of the distance from the accretion disk (Mo et al., 2010). The radiation force on the gas due to the scattering of photons by electrons is

$$F_{rad} = L\sigma_T/4\pi r^2 c, \tag{1.1}$$

where L is the luminosity, σ_T is the Thompson interaction cross-section, r is the distance from the object to the accretion disk and c is the speed of light.

The gravitational force on the corresponding nucleus is

$$F_{grav} = GM_{BH}m_p/r^2 \tag{1.2}$$

where G is the gravitational constant, M_{BH} is the black hole mass, m_p is the proton mass and r is the radius between the black hole and the proton. By equating and rearranging these equations the Eddington luminosity is

$$L_{Edd} = GM_{BH}m_p 4\pi c/\sigma_T = 1.28 \times 10^{46} \, (M_{BH}/10^8 \, M_\odot) \, \text{erg s}^{-1}. \tag{1.3}$$

To find the minimum M_{BH} for a given luminosity the above equation can be inverted

$$M_{Edd} = 8 \times 10^7 \, (L/10^{46} \, \text{erg s}^{-1}) \, M_\odot. \tag{1.4}$$

A highly luminous black hole accretion system with L $\sim 10^{46}$ erg s^{-1} which

radiates at the Eddington limit has a mass of $M_{BH} \sim 10^8$ $M_\odot$, if it is radiating below the Eddington limit its mass must be even larger.

1.3.4 Accretion Rates

The energy available from a mass M is $E = \eta Mc^2$, which can be converted into energy E at an efficiency η. The rate at which energy is supplied by accretion is $L = \eta \dot{M}c^2$, where $\dot{M}$ is the mass accretion rate ($\dot{M} = dM/dt$). To calculate the rate at which the potential energy of infalling material can be converted to radiation we can use

$$L = \frac{dU}{dt} = \frac{GM}{r}\frac{dm}{dt} = \frac{GM_{BH}\dot{M}_{BH}}{r}, \qquad (1.5)$$

where $\dot{M}_{BH}$ is the accretion rate of the black hole and $U = GMm/r$ is the potential energy of mass m at distance r from the central source of mass M.

The highest possible mass accretion rate corresponds to the Eddington luminosity, i.e.

$$\dot{M}_{Edd} = L_{Edd}/\varepsilon_r c^2 \approx 2.2 \ (M_8) \ M_\odot yr^{-1}, \qquad (1.6)$$

where M_8 corresponds to a black hole mass of 10^8 $M_\odot$ and ε_r corresponds to the fraction of mass converted to energy.

If we have a black hole with $M_{Bh} \sim 10^8$ $M_\odot$ and we want it to radiate at 10^{46} erg/s, a typical bolometric luminosity of an active galaxy (Osterbrock, 1991), the mass needs to accrete at the Eddington rate, i.e. ~ 2 $M_\odot yr^{-1}$ for $\varepsilon_r = 0.1$. For a less luminous AGN with $L \sim 10^{44}$ erg/s (Comastri, 2004) the mass of the black hole would be $M_{Bh} \sim 10^6$ $M_\odot$, assuming accretion at Eddington, requiring

0.02 $M_\odot yr^{-1}$ of accretion.

1.4 Optical Classification of AGN

AGN are spectroscopically classified either as Type 1 or Type 2 AGN. Type 1 AGN have broad and narrow emission-line regions in their spectra, whilst Type 2 AGN only exhibit narrow emission lines in their spectra.

1.4.1 Seyfert galaxies

Seyferts are AGN that have low nuclear luminosities, which means that the host galaxies are clearly detectable. The accepted criterion is $M_B > -23$ for a Seyfert galaxy (Schmidt & Green, 1983) or $L_B < 10^{44}$ ergs^{-1} (Whittle, 2000); if the object was more luminous than this it would be classed as a quasar. Seyfert galaxies (Seyfert, 1943) were first observed to have two distinct classes by Khachikian & Weedman (1974). They are classified either as Type 1 Seyferts, if narrow and broad lines are detected in their spectra, or as Type 2 Seyferts, if only narrow lines are detected.

1.4.2 LINERs

A possible type of AGN are the Low Ionization Nuclear Emission Regions (LINERs) which were first identified by Heckman (1980). These are very low-luminosity Seyfert galaxies and spectroscopically similar to Seyfert 2s, except that their low-ionization lines are very strong. However, whether LINERS are in fact AGN that are powered by black hole accretion has been under debate. LINERs could also be generated via photoionzation by normal main-sequence stars (Filippenko &

Terlevich, 1992; Shields, 1992) and more recently, Alonso-Herrero et al. (2000) found many LINERS could be aging starbursts. These indicate that they are not always powered by black holes and it is debatable whether they are all part of the AGN classification scheme.

1.4.3 Quasars

Quasars are the most optically luminous class of AGN with luminosities $M_B < -23$ (Schmidt & Green, 1983) and can outshine their host galaxy. They are typically hosted by massive elliptical galaxies with scale lengths of ~ 10 kpc (McLure et al., 1999). They typically have black hole masses $M_{bh} > 10^8 M_\odot$ with the most radio-loud QSOs exceeding black hole masses of $M_{bh} > 10^9 M_\odot$ (Dunlop et al., 2003). (The radio properties of QSOs will be discussed in the following section.) They have very broad optical emission lines, which are also found in Seyfert 1 galaxies (Robson, 1996). See Figure 1.2 for a typical quasar spectrum.

1.4.4 BAL quasars

Broad Absorption Line quasars (BAL) are a sub-type of quasars which show broad absorption lines. These show evidence of high Doppler broadening (Robson, 1996) which indicates that there is a massive amount of material from the quasar in the form of outflows (Hopkins et al., 2008). These typically have broad absorption lines of 1000 kms^{-1} (Charlton & Churchill, 2000). These can be either from gas near the quasar's central engine or from gas which is unrelated to the quasar, situated along the line-of-sight between the quasar and the observer.

1.4.5   Radio galaxies

Radio galaxies exhibit extended, twin-lobed radio emission which can extend beyond the central galaxy out to Mpc distances (Archibald et al., 2001; Page et al., 2001). They can be classified depending on their optical spectra (Heckman 1980; Baldwin et al. 1981), into either high-excitation radio galaxies (HERGs) or low-excitation radio galaxies (LERGs) (Hine & Longair 1979; Laing et al. 1994; Hardcastle et al. 2013). HERGs are found to have highly excited lines, such a [OIII], [NII] and [MgII] in their spectra and an equivalent width (EW) of [OIII] > 5Å (Hardcastle et al., 2013). HERGs are brighter than LERGs by a factor of $\approx$ 10 in the [OIII] line (Buttiglione et al., 2010). The differences between these RGs could be from different methods of fueling, such as cold or hot gas accretion. LERGs are thought to be fueled by hot gas halos of their host ellipticals and are found at lower redshifts, whilst HERGs are fueled by cold gas which could be from mergers and are found at higher redshifts (Hardcastle et al., 2007).

HERGs can be split up into two spectroscopic classifications; they are either broad-line radio galaxies (BLRGs, Kataoka et al. 2011) or narrow-line radio galaxies (NLRGs, Sikora et al. 2013). The BLRGs have broad and narrow-line emission lines compared to the NLRGs, which only have narrow-line emission lines (Hine & Longair, 1979).

RGs can also be classified in terms of their radio power and morphology, and this will be discussed in detail in Section 1.5.

1.4.6 BL Lacs and OVVs

Most AGN show some form of continuum variability but a small proportion of them show short time-scale variations. These sources are usually called blazars. Historically, blazars can be categorized into two sub types; one called Optically Violently Variable quasars (OVVs) and the other called BL Lacertae objects (BL Lac). The OVVs exhibit broad optical emission lines, whilst BL Lacs do not (Antonucci, 1993).

1.5 Radio Classification of AGN

1.5.1 Radio Loud and Radio Quiet AGN

As well as classifying AGN depending on their optical properties we can also classify them depending on the amount of radio emission they show: traditionally they are classified as radio loud AGN (RL) and radio quiet AGN (RQ). These types are found in different proportions; there are fewer radio-loud AGN ($15 - 20$ per cent, Kellermann et al. 1989) than radio-quiet AGN.

The radio emission is produced by electrons travelling at relativistic velocities and interacting with a magnetic field, which cause the electrons to lose energy and emit in the radio regime. This process is called synchrotron emission: in radio-loud objects, extended lobes are fed by jets of relativistic electrons which originate at the accretion disk (Chiaberge et al., 1999; Tregillis et al., 2001).

There are two methods of classifying AGN either as radio-loud or radio-quiet. One method is to define a radio luminosity boundary to select radio-loud and radio-quiet AGN. However, this method does not account for the radio lumi-

nosity being dependent on black hole mass. The larger the black hole mass the more radio luminous the AGN would be (McLure & Jarvis, 2004). Using a radio luminosity boundary also introduces selection effects due to the flux-density limits of radio surveys, especially at high redshifts. Another method to select radio-loud or radio-quiet AGN is to classify them depending on their ratio of radio to optical flux. Ivezić et al. (2002) use the criterion $R_i = \log(F_{radio}/F_i)$ where radio-loud quasars have $R_i > 1$ and radio-quiet quasars have $R_i < 1$. The F_{radio} and F_i are observed flux densities measured at 1.4 GHz and in the i-band respectively. However, the ratio of radio and optical flux measures can introduce selection effects and bias because the optical flux is susceptible to internal extinction (Zamfir et al., 2007). There is still no current agreed definition for selecting radio-loud and radio-quiet AGN and many authors use different selection criteria for radio-loudness.

Possible reasons for the observed dichotomy in radio type could be that it is due to the environments affecting radio-loudness (Falder et al., 2010), or that the spin of the black hole is higher for RL AGN (Sikora et al., 2007; Volonteri et al., 2007a). There are studies that question whether there are two distinct radio populations of AGN (Lacy et al. 2001; Cirasuolo et al. 2003): these suggest that rather than having a parameter that turns on powerful radio jets, there is a continuous variation of radio luminosity with black hole mass. There is also evidence that the two radio types might actually be two different populations of AGN that go through a radio-loud and then a radio-quiet phase (White et al., 2007; Zamfir et al., 2008).

1.5.2   Radio Structures

There are two radio classes of radio-loud AGN, lobe-dominated and core-dominated. The lobe-dominated RGs and radio-loud quasars consist of two extended lobes from the central galaxy (Miley & De Breuck, 2008).

In the lobe-dominated class there are two sub classes, Fanaroff-Riley class I (FRI) and Fanaroff-Riley class II (FRII) (Fanaroff & Riley, 1974). The FRI objects have lower luminosities and the ends of the sources show the steepest radio spectra and are faint (Owen & Ledlow, 1994). The lobes are usually connected to the central galaxy by smooth and continuous double sided jets.

The FRII objects are more powerful radio lobe-dominated sources that radiate $> 10^{33}$ W at cm wavelengths (Black et al., 1992). The steepest radio spectrum is found in the inner regions and the edges show bright knots of emission or "hot spots." The jets are usually single sided, or one is brighter than the other. Lobe-dominated radio-loud quasars tend to have FRII-type radio morphologies.

These two sub classes of radio-loud AGN are generally found in different environments. The FRIIs generally reside in normal, giant elliptical galaxies and are generally not found in rich cluster galaxies, whereas the FRI RGs are hosted in larger and more luminous massive galaxies, which are found in the centres of rich galaxy clusters (Seldner & Peebles 1978; Longair & Seldner 1979). This implies that the two types of RGs are different objects rather than the same object at different orientations.

An example of a FRI RG is the well known Centaurus A RG which is found to be 3.7 Mpc away from us (Tingay et al., 1996). Figure 1.3 shows a composite image of Centaurus A and corresponding X-ray, radio and optical images. The

large twin lobes can be seen easily in the X-ray and radio images.

The core-dominated objects are dominated by strong radio emission from the compact core. These show flat spectra which extend from the highest radio frequencies into the sub-mm. Core-dominated objects generally show a single sided jet that is detected on kpc scales. Many radio-loud quasars are core-dominated, as are OVV QSOs and BL Lacs, which are part of the blazar family.

1.6 Unification theory

The Unification Model (Antonucci, 1993) proposes that there is an orientation-dependent obscuration due to a dusty "torus" with a size scale greater than the BLR but less than the NLR. The BLRs are found between $0.01 - 0.1$ pc from the black hole (Wiita, 2006), whilst the NLRs are found at greater distances from the black hole, usually > 10 pc (Wiita, 2006); the torus must therefore have a size ~ 1 pc. As a consequence of the existence of the torus, the differences we observe in the different optical types of AGN are due to the angle at which we observe them. Figure 1.4 shows how the orientation of the AGN to the observer can change the type definition of the AGN. An interpretation of these different AGN types is that Type 1 AGN are unobscured, so that their accretion disk and broad emission-line region can be viewed directly. Type 2 AGN are obscured and their broad emission line region cannot be viewed directly due to the obscuring torus along our line of sight. This model can explain many of the differences between type 1 and type 2 AGN (Antonucci, 1993).

In addition to the optical classification of AGN, they are also divided by luminosity. Seyfert galaxies have intrinsically lower luminosities compared to
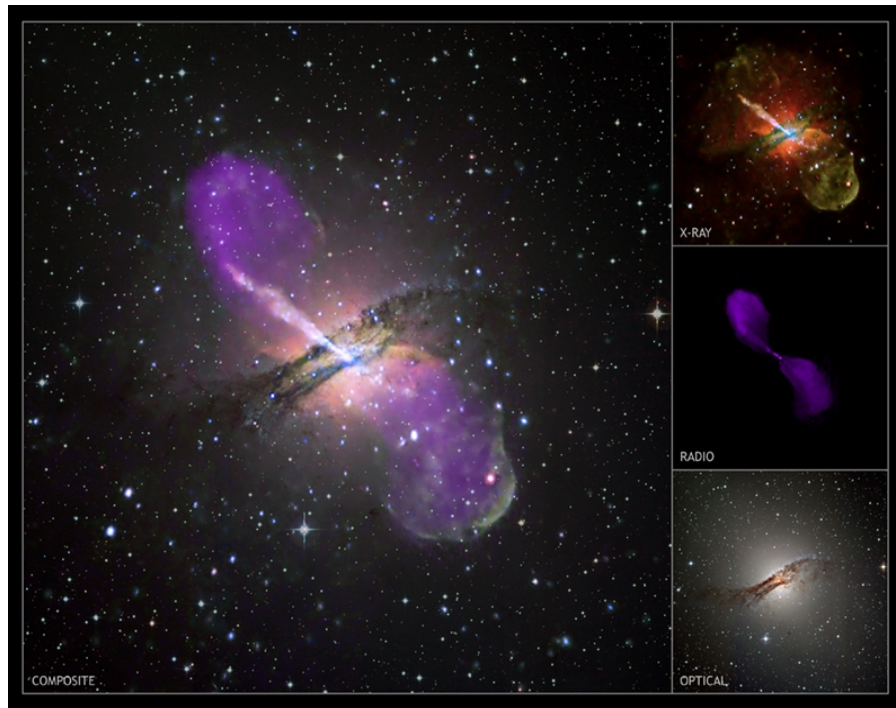
Figure 1.3: A composite image of the radio galaxy Centaurus A and X-Ray, radio and optical images. Credit: X-ray - NASA, CXC, R.Kraft (CfA), et al.; Radio - NSF, VLA, M.Hardcastle (U Hertfordshire) et al.; Optical - ESO, M.Rejkuba (ESO-Garching) et al.

QSOs, which is not explained by their orientation. The differences between their luminosities could be explained by differences in black hole masses, where Seyfert galaxies have lower black hole masses compared to radio-loud QSOs (Wandel, 1999). However, McLure & Dunlop (2001a) find no significant difference between the black hole mass estimates between Seyfert galaxies and QSOs. A possible explanation for their observed differences could be that the high-luminosity QSOs have higher accretion rates (Percival et al., 2001).

Another caveat to the standard model is the discovery of intermediate Seyferts. Osterbrock (1981) found Seyferts, which he called Seyferts 1.8 and 1.9, that have characteristics that fall between the two standard types of AGN. Seyfert 1.8 galaxies show weak broad components of Hα and Hβ and Seyfert 1.9 galaxies show weak broad Hα. In terms of the unified model, Antonucci (1993) suggested that these observations could be explained by the line of sight grazing the outer edge of the dusty torus. However, other studies such as Rudy & Willner (1983) and Goodrich (1995) found that these could be explained by the broad-line clouds having low optical depths and ionizing parameters rather than due to the dusty torus. It is still unclear which of these models is correct, but the fact that objects like intermediate Seyferts exist shows that the standard unification model, in which angle to the ling of sight is the only parameter determining the appearance of an AGN, may well be simplistic.

The Unification picture explains the observed optical properties of the different AGN well; however, the apparent dichotomy between RL and RQ AGN is not explained by the model as low-frequency radio emission is expected to be essentially orientation-independent. Is there a real dichotomy between these types and, if there is, what is causing some AGN to be RL and others to be RQ? Does

the environment have an influence on the radio-loudness or is it due to the black hole spin? Theories other than the Unification Model need to be explored to find whether a true dichotomy exists and if so what the physics behind these observed differences is.

1.7 Galaxy Formation

In this section I explain the main features of current models of galaxy formation in terms of galaxy models and observations, and in particular the relation to AGN activity.

1.7.1 Dark Matter Haloes

Dark matter haloes are important because they are the fundamental building-blocks of structure formation (Press & Schechter, 1974). They are crucial if we want to understand how galaxies are formed and how they evolve to form the most massive galaxies that are seen at the present day.

In the standard model the Universe consists of observable matter (baryonic) and unobservable matter (dark matter). Dark matter was first identified by Zwicky in the early 1930s (Zwicky, 1933). He found that there was a large discrepancy between the expected virial mass compared to the actual amount of detectable (baryonic) mass in clusters. Later on, dark matter was detected using the rotational velocity curves of galaxies (e.g. Persic & Salucci 1995). A rotational velocity curve of NGC 3198 is shown in Figure 1.5 (van Albada et al., 1985). The line with error bars represents the observed rotational curve and the bold lines represent the mass from the disk and halo component of the galaxy. The
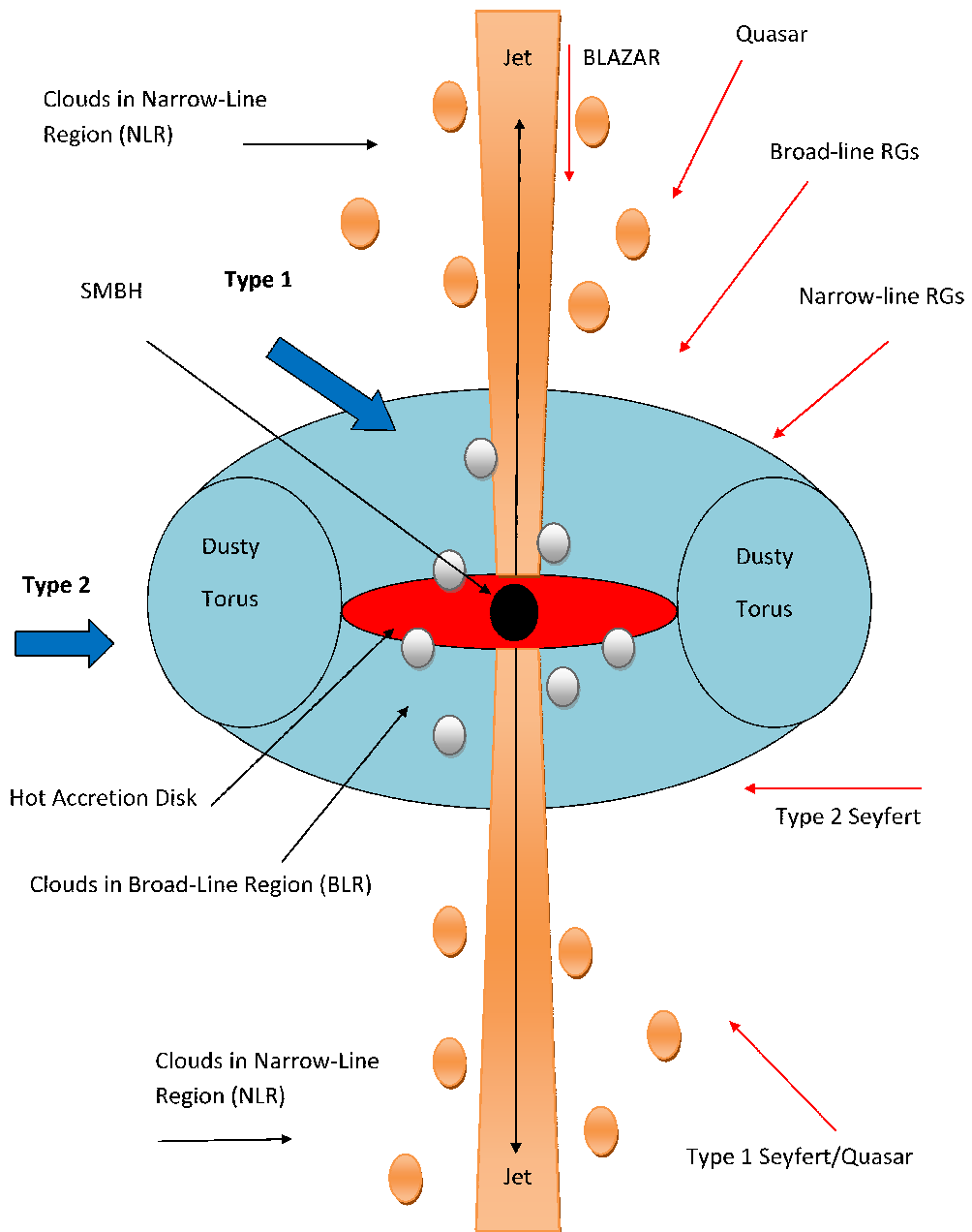
Figure 1.4: This illustration shows the different AGN types and their dependence on orientation (Antonucci, 1993).

discrepancy between the lines, in particular, the disk and the observed rotational curve shows that there must be dark matter present to account for the excess rotational velocity.

These results indicate that another sort of matter was present, which interacted through gravitational forces, but could not be observed directly and was found in large haloes around galaxies (Bertone & Merritt, 2005). Further evidence for dark matter has been indirectly observed through gravitational lensing of galaxies (Kaiser & Squires 1993; Wittman et al. 2000; Melchior et al. 2013) and from X-ray surveys of hot gas in the intra cluster medium (ICM) (Henriksen & Mushotzky 1986; Borgani & Guzzo 2001; Clowe et al. 2006).

1.7.2   Hierarchical Galaxy Formation

Since dark matter was found to be fundamental in the formation of galaxies (see Section 1.7.1) it has been necessary to incorporate it in the models of galaxy formation.

The standard model of galaxy formation is that quantum fluctuations in the early Universe were responsible for small density perturbations (Guth & Pi 1982; Calzetta & Hu 1995; Peiris et al. 2003). Numerical simulations first looked at this process of density perturbations in the early 1980s (Peebles, 1982). The cosmic structures of dark matter haloes were found to grow through the mechanism of gravitational instability, continuing to grow over cosmic time to produce the large scale structure as seen today. Large dark matter haloes grew from smaller dark matter haloes, which merged together; this process is called hierarchical formation or sometimes the "bottom-up" scenario (Lacey & Cole, 1993).
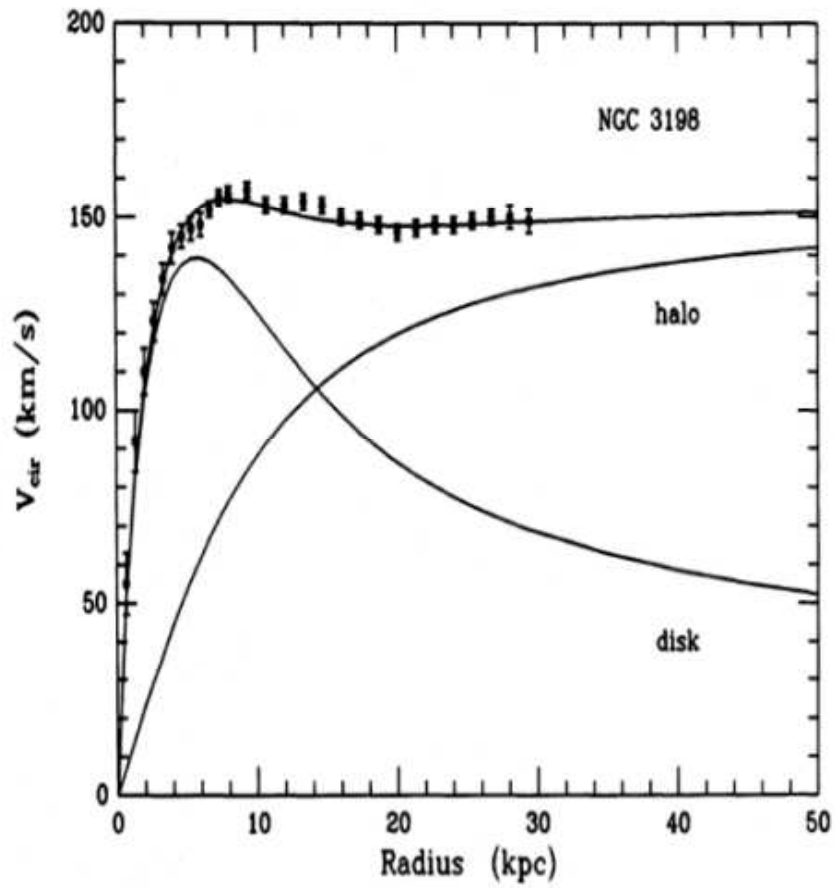
Figure 1.5: A Rotational curve for the distribution of dark matter in NGC 3198 (dots with error bars) and the mass of the disk and halo of the galaxy (bold lines) (van Albada et al., 1985).
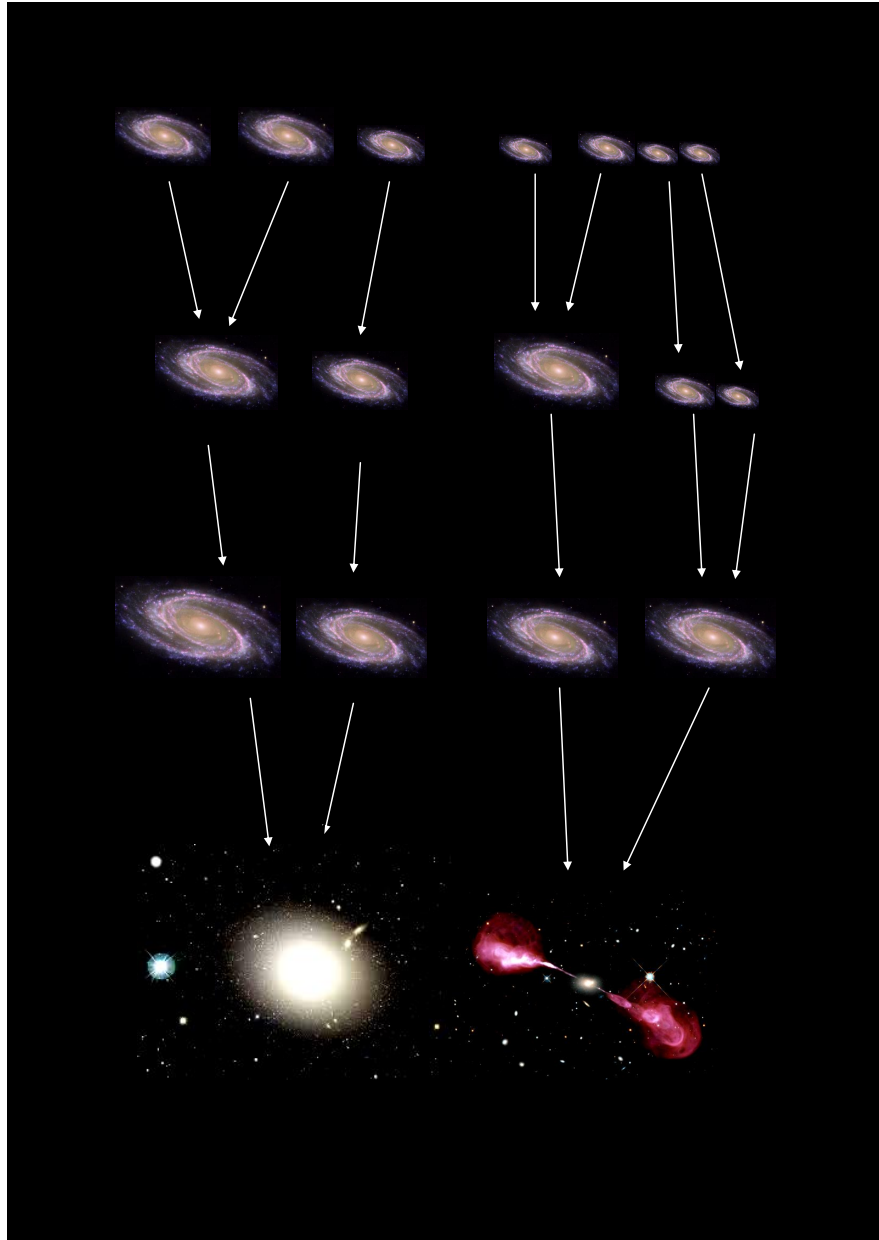
Figure 1.6: Illustration of hierarchical galaxy formation; small spiral galaxies merge to create the large elliptical galaxies seen today. Merging of similar sized spiral galaxies can produce powerful AGN, such as radio galaxies (Baugh et al., 2005; Somerville et al., 2001a).

White & Rees (1978) used models of dark matter haloes to describe the hierarchy of gravitationally bound structures. They proposed that galaxy formation started with dark matter haloes forming in a dissipationless, gravitational collapse. Dissipationless means that the total kinetic and potential energy of a dark matter system is retained. This is because dark matter only interacts through the gravitational forces and therefore it will not lose energy through electromagnetic interactions in the form of radiation. Galaxies then formed inside these dark matter haloes after the baryonic gas cooled and condensed, as first proposed by Hoyle (1953).

Semi-analytic models (SAMs) were then used to describe the formation of dark matter haloes with the inclusion of the baryonic component of matter, permitting the modelling of the observable Universe. SAMs contain physical parameters that are set to match observed properties, such as star-formation, gas cooling and feedback processes (see Section 1.7.6). An advantage of SAMs is that parameters can be turned on or off to gain a better understanding of which parameters have most influence on a particular observation. However, they are limited because they use only one number to represent properties such as mass of stars, cold gas, hot gas and black hole mass for each galaxy, therefore the dynamics within a galaxy are not resolved. The first SAMs of galaxy formation came from White & Frenk (1991). Later on, Kauffmann et al. (1993) and Cole et al. (1994) produced SAMs which could track the formation and evolution of galaxies with evolving dark matter haloes. Recent advancement of SAMs have been able to model the high-redshift and low-mass regimes reliably, and they are in good agreement with a range of observable data such as: galaxy sizes and dynamics, clustering, colours and metal content (Benson & Bower 2010; Guo et al. 2011), and merging histories

of the Universe (Khochfar et al., 2011).

Another method of describing the process of galaxy formation is through hydrodynamical simulations (HYDs). These are different to SAMs because they use models to describe the hydrodynamics and gravitational laws of one galaxy. They allow for the detailed structure of a galaxy to be explored (Neistein et al., 2012). However, these are also limited by resolution. The first HYDs of hierarchical growth of structures were carried out by Davis et al. (1985). Simulations are able to model galaxy formation using the Virgo Consortium's Millennium Simulation (Springel, 2005), this is able to compute the gravitational forces between particles and can identify haloes with masses smaller than the expected mass of the Milky Way's halo. For examples of recent HYDs studies see: Scannapieco et al. (2009); Schaye et al. (2010); Agertz et al. (2011). A possible improvement on these two methods is to combine them both (e.g Stringer et al. 2010; Neistein et al. 2012). However, the predictions of galaxy evolution are dependent on the initial conditions and physical assumptions that each model uses rather than the differences between the two techniques.

1.7.3 Merging scenario

It is thought that the fundamental element of galaxy formation is dark matter haloes and that these follow the hierarchical scenario; however, a key question is how do galaxies form to produce the large elliptical galaxies seen in the present day?

Galaxies are able to build up through galaxy mergers in the hierarchical galaxy formation model (Press & Schechter, 1974; White & Rees, 1978). The most

violent mergers are between two similarly sized dark matter haloes. Hot gas in the individual galaxies would be shock heated during the merger, while any cold gas could fuel star formation and AGN activity in the combined galaxy after the merger (Somerville et al. 2001a; Baugh et al. 2005). If one galaxy is smaller than the other then dynamical friction (Chandrasekhar, 1943) transfers the galaxy's energy from the orbit to the larger galaxy (Johansson et al., 2009). This is done through the gravitational pull by the larger galaxy, which will cause the smaller galaxy to slow down and eventually spiral in towards the center of the larger galaxy. In the current models most elliptical galaxies are formed through mergers, as illustrated in Figure 1.6.

1.7.4 Observational evidence

It is crucial to connect models to actual observable data, such as the galaxy luminosity function. The luminosity function tells us how many galaxies per volume (number density) there are for any given luminosity at a particular epoch, and provides the most fundamental constraint on models (Norberg et al. 2002; Blanton et al. 2003). Before 2006, there was a discrepancy between the models and observations of the galaxy luminosity function. SAMs that matched the observed luminosity function at $z = 0$ often predicted far fewer galaxies at high redshifts than are observed (Baugh et al. 1998; Somerville et al. 2001b; Baugh 2006). Models that could match the abundance of galaxies at high redshifts failed to match the luminosity in the local Universe (Kauffmann et al., 1999a,b). It was not until models by Croton et al. (2006) and Bower et al. (2006), which introduced AGN feedback (see Section 1.7.6), that SAMs could reproduce the

observed luminosity function.

Observations have also suggested that star formation rates in massive galaxies were higher at high redshifts compared to rates in galaxies observed in the local Universe (Cowie et al., 1996; Juneau et al., 2005). This seems to be in contradiction to hierarchical galaxy formation, where lower mass galaxies would be expected to form first and build up through the merging scenario to form more massive galaxies (Jenkins et al. 2001; Sheth et al. 2001; Reed et al. 2007). The fact that massive galaxies have been observed to form before smaller galaxies has been called "cosmic downsizing" (Cowie et al., 1996). AGN feedback has been found to be the likely cause of the discrepancy between observations and the hierarchical picture. AGN can inject energy in the form of radio jets in massive galaxies which would prevent cooling at the centre of massive haloes (Quilis et al. 2001; Brüggen & Kaiser 2002; Churazov et al. 2002; Dalla Vecchia et al. 2004; Sijacki & Springel 2006). The number density of haloes increase towards low redshifts (Mo & White, 2002) but the star formation becomes less efficient and thus the global star formation rate declines with redshift. AGN feedback would be able to explain the decline in star-formation rates.

1.7.5   Formation and Evolution of AGN

To understand the formation of AGN further, the mechanisms behind the transportation of gas needed to feed the SMBH's accretion from inside and outside the host galaxy needs to be considered.

Compared to the mass of the host galaxy, the mass required to fuel the AGN is very low; however, the issue is how the angular momentum of the gas is re-

duced to allow it to accrete onto the SMBH. One possible process is gravitational interactions with other galaxies. Interactions with nearby galaxies can cause the gas in the host galaxy to experience tidal forces which cause the stable disks to develop bars. These bars experience strong gravitational torques which cause the gas to lose angular momentum and accrete on the SMBH (Barnes & Hernquist, 1996). Angular momentum of the gas in the host galaxy may also be lost through galaxy mergers (Springel et al., 2005a). In addition, there might be interactions between the host galaxy and other components in the galaxy to cause the central disk to become barred without any need for galaxy interactions or mergers (Martini et al., 2003).

If bright AGN are powered by high accretion rates we would expect to see the brightest AGN residing in environments that have interacting galaxies, if this is the way in which they are fuelled. There are AGN hosts, at low redshifts, that are found with a possible interacting galaxy (Lacy et al., 2002); however, this does not provide strong evidence on its own that AGN preferentially reside in interacting systems. The model of Hopkins et al. (2006) successfully explains the evolution of galaxies, quasars and starbursts and the growth of SMBHs using the hierarchical models, provided that the merging scenario is responsible for the growth of black holes. These models provide support for the idea that it is mergers which provide the black hole with cold gas, with possible contributions from galaxy encounters and accretion from hot gas haloes.

The typical host galaxies of high-luminosity AGN are early-type galaxies, such as ellipticals and bulges of early-type spirals (Kauffmann et al., 2003). The formation process responsible for producing early-type galaxies, such as galaxy mergers, are similar to the processes responsible for producing AGN, therefore it

is likely that AGN would be found with early-type galaxy hosts. However, not all AGN are found in elliptical galaxies; Seyferts are typically found in spiral galaxies (Kotilainen, 1993). There may be other processes that fuel accretion other than galaxy mergers, such as galaxy bars removing angular momentum that would provide gas, which are found in Seyfert host galaxies (Knapen, 2004).

1.7.6 The Impact of AGN feedback

Two types of AGN feedback, the radiative mode and the mechanical mode, are now normally considered in theoretical models (for a review see Fabian 2012). The radiative mode is thought to be able to heat the gas in the inter stellar medium (ISM) through photoionisation from the radiation which is produced by AGN accretion. This could be produced by bright AGN with efficient accretion rates (Silk & Rees, 1998). The radiative mode operates when the AGN is young, when the galaxy consists of cold gas so that the AGN is obscured. It is possible that radiative pressure can suppress gas cooling and star-formation in halos (Springel et al. 2005b; Hopkins et al. 2006). However, there is less observational evidence for the radiative mode (Fabian, 2012).

The other type of feedback, in this theory, is the mechanical mode which could be from AGN that have low accretion rates and could be caused by radio jets and lobes as discussed in Section 1.5. This mode could be produced by powerful radio jets that inflate bubbles of relativistic plasma on either side of the black hole. This feedback process is possibly seen in nearby elliptical galaxies at the centre of clusters and produces bubbles which are possibly powered by jets (Gull & Northover, 1973). It is more easily observed than the radiative mode because it

is operating in nearby galaxies, which have ionized, hot, transparent gas (Fabian, 2012). Observational evidence for this mode is readily available, the bubbles have been commonly observed with the Chandra telescope (Graham et al. 2008; Fabian et al. 2011).

The mechanical mode could be responsible for quenching cooling flows in clusters of galaxies (Dalla Vecchia et al., 2004; Gaspari et al., 2013). Models also find that mechanical feedback could heat gas in haloes of early-type galaxies and quench star formation in the most massive galaxies (Bower et al., 2006; Croton et al., 2006). These feedback mechanisms could have a crucial effect on the AGN's environment; the radiative mode might be responsible for shaping the galaxy and black hole mass at high redshifts, while the mechanical mode has maintained the galaxy's mass in the low redshift Universe (Churazov et al., 2005).

The most luminous galaxies have been found to live in more massive clusters compared to less luminous galaxies (Norberg et al., 2001; Zehavi et al., 2005). Quasars have also been found to be tracers of the most massive haloes at high redshifts (Falder et al., 2010; Mayo et al., 2012). However, models have recently predicted that feedback is responsible for the fact that the most luminous quasars are not found in the most dense dark matter haloes at $z \sim 0$, which is contrary to what was previously expected (Angulo et al., 2012; Fanidakis et al., 2013). They find that the quasars detected at $z > 5$ are unlikely to be the progenitors of the massive super-clusters observed in the local Universe. This is because their models have found that quasars live in average environments with a typical halo mass of 10^{12} M$_\odot$ which is constant up to $z \sim 4$. If they removed AGN feedback from their models they find that the typical halo mass would be higher than 10^{13} M$_\odot$. Their model also predicts that the super clusters at $z \sim 0$ did not host

a quasar at $z \sim 6$; quasars are generally found in overdense environments, but not the most overdense environments. More observations are needed to confirm these models, by testing whether the most luminous quasars do indeed avoid the most massive dark matter haloes.

1.7.7 The Environmental Dependence of Galaxy Evolution

Many rich galaxy clusters are found in the local Universe, such as the Virgo cluster (Freedman et al., 1994) or the Coma cluster (Briel et al., 1992). These host approximately > 1000 galaxies in just a few Mpc and have been well studied as they are the closest to us. Abell (1958) set out criteria to define and classify clusters of galaxies. The first criterion is the richness of the cluster: a rich Abell cluster must have at least 50 members and a poor Abell cluster has 30 to 50 galaxies. Collections of fewer than 30 galaxies are called groups. The second criterion is the density criterion: the galaxies must be within 1.5 h^{-1}Mpc of the centre of the cluster to be members. The type of galaxies found within the centre of clusters are mainly early-types, which is possible evidence that the cluster environment transforms galaxies, possibly through mergers (Kauffmann & Haehnelt, 2000).

Butcher & Oemler (1984) studied the fraction of blue galaxies in cluster environments at intermediate redshifts ($0.3 < z < 0.5$). They found that there was a larger fraction of blue galaxies in their clusters compared to the galaxies found in clusters in the local Universe. Further evidence for this phenomenon is found from spectroscopic studies of intermediate redshift clusters, which find that there

are more star-forming galaxies in clusters at these redshifts (Dressler & Gunn, 1983). This means that cluster member galaxies were forming stars in the past but have had their star formation quenched in the last $1-2$ Gyrs. This is further evidence that the cluster environment transforms the galaxies from late-types to early-types and from star-forming to passive galaxies in cluster environments.

Several processes which operate in dense environments which may be responsible for these observations. One of the processes is called galaxy harassment, which was first simulated by Farouki & Shapiro (1981). This is where high-speed galaxies (V> 1000 kms^{-1}) interact with each other in clusters; the interaction causes impulsive heating in the galaxy. The stars in the galaxy then become less bound and more likely to be disturbed by other reactions. Galaxy disks could be destroyed by the passage through clusters and nearby interactions with galaxies in the cluster. Models by Moore et al. (1996) show the effect that the interactions have on late-type spiral galaxies in clusters. Galaxy harassment causes the galaxies to lose a lot of mass and transforms the cold disk structure into a more spheroidal structure, similar to what is observed in dwarf and elliptical galaxies in local clusters.

Another process that influences galaxies in clusters is galactic cannibalism (Oemler, 1976). This is where the galaxies in clusters lose energy and momentum due to dynamical friction, which causes them to fall into the centers of clusters. They then merge with the central galaxy. This process causes the central galaxy to increase in mass and reduces the number of dwarf galaxies within the cluster, explaining why observationally we see a large and very bright galaxy, with an extended envelope, in the centre of clusters.

One mechanism that may reduce the amount of cold gas in cluster galaxies

is ram-pressure stripping. This process occurs when a galaxy moves through the intracluster medium (ICM) and its gas component experiences ram pressure which may strip the gas from the galaxy (Gunn & Gott, 1972). This process explains why there are only a limited number of gas-rich star-forming galaxies in clusters at $z = 0$ and may explain why clusters contain a greater number of S0 galaxies compared to the field.

Another mechanism that operates in cluster environments is galaxy strangulation. This process is where the hot halo gas from galaxies that are accreted into the cluster is stripped off by either tidal interactions or ram-pressure stripping (Larson et al., 1980). This gas is not initially used in star formation but it is a reservoir for future star formation as it will eventually cool and fall into the galaxy. If it is stripped then the current star formation will end once the galaxy's cold gas is used up without any replenishment of more cool gas. This results in a decline of the galaxy's star-formation rates within the cluster. This may explain why a galaxy's specific star-formation rate (SSFR), which is the star formation rate (SFR) per unit galaxy stellar mass, is dependent on environmental density (Kauffmann et al., 2004). The star formation in galaxies is found to be much lower in the highest-density environments compared to lower densities.

1.8 AGN and their Environments

1.8.1 AGN used as "Sign-posts" to Galaxy Clusters

To understand how cluster environments affect galaxies at higher redshifts in the Universe, large samples of clusters out to high redshifts ($z > 1$) need to be

obtained. This is difficult because at higher redshifts the galaxies are fainter and more difficult to detect. To find cluster environments out to high redshifts, large area and deep field surveys are required. To avoid searching blindly for galaxy clusters in these large area surveys, which would be time inefficient, AGN have been used as "sign-posts" because they are extremely luminous and can readily be detected out to $z > 6$. This technique has previously been used by many authors to detect some of the densest regions (Best et al. 2003; Wold et al. 2003; Overzier et al. 2006; Overzier et al. 2008; Miley & De Breuck 2008; Hutchings et al. 2009; Falder et al. 2010; Galametz et al. 2010; Falder et al. 2011; Hatch et al. 2011a; Wylezalek et al. 2013).

1.8.2 Environmental Densities

The environments of AGN may be important in addressing the problem of the radio-loud dichotomy, i.e. to investigate whether radio-loud and radio-quiet AGN are intrinsically different objects or whether they are a product of their environment. Do radio-loud AGN reside in similar or different environments to those of radio-quiet AGN? If the environments of the AGN are responsible for this dichotomy, do the radio-loud AGN also influence their environments? Studies of AGN environments have started to provide some evidence to answers to these questions.

As described in Section 1.8.1, AGN have been found in overdense regions compared to background counts in many different studies. This provides evidence that AGN preferentially reside in dense environments.

McLure & Dunlop (2001b) found no difference between the richness of cluster

environment of radio-loud and radio-quiet quasars at $z \sim 0.2$. Similarly, Wold et al. (2001) found no difference between the environments of radio-quiet and radio-loud quasars between $0.5 < z < 0.8$, showing that both classes reside in a wide variety of environments. They conclude that it is mechanisms within the active galactic nucleus which are responsible for producing the powerful radio jets.

However, not all studies have agreed with these findings. There are many which provide evidence that the environments in which radio-loud quasars reside are different to the environments of radio-quiet quasars. Early studies, such as those of Yee & Green (1984, 1987) and Ellingson et al. (1991), found that low to moderate redshift radio-loud quasars were found in denser environments (Abell 0/1) compared to radio-quiet quasars, which were found in clusters only as rich as Abell 0. This fitted into the picture in which radio-loud quasars are found in denser environments compared to radio-quiet quasars.

Recent studies have also found evidence that RLQs occupy different environments to RQQs. Falder et al. (2010) found that a sample of AGN at $z \sim 1$ resided in overdensities and that there was a positive correlation between radio luminosity of the AGN with environmental overdensity. They found that their radio-loud AGN resided in the most overdense environments. Environments can contribute to the radio emission through the process of jet confinement, which enhances synchrotron losses from radio jets, thereby making them brighter (Barthel & Arnaud, 1996).

Galametz et al. (2010) and Mayo et al. (2012) similarly found overdensities of galaxies with active star-formation and evolved populations in the environments of AGN; however, Mayo et al. (2012) found no correlation between the

radio luminosity of their RG sample and the overdensity. Recently, Wylezalek et al. (2013) found that 92 per cent of their radio-loud AGN sample resided in environments richer than average. However, they found no correlation between radio luminosity and environmental density in their sample of RLQs and RGs.

Many of these are at different redshifts, radio luminosities and use different flux-density limits thus making it difficult to get a clear picture of the relationships between AGN and their environments. The AGN sample used by Falder et al. (2010) are matched in luminosity and are chosen to be at the same epoch, which avoids any evolution with redshift. Therefore the difference that they found in the environments of their radio-loud and radio-quiet AGN samples is strong evidence that environment is an important factor in the differences observed between radio-loud and radio-quiet AGN.

1.8.3 Star Formation in AGN Environments

In addition to the environments influencing the radio-loudness of the AGN, the kpc-scale environments of AGN can be probed to see if AGN have influence on the number of star-forming galaxies detected, either through negative or positive feedback (see Section 1.7.6): it is important to distinguish between these feedback effects and a situation in which the star formation is being suppressed in the dense environments where AGN happen to reside (see Section 1.7.7).

As discussed previously, star formation in cluster environments is found to be suppressed at low redshifts $z < 1$ when compared to the field (see Section 1.7.7). However, there are many studies that find AGN with large amounts of star formation in their environments at high redshifts.

Results using sub-millimetre observations show that galaxies with SFRs of order 1000 $M_\odot$ yr^{-1} exist in the environments of AGN at redshifts of $2 < z < 6$ (Ivison et al. 2000; Stevens et al. 2003; Stevens et al. 2004; Priddey et al. 2008; Stevens et al. 2010). In particular, Stevens et al. (2010) detected 17 sub-millimetre galaxies (SMGs) in five fields, centered on quasars at $1.7 < z < 2.8$. The SMGs in their sample have SFRs between $400 - 1300$ $M_\odot$ yr^{-1}. This amount of star formation, if sustained for several hundred million years, would create a stellar mass equivalent to the central bulge of a large galaxy. These SMGs could be progenitors of massive galaxies as seen in the current epoch.

Similarly, Ivison et al. (2000) searched for dusty star-bursts at sub-millimetre wavelengths to find progenitors of massive cluster ellipticals. They focused on the field of the radio galaxy 4C 41.17 at $z = 3.8$, and discovered over-densities of luminous sub-millimetre galaxies when compared to a typical field. These SMGs have bolometric luminosities $> 10^{13} L_\odot$ which correspond to SFRs > 1000 $M_\odot$ yr^{-1}.

Hatch et al. (2011b) conducted a near-IR survey, between $2.2 < z < 2.7$, using an angular auto-correlation function. They detected an over-density of galaxies around 3 RGs, with a significant deviation at the 3σ level from the field. They also found that the rest-frame $U - V$ colour distribution of the protocluster galaxies have a dominant blue sequence, implying that these galaxies are still forming stars.

All of these results imply that powerful AGN, and their environments at $z > 2$, have massive amounts of star-formation activity. When extrapolating to the present day, semi-analytic models of galaxy formation and evolution suggest that they should become the most massive bound objects in the local Universe. However, this may be contradicted by the current dark matter models that predict

that quasars should not reside in the most dense environments and should not be found in the largest present-day clusters (Angulo et al. 2012; Fanidakis et al. 2013). An important point to note is that these studies only use a small number of AGN and therefore it is difficult to extrapolate these results to say that AGN are generally associated with large amounts of star formation at high redshifts.

More star formation would be expected to be detected at higher redshifts since it peaks between $z \sim 1-3$ (Madau et al. 1996; Hopkins 2004; Hopkins & Beacom 2006). It is not clear whether galaxies with active star formation are particularly associated with AGN or whether they are just more common at high redshifts.

1.9 Purpose and Structure of this Work

This Ph.D. will aim to answer the following questions:

- Are AGN found to trace dense environments at high redshifts ($z > 1$)?

- Do radio-loud AGN preferentially reside in dense environments?

- Does star formation evolve differently in high-redshift cluster environments (Stevens et al. 2010; Mayo et al. 2012) compared to the field?

- Do AGN have any impact on star formation in their large scale-environments through feedback processes (Springel et al. 2005b; Hopkins et al. 2006)?

The overall aim of my Ph.D. is to investigate AGN and their environments and calculate the density of star-forming galaxies in the AGN environments throughout cosmic time.

The structure of the thesis is as follows. In Chapter 2, I outline the main telescopes and surveys used in this thesis. In Chapter 3, I introduce the AGN

sample used and I investigate the source density of star-forming galaxies in the environments of a sample of RLQs, RQQs and RGs. I also investigate the galaxy colours in the AGN environments to see if there are any differences between the AGN environments and the field. In Chapter 4, I introduce the VIDEO survey and the neural network method I use to classify quasars in the VIDEO data. I interpret the results using a training sample of known objects to investigate how successful a neural network is at classifying quasars at high redshifts $z \sim 3$. I also compare the neural network method to a colour selection method and I create a list of possible quasar candidates using both methods. In Chapter 5, I investigate the environments of the VIDEO candidate quasars by performing a radial density analysis to search for overdensities. I also find which QSOs have radio counterparts and whether they are radio-loud. This enables me to compare the environments of radio-quiet and radio-loud AGN to investigate whether the environments could be responsible for the dichotomy that is observed. In Chapter 6, I perform another density analysis to investigate the VIDEO QSOs environments and to investigate whether there are any correlations between the environmental density and luminosity, absolute magnitude and redshift for the QSOs. Finally, in Chapter 7 I summarise and conclude.

Throughout this thesis I have assumed a flat cosmology with $H_0 = 72$ km s^{-1} Mpc^{-1}, $\Omega_{\mathrm{m}} = 0.3$ and $\Omega_{\Lambda} = 0.7$. All magnitudes are quoted in the AB system unless stated otherwise.

Chapter 2

Data

My Ph.D. consists of two main science projects which use two main datasets and complementary surveys. In this chapter I discuss the data and telescopes I use and give key information about the surveys. Further information on any of the datasets or surveys can be found from the websites and papers which are referenced in the text.

2.1 Spitzer Telescope

The first data I use are from the Spitzer Space Telescope, which is a space-based infrared observatory that was launched in 25th August 2003. The telescope on Spitzer is a reflector of the Ritchey-Chretien design and it has a mirror that measures 85 cm in diameter. There are three cryogenically-cooled space instruments on board, which provide photometry and spectroscopy in the infrared range. The telescope is sensitive to heat radiation, which means the telescope has to be kept very cold, to as low as 5.5 K. The telescope has three instruments on board; the

Infrared Array Camera (IRAC), the Infrared Spectrograph (IRS) and the Multi-band Imaging Photometer (MIPS). The cryogenic coolant was exhausted in 2009 and only the shortest-wavelength parts of the IRAC are now usable.

I use data from MIPS, which is an imaging camera that detects light at wavelengths of 24, 70 and 160μm, and low-resolution spectroscopy between 55 and 95μm. I use data in the 24μm waveband which is sensitive to dusty regions, such as star-forming galaxies. The detector array for the 24μm waveband is made up of 128×128 pixels and has approximately 5 arcmin^2 field of view. The basic sensitivity of the 24μm waveband is 110μJy at 5σ in 500 seconds on a source with a low background.

The data reduction processing that I perform on the 24μm images are background subtraction and source extraction, all using the SExtractor software package (Bertin & Arnouts, 1996). This is a tool that is used for automatic detection and photometry of sources from FITS images and produces source catalogues for each image.

Further information can be found in Werner et al. (2004) and from the Spitzer website[1].

2.1.1 Spitzer Wide-area InfraRed Extragalactic survey

I use the Spitzer Wide-area InfraRed Extragalactic survey (SWIRE) survey in the project described in Chapter 3. The SWIRE survey is useful because it is a very large wide-area survey ($60 - 65$ sq. degrees) whose purpose is to trace the evolution of dusty star-forming galaxies and evolved stellar populations from $z \sim 3$ to the current epoch. This makes it ideal for achieving the science goals of

---

[1]http://irsa.ipac.caltech.edu/data/SPITZER/docs/spitzermission/
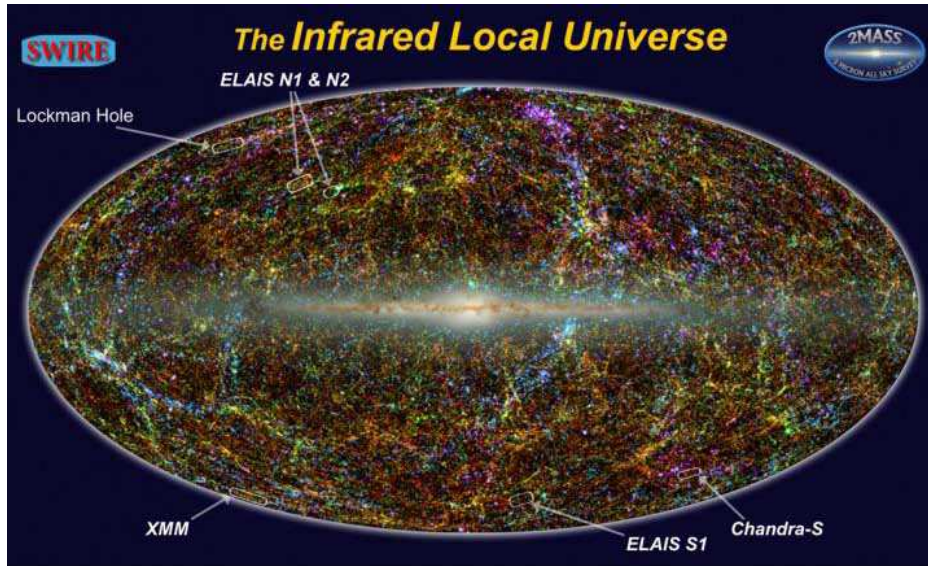
Figure 2.1: An illustration of the fields that are part of the SWIRE survey.

this thesis. The SWIRE survey has IRAC 3.6, 4.5, 5.6, 8μm and MIPS 24, 70, 160μm waveband data in 7 high latitude fields. The fields it covers are ELAIS-S1, XMM-LSS, CDF-S, Lockman, ELAIS-N1 and ELAIS-N2; see Figure 2.1 for an illustration of the main fields. This survey chooses the best fields, where Spitzer can observe at the greatest depth efficiently, by minimising the Galactic cirrus. This is caused by filamentary Galactic dust emission, which is visible over most of the sky and emits in the far-infrared. Fields were also chosen to reduce the background emission from the zodiacal cloud, which produces thermal emission from microscopic dust particles in the Solar System and emits in the mid-infrared.

The SWIRE observations with MIPS produce images with 1.2 arcsecond pixel spacing and the SWIRE team extract their sources using SExtractor, which is the same package I use on my Spitzer images. See Surace et al. (2005) and Lonsdale et al. (2003a) for further details of the observations.
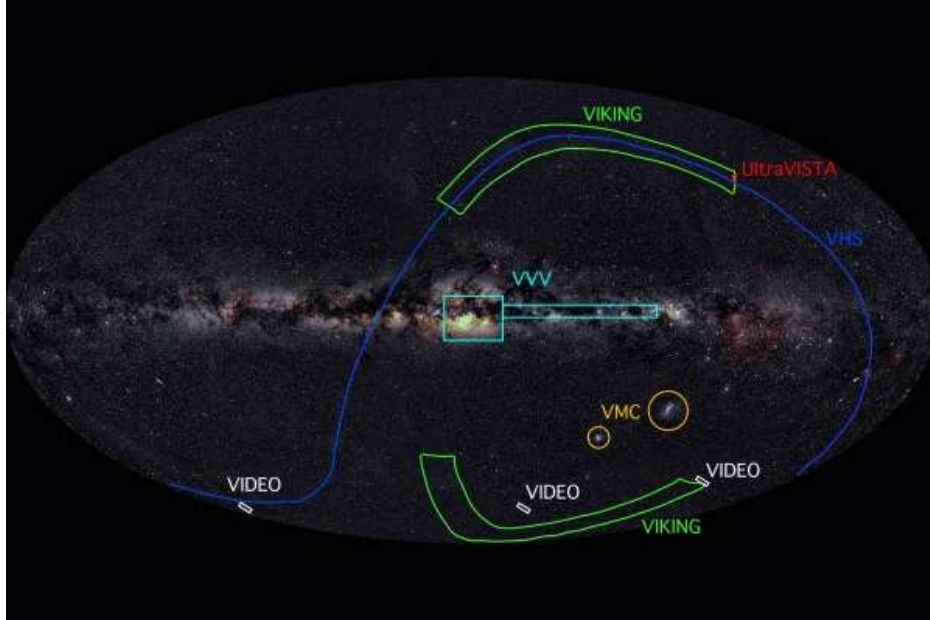
Figure 2.2: The illustration shows the different surveys being conducted with the VISTA near-infrared survey telescope situated at Paranal Observatory in Chile.

2.2 The Visible and Infrared Survey Telescope

The Visible and Infrared Survey Telescope for Astronomy (VISTA) is a 4-m wide field survey telescope and is situated in the Paranal Observatory in Chile. It is being used to carry out multiple surveys of the Southern sky; see Figure 2.2 for the area of sky covered by each survey.

The VISTA telescope uses the VISTA Infrared Camera (VIRCAM; Dalton et al. 2006) which is a wide-field near-infrared camera with a 1.65° diameter field of view and consists of sixteen 2048×2038 arrays with a mean pixel scale of 0.34 arcsec pixel^{-1}. VISTA has filters at Z,Y,J,H and Ks bands and a narrow band filter at 1.18 microns. In my project I use data in the Z,Y,J,H and Ks bands.

2.2.1 VISTA Deep Extragalactic Observations Survey

The VIDEO survey covers a 12 sq. degree area of the sky and has data in the Z, Y, J, H, K_s filters (Jarvis et al., 2013). The VIDEO survey covers the field of Elais-S1 (3 square degrees), XMM-LSS (4.5 square degrees) and the Extended Chandra Deep Field South (CDF-S, 4.5 square degrees). These fields are chosen because they have complementary multi-wavelength data. The Elais-S1, XMM-LSS and the CDF-S fields all have X-ray data, which can link the gas phase to the galaxy population of the clusters. VIDEO reaches depths of $L*$ at $z = 4$ and 0.1 $L*$ at $z = 1$. This coverage enables us to survey representative volumes of the high-redshift Universe, where AGN formation was most abundant, and to detect the bulk of the luminosity density arising from galaxies over 90% of the Universe.

I use data from the VIDEO survey in the form of source catalogues. These are from the XMM3 field and have optical bands coverage from the Canada-France-Hawaii Telescope Legacy Survey Deep-1 field (CFHTLS-D1). Sources in the XMM3 VIDEO field that overlap with the CFHTLS field have been extracted into a catalogue using SExtractor. I also use overlapping radio 1.4 GHz data from the Very Large Array (VLA) (Bondi et al., 2003), see section 2.5. I use the catalogues that have already been produced because all of the data reduction has been performed (Jarvis et al., 2013).

The data reduction on the VIDEO observations was performed by the Cambridge Astronomical Survey Unit (CASU) which used a software pipeline described by Irwin et al. (2004). Details on the specifics of the data reduction are given by Jarvis et al. (2013).

The observations of the XMM3 field were taken between 2009/11/03 and

2011/11/20 over this one field. The observations were carried out in good seeing conditions which ensures the data is of good quality because observations at each filter are required to have a FWHM < 0.8 arcsec.

The individual exposures were split into short segments to overcome the problems with the sky background. The sky is bright and highly variable at these wavelengths, and to reduce the effect of this on the observations short exposures were needed. To overcome the sky variability the telescope is "jittered" around. This means that the telescope is moved around by a random offset of ≤ 20 arcsec in right ascension and declination. For further explanation of the jittering process see Jarvis et al. (2012).

2.2.2 VISTA Kilo-degree Infrared Galaxy survey

As part of my second project, which is outlined in Chapter 4, I use data from the VISTA Kilo-degree Infrared Galaxy survey (VIKING). This survey uses observations from the VISTA telescope and has data in Z,Y,J,H,K_s wavebands. This survey covers 1500 square degrees of the Very Large Telescope Kilo-Degree Survey (VST-KIDs), which adds 4 optical wavebands to the 5 infrared bands at a depth of $K_{s,AB} \sim 21.2$. The main science aim of this survey is to observe $z > 6$ quasars and the bright-end luminosity function.

I use this data to get near-infrared information for QSOs/galaxies from the 2dF-SDSS LRG QSO Survey and Sloan Digital Sky Survey. This is done by cross-matching the QSOs positions within the VIKING database. Further information can be found from the VIKING survey website[1].

---

[1]http://www.astro-wise.org/projects/VIKING/

2.3 VIMOS VLT Deep Survey

I use data from the VIMOS VLT Deep Survey (VVDS, Gavignaud et al. 2006) which is a faint imaging spectroscopic survey which has two types of data. The VVDS-deep targets objects in the range $I_{AB} = 17.5 - 24$, whilst VVSS-wide targets objects in the range $I_{AB} = 17.5 - 22.5$. The VVDS obtains spectroscopic data from the VIsible imaging Multi-Object Spectrograph (VIMOS) and the Near Infra-Red Multi-Object Spectrograph (NIRMOS).

In my project I use a sample of QSOs which are detected in the VVDS-deep data. The VVDS has data in the U, B, V, R, I, J, and K wavebands. The VVDS-deep spectroscopic survey covers two fields ($0226 - 0430$ and $0332 - 2748$) which covers 1×2 degrees and 2×1 degrees of the sky, both go to depths of $I_{AB} = 24.0$. They have complementary radio (1.4 GHz) data from the VVDS-RADIO survey, and imaging in J, H and K from Iovino et al. (2005) and u^*, g', r', i', z' from the Canada-France-Hawaii Legacy Survey (CFHTLS). More details can be found on the VVDS website[1].

2.4 Sloan Digital Sky Survey

I also use data from the well known Sloan Digital Sky Survey (SDSS) which is a large successful survey that has obtained deep, multi-wavelength images covering a large portion of the sky. The SDSS uses a 2.5 m telescope at Apache Point Observatory in New Mexico. The telescope has a 120 mega-pixel camera that images 1.5 square degrees of the sky at any one time.

I use the Seventh Data Release of SDSS (Abazajian et al., 2009). This includes

---

[1]http://cesam.oamp.fr/vvdsproject/

11,663 square degrees of imaging data which lie in regions of low Galactic latitude and has data in 5 wavebands which include u, g, r, i and z. This survey has spectroscopy over 9380 square degrees which consist of $930,000$ galaxies, $120,000$ quasars and $460,000$ stars. There is considerable information about SDSS at their website[1] and more can be found in Abazajian et al. (2009).

2.4.1   2dF-SDSS LRG QSO Survey

I also include QSOs in my project from the 2dF-SDSS LRG QSO Survey (2SLAQ, Croom et al. 2004)[2], which are part of the project outlined in Chapter 4. The QSOs in this sample were selected from SDSS photometry and have spectroscopic information from the 2dF spectrograph on the Anglo-Australian Telescope. This is a deep, extinction corrected survey that goes to depths of $18 < g < 21.85$ and covers 191.9 square degrees of the sky. The main aim of this survey is to probe the optically faint AGN which provide a robust measurement of the QSO luminosity function (Wake et al., 2006).

2.5   VLA 1.4 GHz radio catalogue

In Chapter 5, I use the Very Large Array (VLA) 1.4 GHz radio catalogue (Bondi et al., 2003), which I cross match with the VIDEO data, to obtain radio data for the VIDEO QSOs. The VLA consists of 27 radio antennas that are situated on the Plains of San Agustin in New Mexico; see Figure 2.3 for a picture of the VLA.

---

[1]http://www.sdss.org/
[2]http://www.2slaq.info/

Figure 2.3: A photograph of the VLA radio antennas which are situated on the Plains of San Augustin in New Mexico.

The VLA 1.4 GHz survey has a resolution of 6 arcsec and covers a $1\,\mathrm{deg}^2$ region over the VLA VIRMOS Deep Field (Bondi et al., 2003). The VLA VIRMOS Deep Field covers all of the VIDEO field, which enables me to use this radio survey to find which quasars have radio counterparts. I cross-match the two FITS catalogues in TOPCAT to produce a quasar catalogue that has 1.4 GHz radio data.

Chapter 3

The Environments of 169 AGN at Redshift 1

3.1 Introduction

Powerful radio galaxies could be induced through major gas-rich mergers; evidence for this comes from morphological and spectroscopic studies (Heckman et al., 1986; Ramos Almeida et al., 2011; Tadhunter et al., 2011). Hydrodynamic simulations show that star formation could also be induced in these mergers (Mihos & Hernquist 1996; Di Matteo et al. 2007; Cox et al. 2008; Johansson et al. 2009). Investigating whether radio-loud AGN and star-formation activity is linked would provide information about the nature of the triggering of AGN. Dicken et al. (2012) used the mid-IR waveband and other diagnostic techniques to detect star formation in the host galaxies of radio galaxies. They argued against the idea that there is a close link between star formation and powerful radio-loud AGN activity. They found that only a minority of these AGN are triggered at

the peak of star formation activity in major, gas-rich mergers. However, it is important to note that their sample is at low redshift and may not represent the situation at the peak of star formation.

Mayo et al. (2012) conducted a study of 63 high-redshift ($1 < z < 5.2$) radio galaxies at the 24 μm waveband using the MIPS camera on the *Spitzer Space Telescope*. They found that 20 of their selected fields are overdense, at a 3σ significance, between redshifts $1.173 \leq z \leq 4.413$. 11 of these overdensities have been previously confirmed but 9 of them are new protocluster candidates. They used a flux-density cut of 0.3 mJy and the Rieke et al. (2009) relationship between SFR and 24μm luminosity to find that they are sensitive to SFR = 100 $\mathrm{M}_\odot\mathrm{yr}^{-1}$ at $z = 1$ and ~ 1000 $\mathrm{M}_\odot\mathrm{yr}^{-1}$ at $z = 3$. They found no correlation between the radio luminosity of the RGs and the source density of star-forming objects in their environments.

Radio-quiet AGN host galaxies have been found to host more star formation than those of radio-loud AGN. According to Chen et al. (2012) the fraction of star-forming galaxies is a factor of ~ 2 times lower amongst galaxies with radio-loud AGN than radio-quiet AGN; they found this for both high and low redshifts ($0.4 < z < 0.7$). This possibly implies that AGN with a radio-emitting jet have less star formation, due to the radio lobes expanding and shutting down the cooling onto the host galaxy or possibly due to direct effects on cold gas in the kpc environment of the AGN. It would be interesting to investigate whether the star-formation rates of galaxies within the environments of radio-quiet and radio-loud AGN differ, and so to test whether they inhabit environments with different star-forming properties.

In this project I use observations at 24 μm of 169 radio-loud and radio-quiet

AGN with the *Spitzer Space Telescope* which has the ability to reveal strong dust-obscured star formation in the AGN environments (Saintonge et al., 2008). I use AGN to select possible rich environments at $z \sim 1$ which enables me to probe the epoch when star formation is most prominent, before the star-formation rates decrease, observing galaxies that possibly reside in denser environments. Due to the sample selection at $0.9 < z < 1.1$, I am able to trace the SFR at a single epoch as a function of AGN type. This enables me to investigate whether the AGN environments influence the AGN activity and/or the star-formation activity of galaxies. This programme is thus an extension of the work carried out by Falder et al. (2010), who used the same sample but at 3.6μm, which is sensitive to evolved stellar populations. They found that the 3.6μm overdensities increase with the radio power of the AGN. The aim of this project is to see if star formation is present in the environments of the same AGN sample and whether the source overdensities increase with the radio power of the AGN.

In Section 3.2 I present the sample selection process and in Section 3.3 I describe the observations taken along with the data reduction. In Section 3.4 I discuss the source extraction and explain the methods of analysis. I present my results in Section 3.5. In Section 3.6 I present the galaxy $(24\mu m - 3.6\mu m)$ colours and compare them to the $(24\mu m - 3.6\mu m)$ colours of the field galaxies. The discussion is presented in Section 3.7.

3.2 The Sample Selection

The selection of the sample of AGN was carried out by Falder et al. (2010) and I shall explain the process he used in this section.

The sample of radio-quiet and radio-loud quasars was constructed using the multi-colour selection of the SDSS Quasar Survey. The SDSS quasar catalogue is large, with more than 120,000 quasars which enables a comparison between the colour selected radio-quiet and radio-loud quasars. The initial sample that met the SDSS colour criteria for quasars was then cross referenced with the NRAO VLA Sky Survey (NVSS; Condon et al. (1998), the VLA FIRST survey (Becker et al., 1995) and the Westerbork Northern Sky Survey (WENSS; Rengelink et al. (1997)) to pick out the radio-loud and radio-quiet quasars.

The RLQs were chosen to have a low frequency WENSS (325 MHz) flux density of greater than 18 mJy which is the 5σ limit of the survey. This corresponds to a radio luminosity almost entirely within the radio-loud domain. The sample was compared to the definition of radio-loudness used by Ivezić et al. (2002), seen in Figure 3.1. Here the radio-loud objects are defined to have $R_i > 1$ where $R_i = log_{10}(F_{radio}/F_i)$ and F_{radio} and F_i are flux densities measured at 1.4 GHz and in the i-band respectively (k-corrections are not applied). All except 4 of the sample of RLQs would be considered radio-loud using this definition. The 4 RLQs below the radio-loud line have only one radio flux-density measurement at radio wavelengths and therefore do not have a calculated spectral index. These 4 RLQs were assigned a spectral index of 0.7, which is the mean value of the spectral indices. These objects might fall above the line if they were assigned a higher spectral index; however, using a low frequency radio flux to define the RLQs allows them to be compared more easily to the RGs without severe orientation bias.

The RQQs were defined as being undetected by the FIRST survey at the 5σ level. FIRST was used for this definition because it provides a more sensitive flux

density limit than WENSS. Note that this means that the RQQs are not selected to be true radio-quiet objects as defined by the radio-loudness parameter, since there are only upper limits on their radio flux. The radio images were stacked to reveal the average value of the FIRST radio power (White et al., 2007) for the RQQs in the sample. This includes stacking up the radio images at the known positions of the RQQs, weighting each image by its standard deviation and then computing the average radio emission or obtaining a sensitive upper limit. The stacked radio image is shown in Falder et al. (2010). Using this technique, Falder et al. (2010) found an average flux density for the RQQs at 1.4 GHz of 0.10 ± 0.02mJy (i.e. a 5σ detection). Assuming a spectral index of 0.7 allows for an extrapolation to a 325 MHz flux density of 0.3 ± 0.06mJy which at $z \sim 1$ corresponds to a 325 MHz luminosity, $\log_{10}(L_{325}/WHz^{-1}sr^{-1}) = 23.02$.

The final lists of 75 RLQs and 67 RQQs were chosen so as to be matched in optical luminosity and span the full 5 optical magnitudes available, from -23 to -28 in absolute magnitude of the SDSS i band. The distribution of optical magnitudes within the selected redshift range is shown in Figure 3.2. See Table 3.1 for details of the quasars in the AGN sample, including IDs, positions, i-band absolute magnitudes, AGN types and redshift information.

The RG sample consists of 27 objects. The reason for the substantially smaller RG sample is due to the small numbers of known RG at $z \sim 1$. The radio galaxies have a similar range in radio luminosity to the radio-loud quasars, which were taken from SDSS: see Table 3.2 for the RG sample. They were selected from the 3CRR (Laing et al., 1983), 6CE (Rawlings et al., 2001), 6C* Jarvis et al. (2001), 7CRS (Willott et al., 2003) and TOOT surveys (Vardoulaki et al., 2010). The 6C objects have redshifts taken from Best et al. (1996); Inskip et al. (2005); Rawlings

et al. (2001).

The RGs are either classified as high-excitation galaxies (HEGs), low-excitation galaxies (LEGs) or weak quasars (WQ). Details of the optical classifications of the 3CRR objects are from Jackson & Rawlings (1997), the 6CE objects from Rawlings et al. (2001), the 6C* objects from Jarvis et al. (2001), the 7CE from Willott et al. (2003) and the TOOT objects are described by Vardoulaki et al. (2010).

The radio luminosity distribution of the sample within the selected redshift range is shown in Figure 3.3. This shows that, on average, the RGs are more radio-luminous than the RLQs; however, there is an overlap. Using the FIRST radio images an upper limit can be placed on the radio emission of each RQQ. Figure 3.1 and Figure 3.3 show that at least two thirds of the RQQ sample, and maybe more, would be classified as radio-quiet using the definition from Ivezić et al. (2002). There is an obvious gap between the radio luminosities of the RLQs and the upper limits of the RQQs, seen in Figure 3.3. This effect is due to the difference in the survey depths of the WENSS and FIRST surveys from which they were selected, rather than evidence for any real radio power dichotomy.

The sample is selected to span 5 magnitudes in quasar optical luminosity, as shown in Fig 3.4.
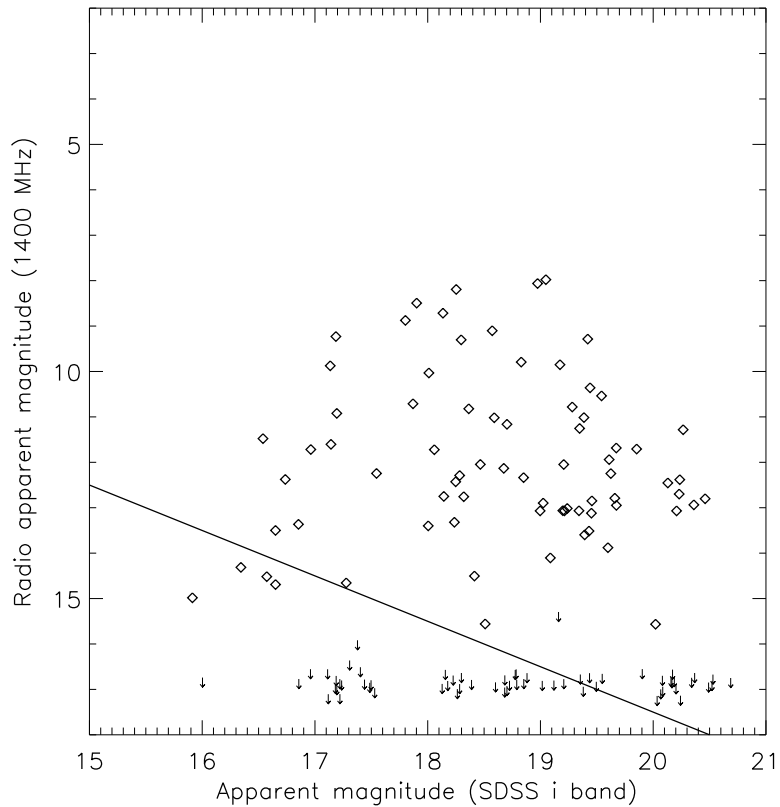
Figure 3.1: Optical apparent magnitude (SDSS i band) vs radio apparent magnitude (NVSS 1400 MHz) for the quasar samples. The radio apparent magnitude is found using $t = -2.5\log(F_{int}/3631Jy)$, where F_{int} is the integrated flux density. This places the radio magnitudes on the AB system of Oke & Gunn (1983). The RLQs are plotted as diamonds while the RQQs are shown as upper limits. The line shows the parameter $R_i = 1$, which is used to determine radio-loudness (Ivezić et al., 2002). The objects falling above the line are classified radio loud while objects falling below the line are classified as radio quiet.
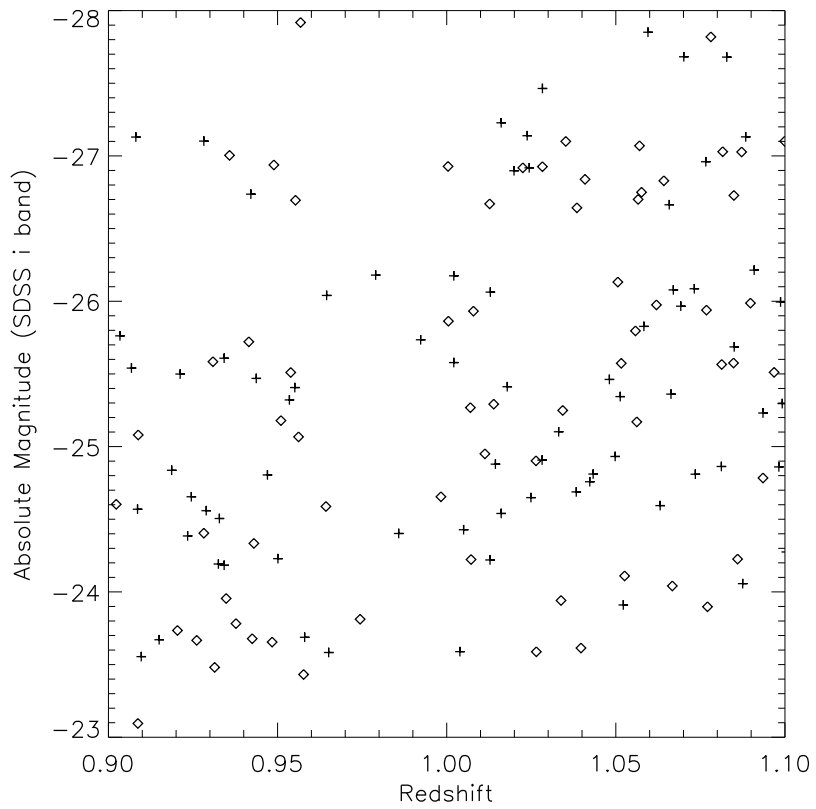
Figure 3.2: Optical absolute magnitude (SDSS i band) vs redshift for the quasars in the sample. The RLQs are plotted as plus signs and the RQQs are plotted as diamonds.
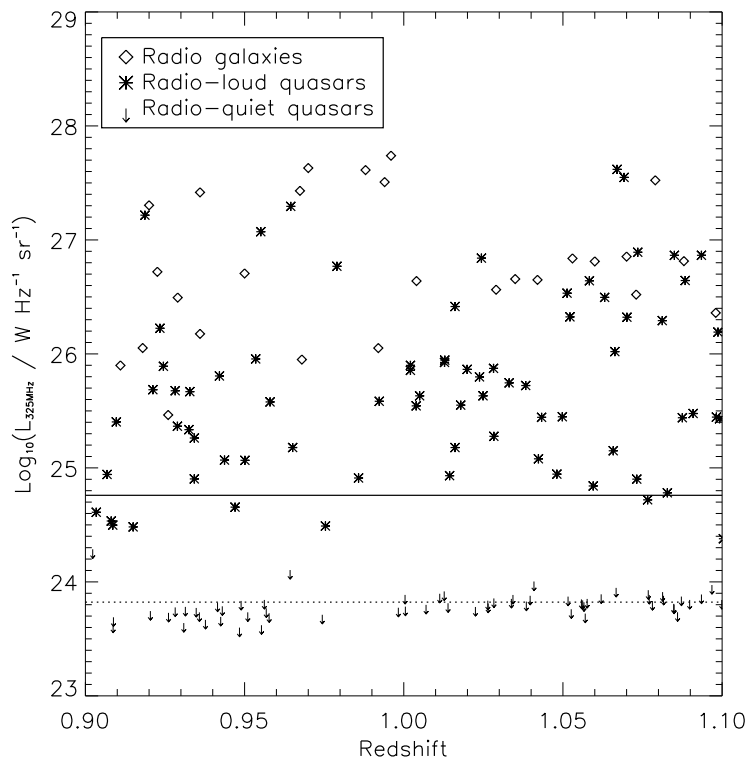
Figure 3.3: The radio luminosity (low frequency, 325 MHz) vs redshift for the sample of AGN. The RGs are represented by diamonds (from WENSS survey), the RLQs are represented by asterisks and the RQQs represented by 5σ upper limits (extrapolated to rest-frame 325 MHz from the FIRST survey). Where WENSS data were unavailable for the RLQs due to sky coverage (approximately 10 objects) the 325 MHz flux density was extrapolated from the NVSS survey at 1400 MHz assuming $\alpha = 0.7$. The line shows the average 5σ limit of the WENSS survey, converted to a luminosity at z = 1 by assuming $\alpha = 0.7$; the RLQs were selected to have radio luminosities falling above this line. The dotted line shows the average 5σ limit of the FIRST survey, extrapolated to 325 MHz and again converted to a luminosity; the RQQs were selected to have a radio luminosity falling below this line. The assumed spectral indices for some conversions explain why some objects fall between the lines on this plot.

57
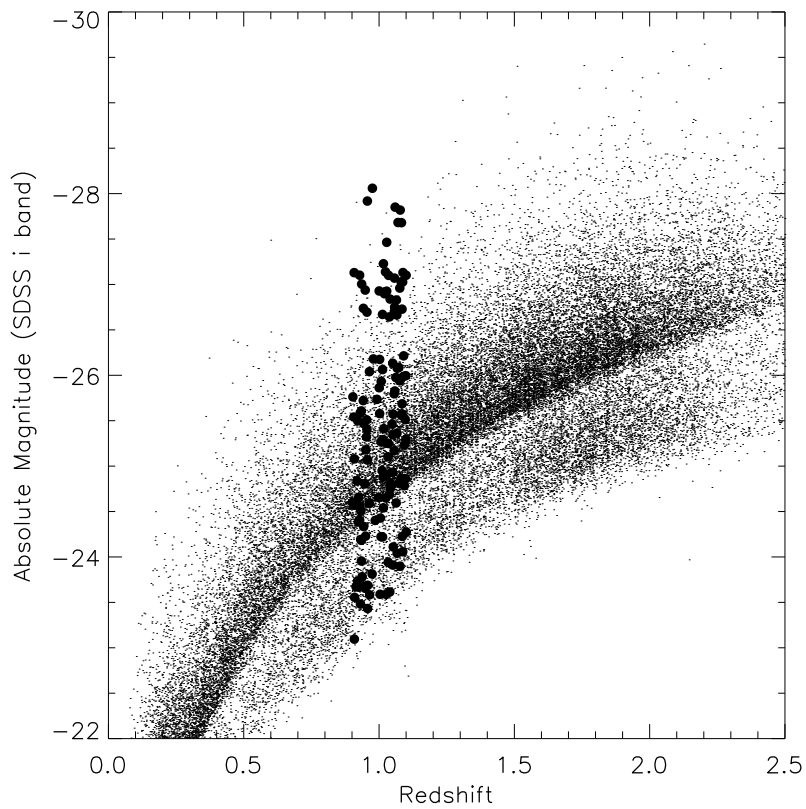
Figure 3.4: Redshift versus optical (SDSS i band) absolute magnitude. The smaller dots represent the quasars from the fifth data release of the SDSS quasar survey (Schneider et al., 2005). The dots in bold represent the quasars used in our sample in the redshift range of $0.9 < z < 1.1$, showing that they span a range of 5 magnitudes in optical luminosity.

Table 3.1: The complete quasar sample, including the RLQs and RQQs. I include the ID, RA and Dec of the AGN positions, the i-band absolute magnitude, the AGN type (RQQs=2 and RLQs=3) and the redshifts of the AGN sample.

ID	RA	Dec	AbsMagi	Type	Redshift
SDSS003146.07+134629.6	7.94196	13.7750	-24.2230	2	1.007
SDSS023540.90+001038.9	38.9204	0.177550	-23.6550	2	0.948
SDSS073802.37+383116.3	114.510	38.5213	-26.9180	2	1.023
SDSS074417.47+375317.2	116.073	37.8881	-26.0780	3	1.067
SDSS074729.24+434607.5	116.872	43.7688	-24.2260	2	1.086
SDSS074815.44+220059.5	117.064	22.0166	-27.8510	3	1.059
SDSS075058.21+421617.0	117.743	42.2714	-23.7820	2	0.938
SDSS075222.91+273823.2	118.095	27.6397	-27.0700	2	1.057
SDSS075339.84+250137.9	118.416	25.0272	-24.3340	2	0.943
SDSS075928.29+301028.3	119.868	30.1746	-26.1750	3	1.002
SDSS080915.88+321041.6	122.316	32.1782	-23.6710	3	0.915
SDSS081520.66+273617.0	123.836	27.6047	-27.1300	3	0.908
SDSS082012.62+431358.5	125.053	43.2329	-26.0860	3	1.073
SDSS082229.78+442705.2	125.624	44.4515	-26.7010	2	1.057
SDSS082836.39+504826.5	127.152	50.8074	-24.5590	3	0.929

Continued on Next Page. . .

Table 3.1 – Continued

ID	RA	Dec	AbsMagi	Type	Redshift
SDSS082901.27+371806.1	127.255	37.3017	-24.1830	3	0.934
SDSS083110.01+374209.6	127.792	37.7026	-24.8370	3	0.919
SDSS083115.89+423316.6	127.816	42.5546	-25.5840	2	0.931
SDSS083226.07+343414.3	128.109	34.5708	-24.4280	3	1.005
SDSS083248.44+422459.5	128.202	42.4165	-25.3440	3	1.051
SDSS083315.07+350647.3	128.313	35.1131	-24.8600	3	1.098
SDSS083407.56+354712.0	128.531	35.7867	-24.0570	3	1.088
SDSS084028.34+323229.4	130.118	32.5415	-25.2960	3	1.099
SDSS084723.67+011010.4	131.849	1.16952	-25.5650	2	1.081
SDSS090037.89+550318.0	135.158	55.0550	-24.8050	3	0.947
SDSS090142.41+425631.0	135.427	42.9419	-24.8790	3	1.014
SDSS090153.42+065915.6	135.473	6.98759	-27.0290	2	1.082
SDSS090812.18+514700.8	137.051	51.7836	-25.5780	3	1.002
SDSS090910.09+012135.7	137.292	1.35987	-26.9180	3	1.024
SDSS091011.01+463617.8	137.546	46.6049	-26.8980	3	1.019
SDSS091216.88+420314.2	138.070	42.0540	-23.8980	2	1.077
SDSS091921.56+504855.4	139.840	50.8154	-25.4990	3	0.921
SDSS092257.86+444651.8	140.741	44.7811	-25.9390	2	1.077
SDSS092753.52+053637.0	141.973	5.61023	-25.9750	2	1.062
SDSS092829.86+504836.6	142.124	50.8101	-25.2490	2	1.034

Continued on Next Page...

Table 3.1 – Continued

ID	RA	Dec	AbsMagi	Type	Redshift
SDSS093023.28+403111.0	142.597	40.5197	-25.5110	2	1.097
SDSS093303.50+460440.2	143.265	46.0777	-25.9870	2	1.089
SDSS093332.71+414945.0	143.386	41.8292	-24.1920	3	0.933
SDSS093759.44+542427.3	144.497	54.4076	-24.0410	2	1.067
SDSS094644.72+414304.5	146.686	41.7179	-25.4120	3	1.018
SDSS094740.01+515456.8	146.916	51.9158	-24.5940	3	1.063
SDSS094811.89+551726.5	147.049	55.2907	-23.9410	2	1.034
SDSS095227.30+504850.7	148.114	50.8140	-26.2140	3	1.091
SDSS100730.47+050942.3	151.877	5.16167	-23.7350	2	0.920
SDSS100835.81+513927.8	152.149	51.6577	-25.5750	2	1.085
SDSS100906.35+023555.3	152.276	2.59872	-27.1010	2	1.100
SDSS100940.46+465525.0	152.419	46.9236	-24.2200	3	1.013
SDSS100943.56+052953.9	152.431	5.49834	-26.7370	3	0.942
SDSS102005.99+033308.5	155.025	3.55233	-27.0040	2	0.936
SDSS102111.57+611415.0	155.298	61.2375	-23.4810	2	0.931
SDSS102349.40+522151.2	155.956	52.3642	-26.6950	2	0.955
SDSS103347.32+094039.0	158.447	9.67751	-26.9260	2	1.028
SDSS104537.69+484914.6	161.407	48.8207	-23.6780	2	0.9425
SDSS104542.18+525112.6	161.426	52.8534	-25.8270	3	1.058
SDSS104935.76+554950.6	162.399	55.8307	-25.7960	2	1.056

Continued on Next Page. . .

Table 3.1 – Continued

ID	RA	Dec	AbsMagi	Type	Redshift
SDSS105408.88+042650.4	163.537	4.44733	-26.7280	2	1.085
SDSS112023.23+540427.1	170.097	54.0742	-24.3850	3	0.923
SDSS112317.52+051804.0	170.823	5.30109	-26.9280	2	1.000
SDSS114700.39+620008.1	176.752	62.0023	-26.8390	2	1.041
SDSS115027.25+665848.0	177.613	66.9800	-27.1000	2	1.035
SDSS115120.46+543733.1	177.835	54.6259	-28.0590	3	0.975
SDSS120127.43+090040.6	180.364	9.01130	-27.2280	3	1.016
SDSS120556.09+104253.9	181.484	10.7150	-27.1310	3	1.088
SDSS121529.56+533555.9	183.873	53.5989	-25.9660	3	1.069
SDSS122339.34+461118.7	185.914	46.1886	-26.0630	3	1.013
SDSS122409.91+500155.5	186.041	50.0321	-26.6640	3	1.066
SDSS122832.94+603735.1	187.137	60.6264	-23.6140	2	1.040
SDSS123059.71+101624.8	187.749	10.2735	-25.1700	2	1.056
SDSS123259.81+513404.5	188.249	51.5679	-24.4020	3	0.986
SDSS125139.05+542758.1	192.913	54.4662	-25.3610	3	1.066
SDSS131103.20+551354.4	197.763	55.2317	-24.6550	3	0.925
SDSS132909.25+480109.7	202.289	48.0194	-27.1020	3	0.928
SDSS132957.15+540505.9	202.488	54.0850	-26.9380	2	0.949
SDSS133713.06+610749.0	204.304	61.1303	-23.6670	2	0.926
SDSS133733.30+590622.6	204.389	59.1063	-27.0270	2	1.087

Continued on Next Page. . .

Table 3.1 – Continued

ID	RA	Dec	AbsMagi	Type	Redshift
SDSS133749.64+550102.2	204.457	55.0174	-25.9950	3	1.099
SDSS134213.27+602142.8	205.555	60.3619	-26.0400	3	0.965
SDSS134357.62+575442.5	205.990	57.9118	-24.5050	3	0.933
SDSS134635.02+415630.9	206.646	41.9420	-24.6030	2	0.902
SDSS134934.65+534117.0	207.394	53.6881	-26.1800	3	0.979
SDSS135823.99+021343.8	209.600	2.22889	-27.9180	2	0.957
SDSS141028.21+460821.0	212.617	46.1391	-24.5400	3	1.016
SDSS141802.79+414935.3	214.512	41.8265	-24.7580	3	1.042
SDSS142124.65+423003.2	215.353	42.5009	-25.8630	2	1.001
SDSS142817.30+502712.6	217.072	50.4535	-26.6700	2	1.013
SDSS142829.93+443949.8	217.125	44.6638	-24.9320	3	1.050
SDSS143253.73+460343.8	218.224	46.0622	-26.9600	3	1.077
SDSS143746.64+443258.6	219.444	44.5496	-25.4690	3	0.944
SDSS143844.80+621154.5	219.686	62.1985	-25.2310	3	1.094
SDSS144527.40+392117.0	221.364	39.3547	-23.5830	3	0.965
SDSS144837.54+501448.9	222.156	50.2469	-24.8100	3	1.074
SDSS145503.47+014209.0	223.764	1.70255	-24.1100	2	1.053
SDSS145506.12+562935.6	223.775	56.4932	-26.6430	2	1.039
SDSS150031.81+483646.8	225.132	48.6131	-27.4640	3	1.028
SDSS150133.92+613733.8	225.391	61.6260	-23.5550	3	0.910

Continued on Next Page. . .

Table 3.1 – Continued

ID	RA	Dec	AbsMagi	Type	Redshift
SDSS150759.06+020053.8	226.996	2.01498	-27.6800	3	1.083
SDSS151520.56+004739.3	228.836	0.794290	-25.1790	2	0.951
SDSS151921.85+535842.3	229.841	53.9784	-23.5880	2	1.027
SDSS152556.23+591659.5	231.484	59.2832	-25.4060	3	0.955
SDSS152949.77+394509.6	232.457	39.7527	-24.8630	3	1.081
SDSS154515.89+432953.1	236.316	43.4981	-25.7620	3	0.903
SDSS155404.96+461107.5	238.521	46.1855	-23.5890	3	1.004
SDSS155416.50+513218.9	238.569	51.5386	-25.5400	3	0.907
SDSS155436.25+320408.4	238.651	32.0690	-26.7500	2	1.058
SDSS155650.41+394542.8	239.210	39.7619	-25.7210	2	0.942
SDSS155729.94+330446.9	239.375	33.0797	-25.3210	3	0.954
SDSS160516.07+313620.8	241.317	31.6058	-24.9070	3	1.028
SDSS161603.76+463225.3	244.016	46.5404	-24.2290	3	0.950
SDSS161806.32+422532.1	244.526	42.4256	-25.6080	3	0.934
SDSS162553.31+434713.8	246.472	43.7872	-25.4620	3	1.048
SDSS162917.79+443452.4	247.324	44.5812	-25.1020	3	1.033
SDSS163302.10+392427.4	248.259	39.4076	-27.1390	3	1.024
SDSS163402.95+390000.6	248.513	39.0002	-25.6860	3	1.085
SDSS163408.64+331242.1	248.536	33.2117	-25.2680	2	1.007
SDSS163624.98+361458.0	249.104	36.2494	-24.5690	3	0.909

Continued on Next Page. . .

Table 3.1 – Continued

ID	RA	Dec	AbsMagi	Type	Redshift
SDSS164054.17+314329.9	250.226	31.7250	-23.6880	3	0.958
SDSS164617.17+364509.4	251.572	36.7527	-23.4320	2	0.958
SDSS165231.30+353615.9	253.130	35.6044	-24.4040	2	0.928
SDSS165919.97+374332.7	254.833	37.7258	-24.6490	3	1.025
SDSS165943.08+375422.7	254.930	37.9063	-24.6880	3	1.038
SDSS170648.07+321422.9	256.700	32.2397	-27.6820	3	1.070
SDSS170949.24+303259.2	257.455	30.5498	-24.8110	3	1.043
SDSS171005.53+644843.0	257.523	64.8119	-25.9320	2	1.008
SDSS171330.21+644253.0	258.376	64.7147	-26.1320	2	1.051
SDSS171704.69+281400.6	259.270	28.2335	-27.8190	2	1.078
SDSS172955.84+530955.9	262.483	53.1656	-23.9100	3	1.052
SDSS215541.74+122818.8	328.924	12.4719	-26.8290	2	1.064
SDSS224159.43+142055.2	340.498	14.3486	-25.5100	2	0.954
RSDSS103525.05+580335.6	158.854	58.0599	-24.5880	2	0.964
RSDSS104659.37+573055.6	161.747	57.5155	-24.9020	2	1.026
RSDSS103829.74+585204.1	159.624	58.8678	-23.9550	2	0.935
RSDSS104859.67+565648.6	162.249	56.9468	-25.2920	2	1.014
RSDSS103855.33+575814.7	159.731	57.9708	-25.0670	2	0.956
RSDSS104930.46+592032.6	162.377	59.3424	-24.9500	2	1.011
RSDSS104114.18+590219.4	160.309	59.0387	-24.7840	2	1.094

Continued on Next Page. . .

Table 3.1 – Continued

ID	RA	Dec	AbsMagi	Type	Redshift
RSDSS160913.18+535429.6	242.305	53.9082	-25.7350	3	0.992
RSDSS104156.51+593611.2	160.486	59.6031	-24.2750	3	1.100
RSDSS163225.56+411852.0	248.107	41.3146	-25.0800	2	0.909
RSDSS104239.66+583231.0	160.665	58.5420	-24.6550	2	0.998
RSDSS163306.12+401747.0	248.276	40.2965	-23.8120	2	0.974
RSDSS104355.47+593054.0	160.981	59.5150	-23.0950	2	0.909
RSDSS163930.82+410013.2	249.878	41.0038	-25.5730	2	1.051

3.3 Observations and the Data Reduction

The observations were taken with the MIPS camera on the *Spitzer Space Telescope* which provides 24μm capability, as discussed in Chaper 2.

The observations were carried out between August 2006 and August 2007. The sample of quasars was expected to have a 24μm flux density of approximately 500μJy, so one cycle of 7 jitters was used with a 10s exposure per jitter which results in a total exposure of 70s. For the radio galaxies, the 3CRR sources were observed with the same strategy while the less radio-luminous objects from the 6CE, 7CRS and TOOT samples were observed for 2 cycles of 7 jitters. This resulted in a total exposure time of 140s. Thirteen of the quasar sample were taken from the Spitzer Wide-area InfraRed Extragalactic (SWIRE; Lonsdale et al.,

Table 3.2: Table of the radio galaxies used in the AGN sample. I display the RG's ID, its observed-frame 325 MHz flux density (S_{325} (Jy)), the spectral index (α) and the redshift information (z) which are taken from NED except for the 6C* and TOOT objects, see Falder et al. (2010) for further details. The optical classification of the RGs according to the literature: HEG = high-excitation galaxy, LEG = low - excitation galaxy and WQ = weak quasar (Rawlings et al., 1995).

Name	S_{325} (Jy)	α	z	Class
3C 175.1	6.939	0.85	0.920	HEG
3C 184	9.097	0.87	0.994	HEG
3C 22	8.348	0.90	0.936	WQ
3C 268.1	15.615	0.58	0.970	HEG
3C 280	16.025	0.81	0.996	HEG
3C 289	8.278	0.84	0.967	HEG
3C 343	13.413	0.68	0.988	HEG
3C 356	6.820	1.04	1.079	HEG
6C E0943+3958	1.182	0.85	1.035	LEG?
6C E1011+3632	1.190	0.79	1.042	HEG
6C E1017+3712	1.540	1.00	1.053	HEG
6C E1019+3924	1.690	0.94	0.923	LEG?
6C E1129+3710	1.543	0.89	1.060	HEG
6C E1212+3805	1.408	1.06	0.950	LEG?
6C E1217+3645	1.402	0.94	1.088	HEG?
6C E1256+3648	1.760	0.81	1.070	HEG?
6C E1257+3633	1.036	1.08	1.004	HEG
6C*0128+394	1.322	0.50	0.929	HEG?
6C*0133+486	0.742	1.22	1.029	LEG?
5C 6.24	0.839	0.77	1.073	HEG
5C 7.17	0.469	0.93	0.936	HEG
5C 7.23	0.546	0.78	1.098	HEG
5C 7.242	0.304	0.94	0.992	HEG?
5C 7.82	0.371	0.93	0.918	LEG?
TOOT1066	0.098	0.87	0.926	LEG?
TOOT1140	0.298	0.75	0.911	LEG
TOOT1267	0.282	0.80	0.968	HEG

2003a) survey. The data reduction was performed using the standard pipeline version S15.0.5.

3.4 Density Analysis

3.4.1 Method

To investigate the environments of the AGN I have used a radial analysis technique. This technique is used to search for sources within a given area in the nearby environments of AGN. This was done by placing concentric annuli over each image fixed on a certain position. The area of each annulus was fixed, this ensured that the Poisson errors for each bin were similar so that a comparison between source densities between each annulus was possible.

For an illustration of this method see Figure 3.5. I have used an image of 3C22 radio galaxy for an example of this method and have overlaid the annuli used. They are centered on the coordinate of the radio galaxy. There was a change of depth beyond the central region of the images and therefore I was limited to a radius of 89 arc seconds from the central AGN.

3.4.2 Source extraction

The SExtractor software package (Bertin & Arnouts, 1996) was utilized to find the sources in the AGN fields. I used a detection threshold of 5 adjacent pixels each at 1.5σ above the local background level. The seeing full-width half maximum (FWHM) was set to 6.0 arc seconds, the pixel spacing to 2.45 arc seconds per pixel and the aperture diameter to 4.9 pixels. The background mesh size parameter was set to 32 pixels, which estimates the background of the image and the RMS noise in that background. The background filter was set to 6 times the background mesh size; this smooths the image to help detect faint, extended objects. I found
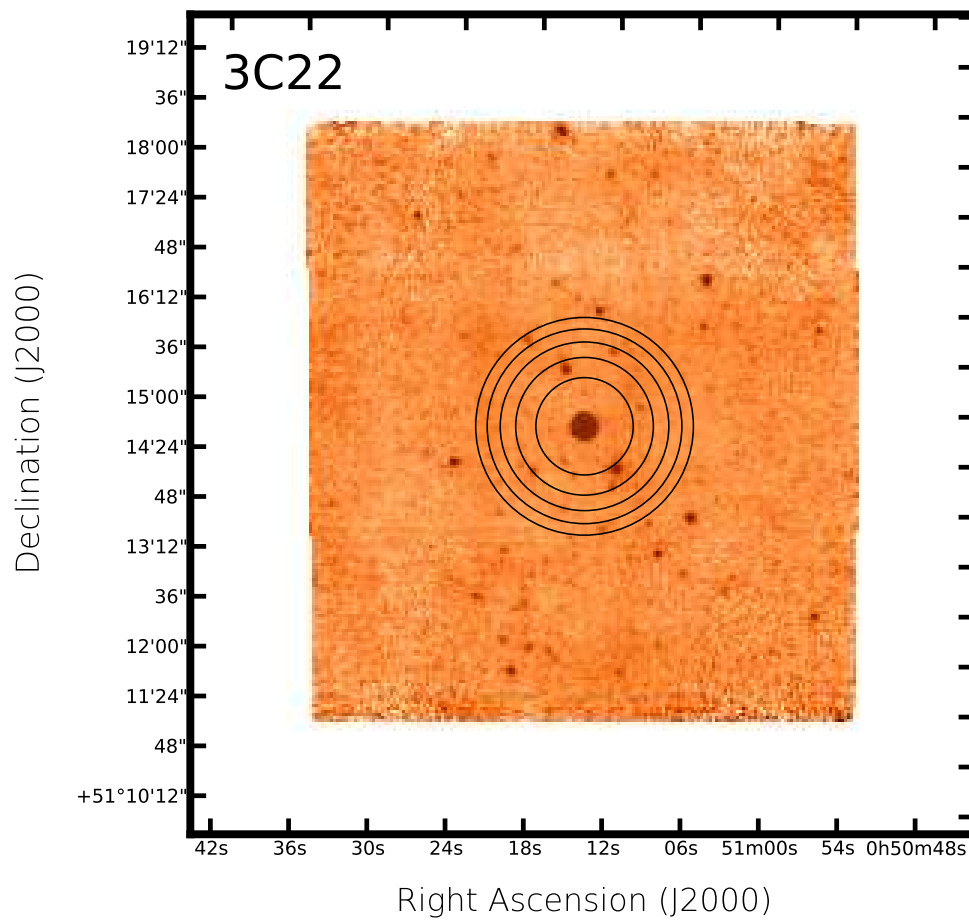
Figure 3.5: Image of 3C22 radio galaxy in the sample together with the 5 annuli used.

that this was the optimum value for these data after I observed background maps using different values, as discussed further in the following sub-section. All other parameters were left at their default settings. To check for any missing sources or spurious detections, the AGN fields were visually inspected.

3.4.3   Background subtraction

The confusion noise in the images was subtracted by creating background maps, for every image, using the LOCAL BACKGROUND parameter in SExtractor. The size of the background mesh size parameter was checked by using background mesh sizes of 8, 12, 32 and 64 pixels; see Figures 3.6, 3.7, 3.8 and 3.9 for example background maps for 3C175.1. If the background mesh size is too small the estimate will be partly object flux, as shown in Figure 3.6 and Figure 3.7. If the background mesh is too large the small scale variations in the background will not be taken into account and the background will be very smooth, as shown in Figure 3.9. I chose 32 pixels (see Fig 3.8) as a background mesh size, which took into account variations in the background without including any flux from objects in the field.

A further check of this background size was done by placing the source extracted objects in the field on top of the image and checking that they were in sensible places. I did this for each background size and found that the most reliable one was the 32 pixel mesh size.

Figure 3.6: Background map of 3C175.1 using a background mesh size of 8 pixels.

Figure 3.7: Background map of 3C175.1 using a background mesh size of 12 pixels.
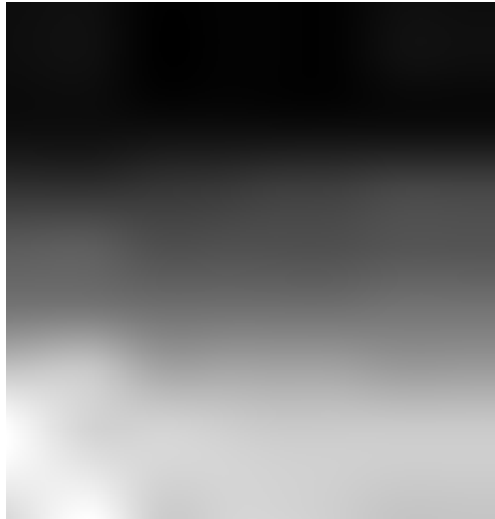
Figure 3.8: Background map of 3C175.1 using a background mesh size of 32 pixels.
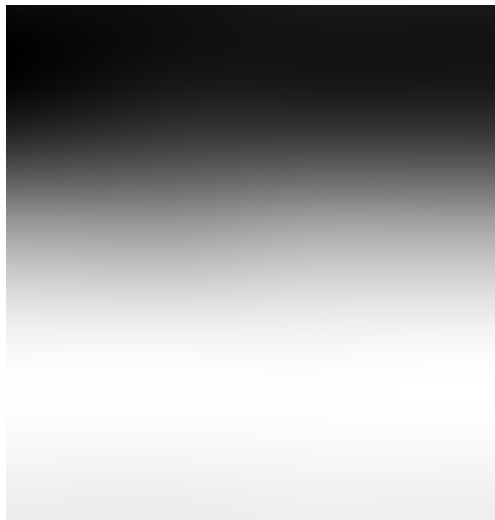
Figure 3.9: Background map of 3C175.1 using a background mesh size of 64 pixels.
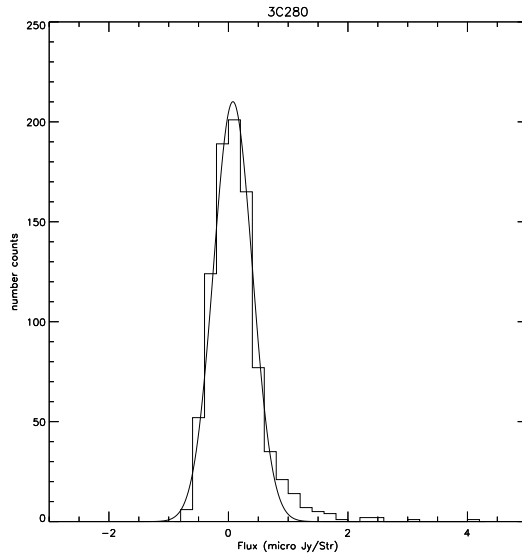
Figure 3.10: Histogram of the background noise (μJy) from the field containing the radio galaxy 3C280 together with the fitted Gaussian curve to calculate the 3σ noise values.

3.4.4   Source Cuts

To ensure that all of the images are analysed to a common depth a comparison of the source counts for each field is needed, but it is important to do this in a statistically rigorous manner. This point is especially relevant since data for a number of the AGN fields are taken from the SWIRE survey which has a much lower noise level than my data.

To determine a suitable flux-density cut to the data, which ensures a uniform sensitivity throughout, I calculated the RMS noise for fluxes in apertures of 2.45 arcsec radius. This was done by placing a thousand apertures randomly on each
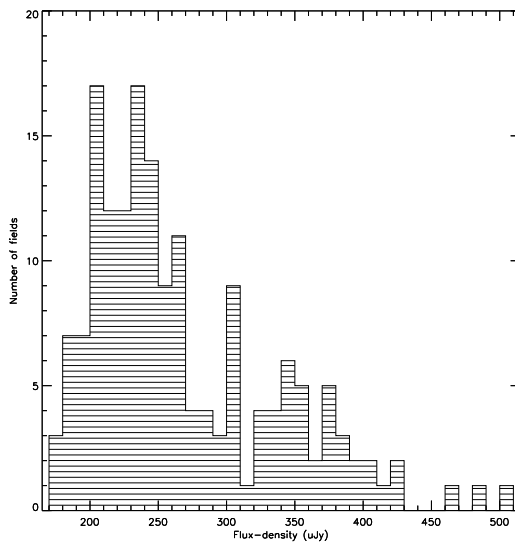
Figure 3.11: Histogram of the 3σ noise values for all 169 fields.

field. I ensured that the apertures did not overlap with any real sources by placing them 12 arcsec (4.9 pixels) away from any given source. This guaranteed that the background noise was not skewed by the flux from the sources. The aperture fluxes were then binned and I performed a Gaussian fit to find the 3σ noise values for each field; for an example see Figure 3.10. For the flux-density cut I analysed the 3σ noise values for all of the fields and found that they varied significantly; I found a range of 171 μJy to 505 μJy and a mean of $f_{24\mu m} = 268\mu$Jy. For a plot of the 3σ noise values for the whole AGN sample see Figure 3.11. I adopted a conservative limit of $f_{24\mu m} = 450\mu$Jy which ensured I was above the 3σ limit for the majority of the AGN fields. Only 3 fields are slightly above my flux-density cut; this should not affect the results.

Table 3.3: Table of the number of annuli with their outer radii from the central AGN in arcsec and Mpc.

Annulus	Outer radius (arcsecs)	Outer radius (Mpc)
1	40.0	0.3
2	56.6	0.4
3	69.3	0.5
4	80.0	0.6
5	89.4	0.7

I checked how complete the fields are at their 5σ flux-density limits and found that most of the fields have a completeness ≥ 50 per cent, within the 300kpc-700kpc region; see Figure 3.12. I find that the inner 300kpc region is less complete but this is to be expected for the first annulus, due to the central AGN; see Figure 3.13.

3.4.5 Source Counts

I compared the environments of the AGN by counting the number of sources detected in various annuli around the AGN. In the radial search I was limited to a maximum search radius of 89 arcsec from the AGN, equivalent to ~ 0.7Mpc at $z = 1$. This was due to the reduced integration time at the edge of the images compared to the centre of the images, which was caused by the dither of the telescope. The 5 annuli I used can be found in Table 3.3: I chose the radii to ensure that all have an area of 1.396 arcmin^2. I counted the number of sources detected in the whole ~ 0.7Mpc radius in the AGN environments, which has a total area of 6.91 arcmin^2. The target AGN was excluded from the source counts, in each AGN field, as this would otherwise create a bias in the first bin compared to the outer bins.
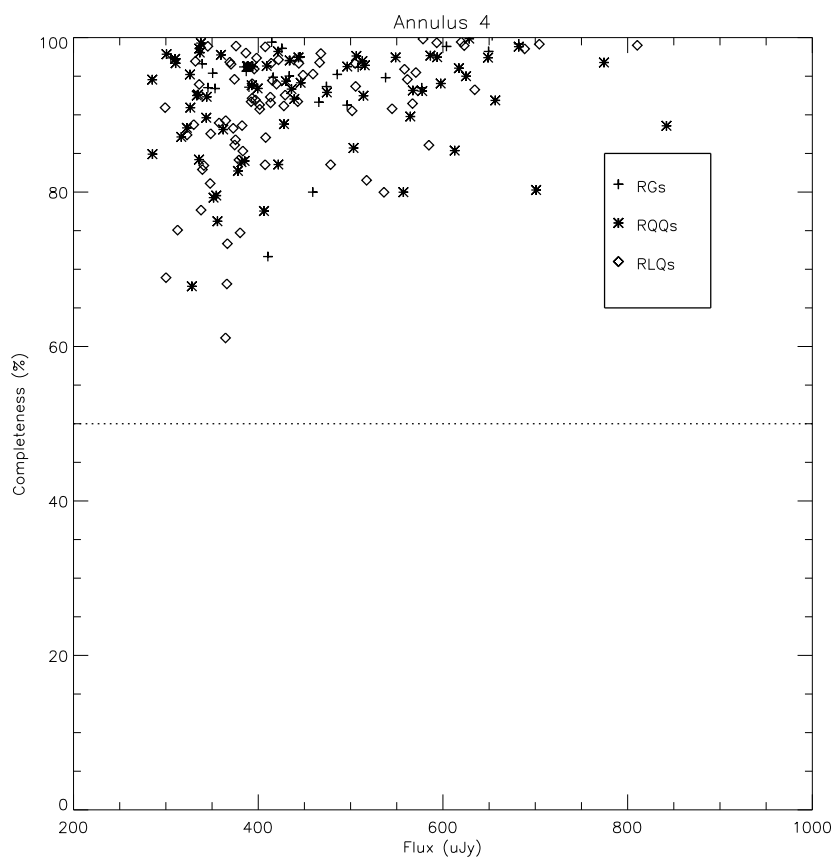
Figure 3.12: The completeness values in annulus 4 versus the 5σ noise for each field. The crosses represent the RGs, the asterisks represent the RQQs and the diamonds represent the RLQs. The dotted line represents the 50 per cent completeness.

It is not very useful to compare one individual field to another because the

Poisson error for individual fields is too high and thus the catalogues were com-
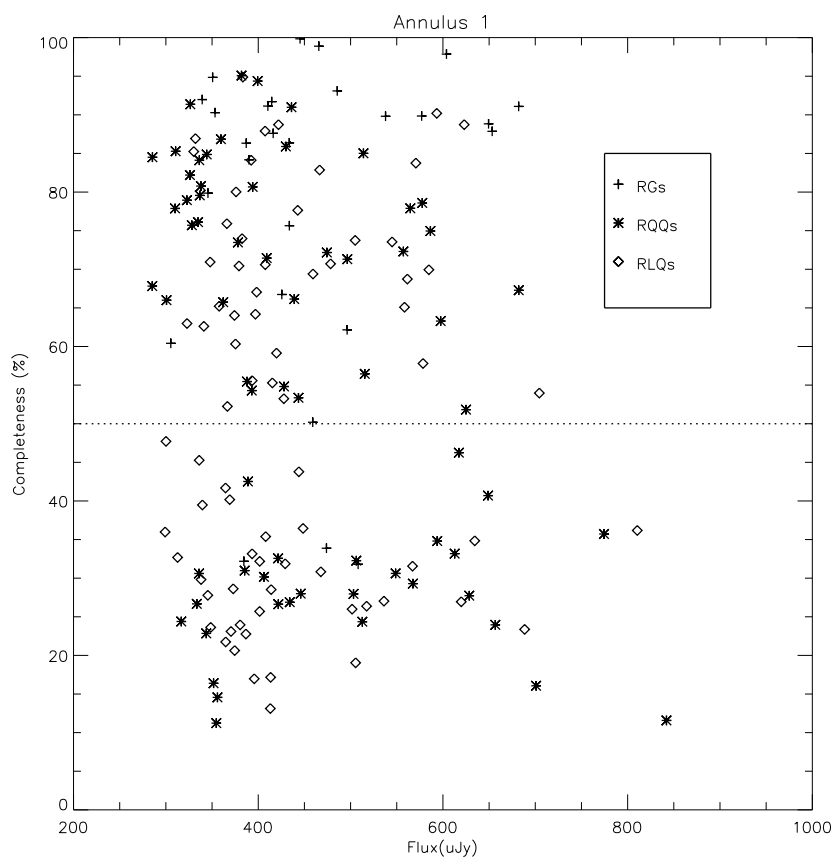
Figure 3.13: The completeness values in annulus 1 versus the 5σ noise for each field. The crosses represent the RGs, the asterisks represent the RQQs and the diamonds represent the RLQs. The dotted line represents the 50 per cent completeness.

bined and a stacking analysis was conducted.

3.4.6 Background Counts
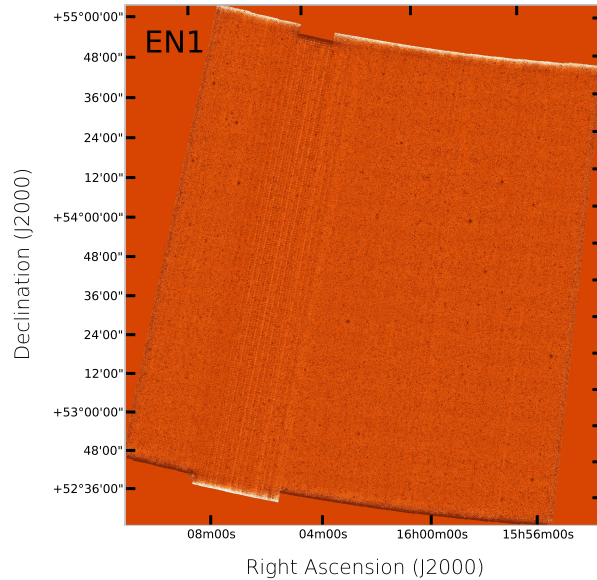
Figure 3.14: Image of the SWIRE E1 field.

To determine whether an overdensity of galaxies was detected around the AGN, the counts were compared to a background field. I used data from the SWIRE survey (Lonsdale et al., 2003a) to calculate the background counts. The ELAIS N1 (E1), ELAIS N2 (E2) and Lockman Hole (LH) fields were used and I performed the same source extraction on these SWIRE fields as I did with the AGN fields, see Figures 3.14, 3.15 and 3.16 for images of these fields. The one additional step was to re-bin the pixel spacing of the SWIRE images from 1.2 to 2.4 arcsec pixels so that they matched the AGN images; this was done using the BLKAVG command in IRAF.

The background source densities in the E1, E2 and LH fields were found to be 0.413 ± 0.0238 arcmin^{-2}, 0.362 ± 0.0244 arcmin^{-2}, and 0.385 ± 0.0235 arcmin^{-2}, respectively. I adopted the mean as the best estimate; 0.387 ± 0.026 sources
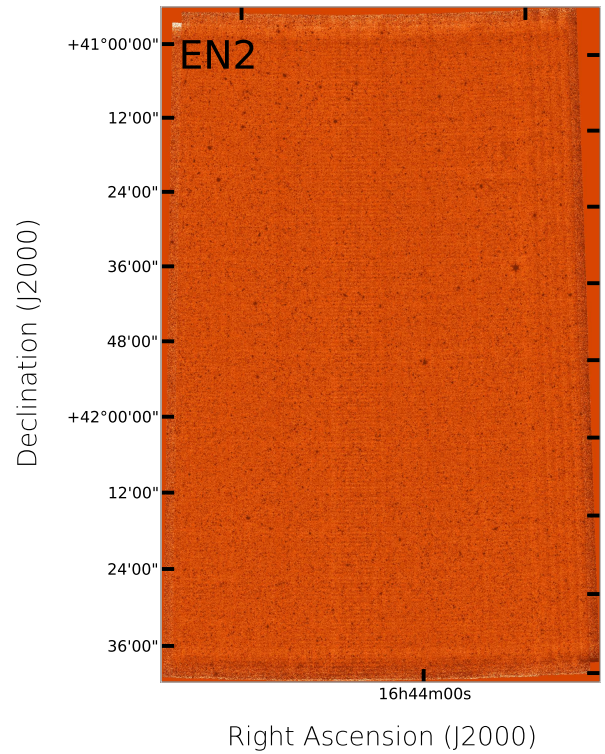
Figure 3.15: Image of the SWIRE E2 field.
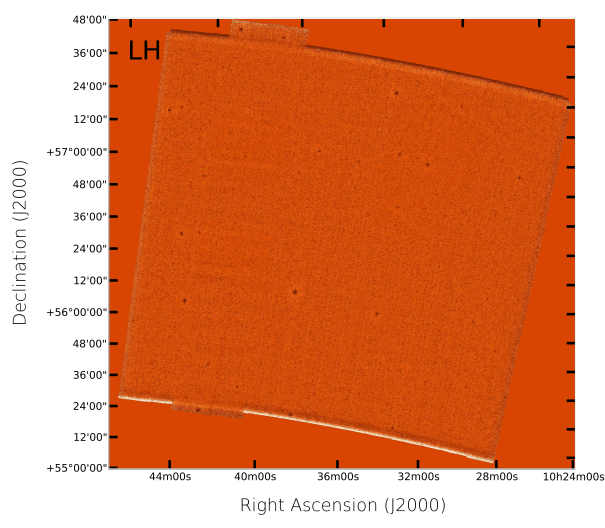
Figure 3.16: Image of the SWIRE LH field.
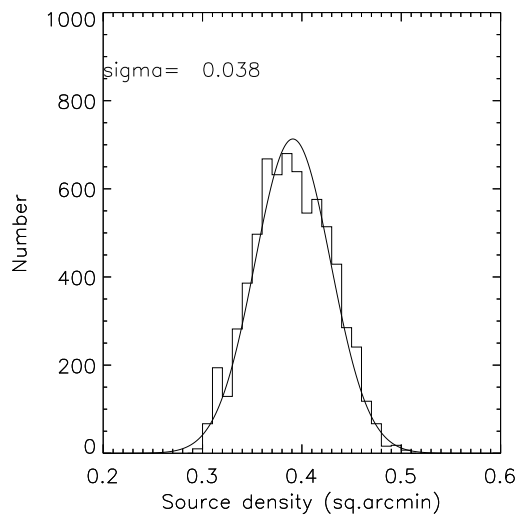
Figure 3.17: Histogram of the background values for the EN1 SWIRE field with the Gaussian fitted.

arcmin^{-2}. The uncertainty on the average background count was found from the Poisson uncertainty.

I investigated whether the cosmic variance uncertainty was significant enough to incorporate it in the uncertainty on the background values. This was done by placing 1000 annuli with a fixed area of 1.396 arcmin^2 on all three SWIRE fields. The cosmic variance is then given by the excess variance over the expectation from a Poisson distrbution:

$$\text{Cosmic Variance error} = (\sigma^2 - \text{Poisson}^2)^{0.5} \tag{3.1}$$

In Table 3.4 I compare the cosmic variance and Poisson uncertainties. From

these it is clear that the Poisson uncertainties completely dominate in individual fields. Therefore, I will only include the Poisson uncertainties hereafter.

Table 3.4: The Poisson and cosmic variance uncertainties for the 3 SWIRE fields.

SWIRE Field	Poisson (arcmin^{-2})	CV (arcmin^{-2})
EN1	0.544	0.153
EN2	0.507	0.102
LH	0.535	0.105

3.4.7 Completeness

In order to compare the source density around the AGN in the sample to the background source density from SWIRE, I determined the completeness as a function of flux density for each of the MIPS observations separately.

The completeness of a field is a measure of how accurately the data represents the distribution of sources in a field. At fainter fluxes there will be an incomplete distribution of faint sources from the data due to noise and obscuration from bright sources. To calculate the completeness for a range of sources I put "fake" sources of known flux into each image and source-extracted the images to get the percentage of "fake" sources detected at each flux. This ensures that the relevant completeness corrections can be made to the source densities for all fields and annuli. This is particularly important at lower flux densities where the corrections can be of the order of 70 per cent for the noisiest images.

Therefore, I inserted 2500 artificial sources into each AGN image and 25000 artificial sources into each of the E1, E2 and LH SWIRE images. The sources were modelled as point sources using the 24μm MIPS point response function scaled to a range of different flux densities between 125μJy and 1500μJy. The
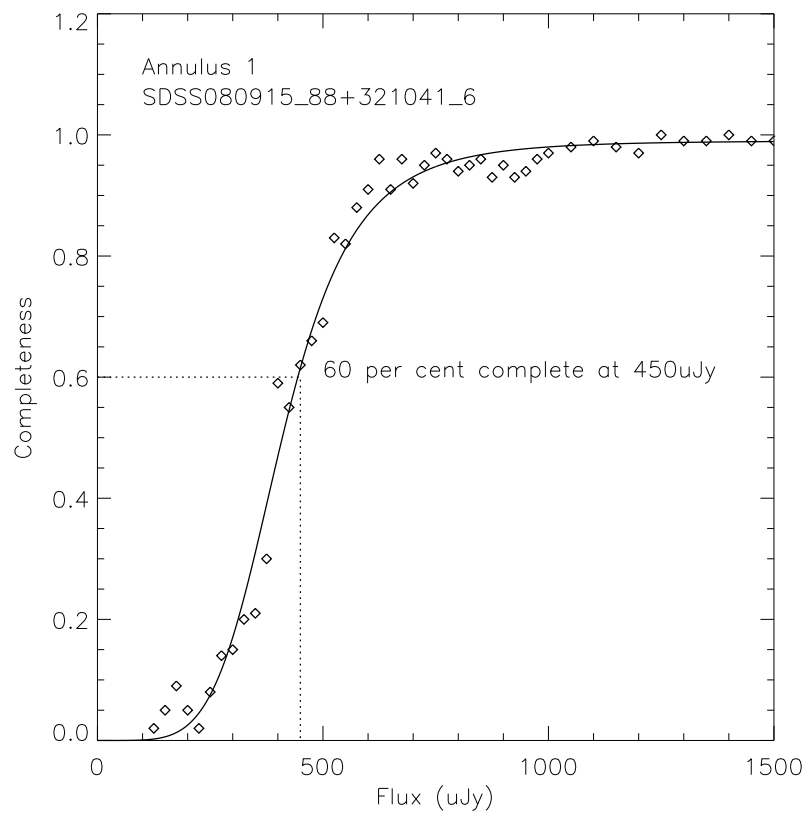
Figure 3.18: An example of a completeness curve in the first annulus of an image with the fitted cumulative distribution function. Our chosen flux-density limit is 450 μJy at 3σ, therefore this is the lowest flux at which I use the completeness correction.

artificial sources were separated, so as not to be blended.

The sources were considered recovered if they were found in the SExtractor

catalogues, were within 1.5 pixels (3.68 arcsecs) of their input position, and had an extracted flux which was within a factor of 2 of their input flux. I determined the completeness for the background fields (E1, E2 and LH) as a function of flux-density only, whereas for the AGN fields I calculated the completeness as a function of separation from the central AGN. This ensured that I can correct for bright objects obscuring regions of certain annuli, especially in the first annulus, where the AGN dominates.

The completeness curves were fitted with an empirical model of the form (Coppin et al., 2006)

$$\text{Completeness} = (S^a)/(b + cS^a) \qquad (3.2)$$

where S is the 24μm flux density and a, b and c are free parameters. An example of a typical completeness curve of a quasar field is shown in Fig 3.18.

I derived the best parametrisation of equation 3.2 for each annulus in the AGN fields; this enabled me to apply a completeness correction for each annulus in each image as a function of flux density. Applying the corrections increased the source density in all of the annuli, although the significance is not changed as the error is also scaled by the completeness correction factor.

3.4.8 Bootstrap Method

To calculate the uncertainties on the completeness corrections I have used the bootstrap method; this was used because the original completeness corrections were not normally distributed so that I needed to resample the completeness corrections to find the error on the mean. For this method I used the original

data set of the completeness corrections (in each annulus) of a certain size and made a new sample, called the bootstrap sample that was of the same size. This new sample was taken from the original using sampling with replacement, so that it was not identical with the original completeness correction sample. Each new sample was summed up to give the total completeness correction in each annulus. I repeated this 1000 times to get a distribution of total completeness corrections as a function of annulus, and for each of these bootstrap samples I computed the mean. I then created a histogram of all of the bootstrap means. This provided an estimate of the shape of the distribution of the mean and by using a Gaussian fit the standard deviation was estimated. This process was carried out for each AGN type and for each annulus. I derived a probability distribution for each annulus, see Figures 3.19, 3.20, 3.21, 3.22 and 3.23 for the bootstrap histograms of annulus 1, 2, 3, 4 and 5. These bootstrap uncertainties were then added, in quadrature, with the Poisson uncertainties.

3.5 Density Results

3.5.1 Whole Sample and Subsamples

The source density (N) has been found by counting the number of sources detected above the flux-density cut in each annulus and for each AGN type. The uncertainty on the source density is the Poisson uncertainty, added in quadrature, with the bootstrap uncertainty. I calculate the source overdensity (ΔN) for the
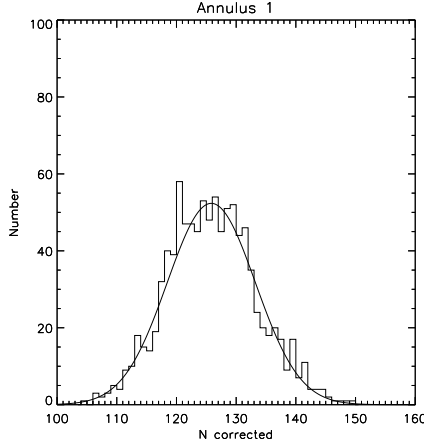
Figure 3.19: The total completeness corrections in annulus 1, which have been resampled with replacement. The bootstrap uncertainty is $\sigma = 7.09$. The total completeness correction from the actual data is 126.0 and this matches up with the mean of the bootstrap sample.

complete sample and for the AGN subsamples, in all annuli, using;

$$\Delta\mathrm{N} = (N_{AGNfields} - N_{Swire}) \tag{3.3}$$

where $N_{AGNfields}$ is the source density in the AGN fields and N_{Swire} is the source density in the background SWIRE fields.

The total of the galaxy counts in the AGN fields, in the first annulus, shows a slight overdensity of 0.148 ± 0.072 arcmin^{-2}, but at a low significance (2σ) above the background field count (see Figure 3.24 and Table 3.5). Therefore I cannot say that I have a significant detection of galaxies over the expected background values.
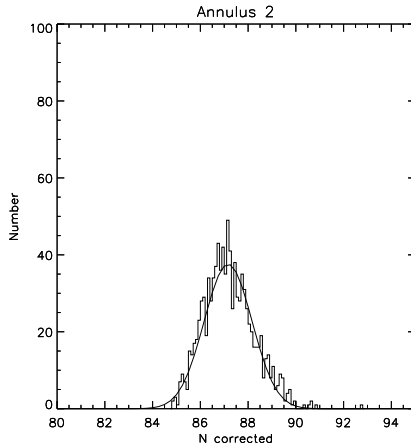
Figure 3.20: The total completeness corrections in annulus 1, which have been resampled with replacement. The bootstrap uncertainty is $\sigma = 0.97$. The total completeness correction from the actual data is 87.2 and this matches up with the mean of the bootstrap sample.

I have compared my source overdensities with those of Falder et al. (2010), who used the same AGN sample but at 3.6μm. This traces evolved stellar populations rather than star-forming galaxies. The source overdensity was found using the same method as used by Falder et al. (2010). The 3.6μm source overdensities have been completeness corrected and background subtracted and I used the same sized annuli as the 24μm data. This allows for a direct comparison between the two data sets. The histogram of the overdensity for the complete sample of AGN fields can be found in Figure 3.28. The 24μm source overdensity (bold line) is clearly lower than what was found by Falder et al. (2010), who used data at 3.6μm, and found a factor of ~ 2 overdensity at a significance of $> 8\sigma$ (dashed-dotted line). Falder et al. (2010) found, on average, a factor of 12.2 ± 6.1
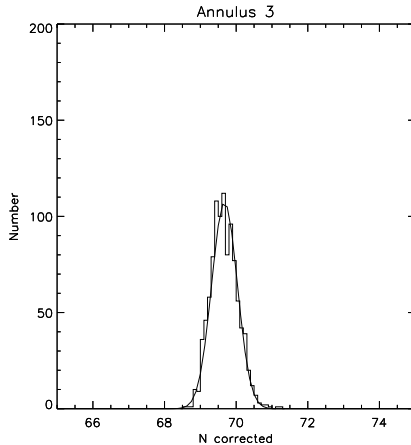
Figure 3.21: The total completeness corrections in annulus 1, which have been resampled with replacement. The bootstrap uncertainty is $\sigma = 0.34$. The total completeness correction from the actual data is 69.7 and this matches up with the mean of the bootstrap sample.

more galaxies per square arcmin within 40 arcsec of their AGN compared to my results. Their fields are much more dense at 3.6μm compared to the same fields at 24μm. However, it is important to stress that the two surveys are sensitive to very different classes of object so that these numbers are not directly comparable.

To see if there is a trend with AGN type I split the sample into the three types of object present in the sample: RQQs, RLQs and RGs. I find that there are no significant source overdensities around the RLQs and RQQs within the 300 kpc region of the central AGN. The RLQs have an overdensity of 0.224 ± 0.126 arcmin^{-2} at a significance of 1.8σ and the RQQs have an overdensity of 0.150 ± 0.102 arcmin^{-2} at a significance of 1.48σ (see Fig 3.25 for the RGs, Fig 3.26 for the RQQs, Fig 3.27 for the RLQs and Table 3.5 for the statistics). Further-
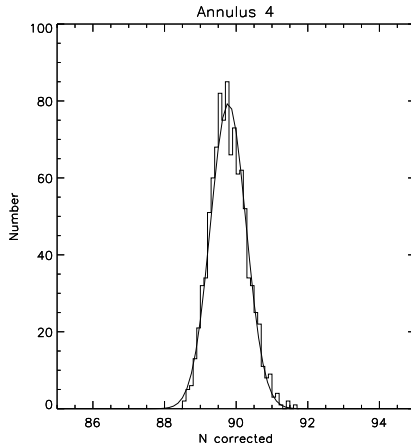
Figure 3.22: The total completeness corrections in annulus 1, which have been resampled with replacement. The bootstrap uncertainty is $\sigma = 0.47$. The total completeness correction from the actual data is 89.8 and this matches up with the mean of the bootstrap sample.

more, the RGs have no significant source overdensity, -0.071 ± 0.099 arcmin^{-2} within the 300kpc region.

I also compared the source density distribution, in the first annulus, of each AGN type and the combined QSOs by performing a two-sample Kolmogorov-Smirnov test (K-S Test) and a Mann-Whitney U-Test (M-W Test). The significances of these tests are found in Table 3.6. The most significant results are from the K-S tests. These show that the RGs and the RLQs, are drawn from different distributions at the 3σ confidence level, the RGs and the RQQs are drawn from different distributions at the 2.5σ confidence level and the RGs and the combined QSOs are drawn from different distributions at the 4.5σ confidence level. See Figure 3.29 for the histograms of the source densities of the combined
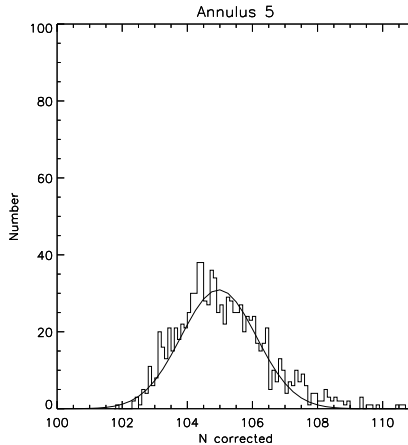
Figure 3.23: The total completeness corrections in annulus 1, which have been resampled with replacement. The bootstrap uncertainty is $\sigma = 1.31$. The total completeness correction from the actual data is 105.1 and this matches up with the mean of the bootstrap sample.

QSOs and the RGs. However the M-W test, which determines if the two medians are drawn from the same population, does not detect a significant difference (1.5σ) of the RGs and the QSOs having different medians. This is because both distributions of source densities have the same medians but a different shape in the distributions. It is difficult to say that there is an overdensity of galaxies within 300kpc of the AGN for the QSOs but there does seem to be a statistically significant difference between the RGs and the QSOs distributions, even though neither of them have a significant source overdensity, in the sense that there are no RGs with significant individual measured overdensities. A possible reason why the K-S tests show significant differences in the distribution of source densities between the AGN samples when there is no overall significant detection
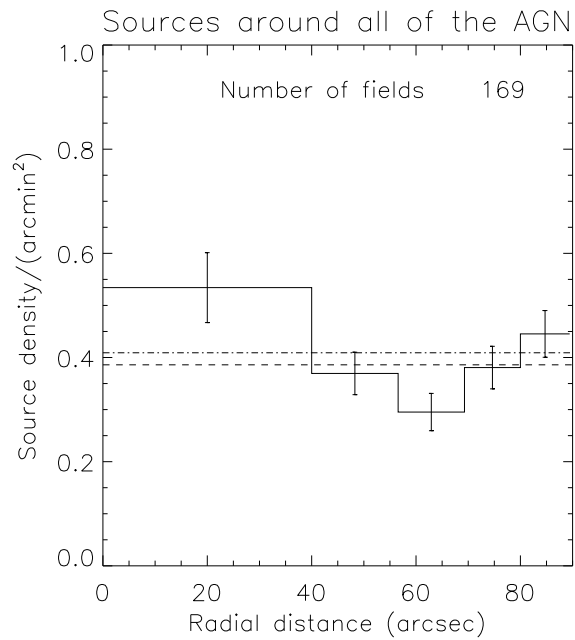
Figure 3.24: Histogram showing the average source density for all of the AGN fields with the flux-density cut of 450μJy. The dashed line represents the background level. The dashed dotted line represents the average source density, for the total area of 6.91 arcmin^2 for all of the annuli.

of overdensity could be that there is a tail of objects that have large clustering values (See Fig 3.29). These are detected when comparing the source overdensity distributions, giving significant K-S test results but would be overwhelmed when averaging the source overdensity in each radial bin. Further interpretation of these results will be discussed in Section 3.7.
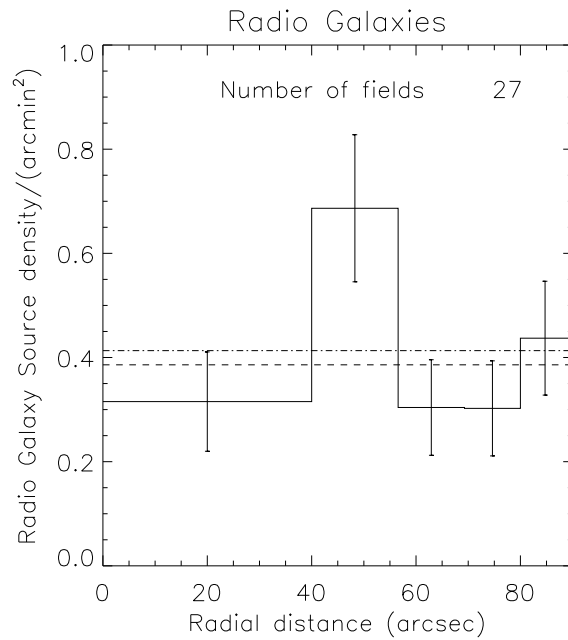
Figure 3.25: Histograms showing the average source density for the RGs with flux cut of 450μJy. The error bars for each field are the Poisson errors for each bin added in quadrature with the bootstrap errors. The dashed line represents the background level. The dotted dashed line represents the average source density for the total area of 6.91 arcmin^2 for all of the annuli.

3.5.2 The Star-Formation Rates

In order to interpret my results I need to calculate what star-formation rate (SFR) Spitzer is sensitive to in these data.

I use the SFR relation of Chary & Elbaz (2001) which converts the rest-frame luminosity at 12μm into a total infrared luminosity (L_{IR}) and hence a SFR. This
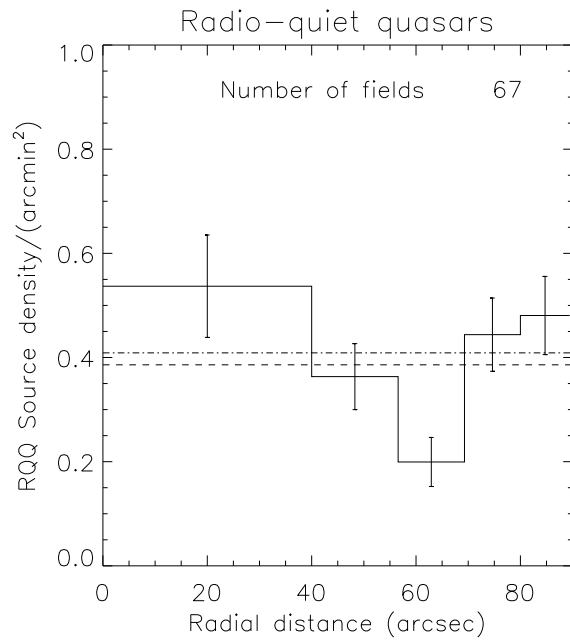
Figure 3.26: Histograms showing the average source density for the RQQs with flux cut of 450μJy. The error bars for each field are the Poisson errors for each bin added in quadrature with the bootstrap errors. The dashed line represents the background level. The dotted dashed line represents the average source density for the total area of 6.91 arcmin^2 for all of the annuli.

relation is valid for $L_{\mathrm{IR}} > 10^{10}$ L$_\odot$ and is given in equation 3.4;

$$L_{IR} = 0.89^{+0.38}_{-0.27} \times L_{12\ \mu m}^{1.094}.\tag{3.4}$$
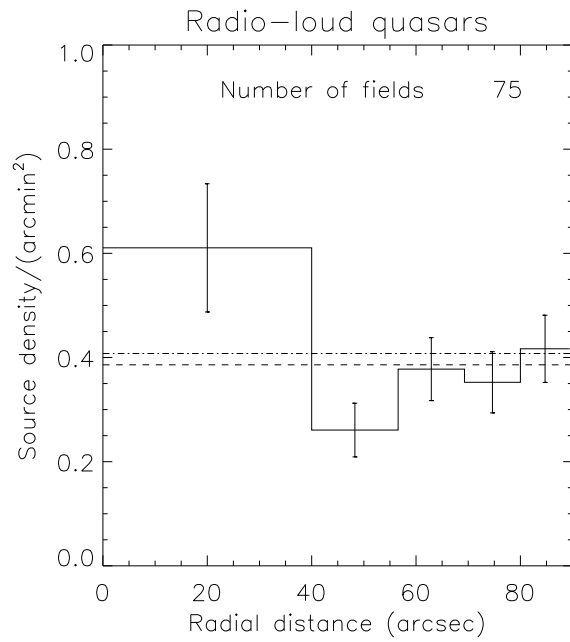
Figure 3.27: Histograms showing the average source density for the RLQs with flux cut of 450μJy. The error bars for each field are the Poisson errors for each bin added in quadrature with the bootstrap errors. The dashed line represents the background level. The dotted dashed line represents the average source density for the total area of 6.91 arcmin^2 for all of the annuli.

The star-formation rate is then given by

$$\text{SFR } (\text{M}_\odot \text{ yr}^{-1}) = 1.71 \times 10^{-10} \; L_{\text{IR}} \; (\text{L}_\odot). \tag{3.5}$$

At $z = 1$ the limiting flux density of 450 μJy corresponds to a rest-frame 12μm luminosity of 7.55×10^{10} L$_\odot$. Substituting this value into equation 3.4 gives a

Table 3.5: The source density in each annulus for the complete sample and the RG, RLQ and the RQQ sub-samples using the flux-density cut of 450μJy. The Poisson uncertainties and bootstrap uncertainties are added in quadrature. The source overdensity (ΔN) has been calculated using Equation 3.3 for the full sample and for each AGN type using the flux-density cut of 450μJy. The average background count from the SWIRE fields has been subtracted from the source density in the first annulus. The uncertainties are the Poisson uncertainties that are added in quadrature with the uncertainty from the average SWIRE background count and the bootstrap uncertainties. The significance σ is the number of 1σ error bars that the source overdensity is above zero.

Sample	N	±Error	ΔN	±Error	σ
Complete A1	0.534	0.067	0.148	0.072	2.038
Complete A2	0.371	0.041	-0.016	0.049	-0.329
Complete A3	0.296	0.036	-0.091	0.045	-2.037
Complete A4	0.381	0.041	-0.0050	0.049	-0.112
Complete A5	0.446	0.045	0.059	0.052	1.140
RGs A1	0.316	0.095	-0.071	0.099	-0.717
RGs A2	0.688	0.141	0.301	0.144	2.092
RGs A3	0.305	0.092	-0.082	0.096	-0.860
RGs A4	0.303	0.091	-0.084	0.095	-0.881
RGs A5	0.437	0.109	0.051	0.113	0.451
RLQs A1	0.611	0.123	0.224	0.126	1.778
RLQs A2	0.262	0.052	-0.125	0.058	-2.149
RLQs A3	0.379	0.061	-0.008	0.066	-0.121
RLQs A4	0.353	0.059	-0.034	0.064	-0.524
RLQs A5	0.417	0.065	0.030	0.070	0.437
RQQs A1	0.537	0.098	0.150	0.102	1.476
RQQs A2	0.365	0.064	-0.022	0.069	-0.319
RQQs A3	0.200	0.047	-0.187	0.054	-3.454
RQQs A4	0.445	0.070	0.058	0.075	0.769
RQQs A5	0.482	0.075	0.095	0.080	1.192
All complete	0.406	0.021	0.049	0.034	1.451
All RGs	0.410	0.048	0.059	0.055	1.080
All RLQs	0.404	0.034	0.045	0.043	1.053
All RQQs	0.406	0.033	0.049	0.042	1.166

total infrared luminosity, $L_{\mathrm{IR}} = 7.078 \times 10^{11}$ $L_\odot$ which is in the Luminous Infrared Galaxy (LIRG) regime and in the luminosity range where the adopted method

Table 3.6: Statistical tests for the source densities of different combination of the AGN types within 300kpc of the central AGN. The significance shown is the confidence level at which the null hypothesis can be rejected.

Comparison	KS Tests	MW Tests
RGs vs RLQS	0.996	0.803
RGS vs RQQs	0.988	0.792
RQQs vs RLQs	0.311	0.589
RGs vs all QSOs	0.999	0.816

is valid (see Fig. 1 of Elbaz et al. 2010). Substituting L_{IR} into equation 3.5, I find the limiting SFR of the survey to be 121^{+51}_{-37} $M_\odot$ yr^{-1} where the quoted error comes from the 1-σ scatter around the relation in equation 3.4.

This method of using mid-infrared observations to determine the total infrared luminosity has been verified by Elbaz et al. (2010) using new far-infrared data from the *Herschel Space Telescope* (Pilbratt et al., 2010). They directly compare the total infrared luminosity calculated with *Herschel* data to the total infrared luminosity calculated from the 24μm data alone, using the method described by Chary & Elbaz (2001). They find that the mid-infrared flux density is a robust indicator of total infrared luminosity for objects with $L_{IR} \lesssim 10^{12}$ $L_\odot$ and $0 \leq z \leq 1.5$, quoting a dispersion of only 0.15 dex. Therefore I can use the Chary & Elbaz (2001) relation with confidence.

It is important to check that AGN do not contaminate the limits I place on the star formation. To determine the expected number of QSOs at $z \sim 1$, I used the correlation between absolute i-band magnitude (M_i) and 24μm flux-density ($S_{24\mu m}$) to find the absolute i-band magnitude that corresponds to the 450μJy flux-density limit. The M_i which corresponds to a 450μJy flux-density limit is $M_i = -22.1$. Using the luminosity function of Croom et al. (2009), corrected to the i-band, I find that I expect 14 QSOs per sq.deg, which equates to ~ 0.03
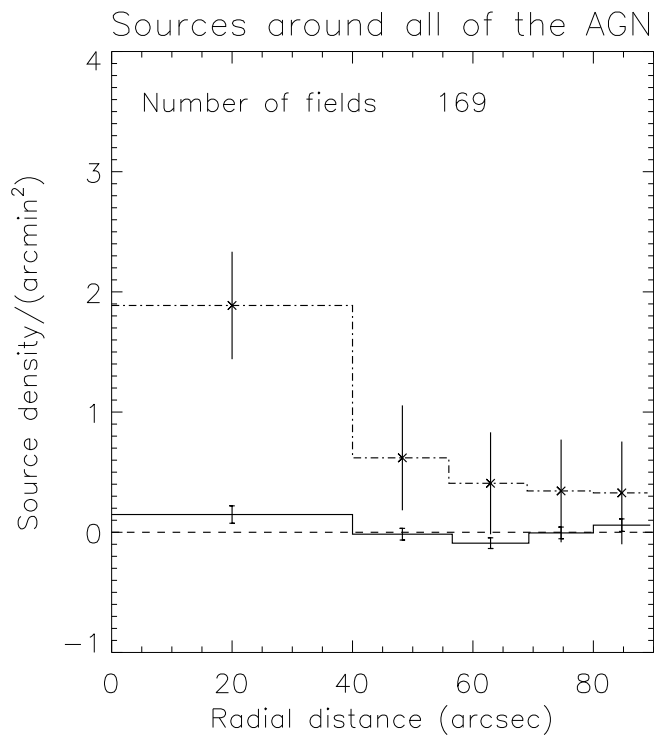
Figure 3.28: Histogram showing the 3.6μm and 24μm average source overdensity for all of the AGN fields as a function of radius from the AGN. The bold lines are the 24μm over-densities and the dashed-dotted lines are the 3.6μm over-densities. Both profileshas been completeness corrected and the local background has been subtracted. The error bars are the Poisson errors for each bin, which have been added in quadrature with the Poisson error on the blank field level. The dashed line shows the zero level where there is no overdensity.

QSOs per AGN field and 0.0054 QSOs per annulus. I find that approximately 1 per cent of the objects detected in the first annulus will be QSOs for the complete
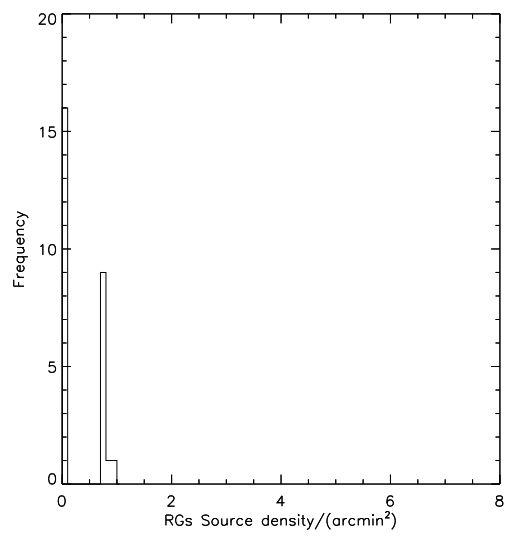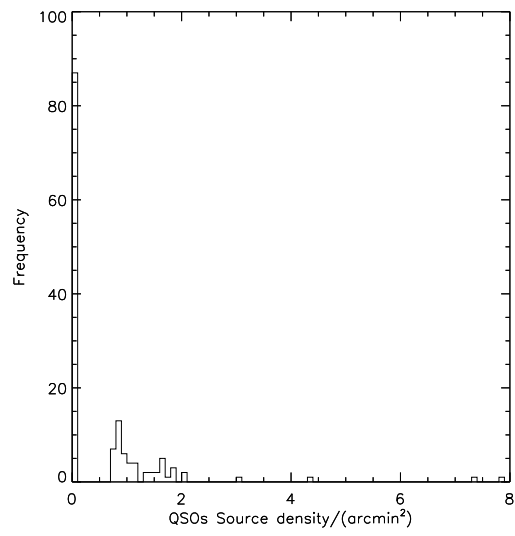
Figure 3.29: Histograms of the individual source densities for each field for the QSOs and the RGs.

sample and this fraction is only ~ 3 per cent for the lowest detected source density (RQQs (A2): 0.2 arcmin^{-2}). Therefore it is likely that the vast majority of the 24μm sources that are detected are from star-forming galaxies rather than AGN.

3.6 Galaxy Colours in the AGN Environments

In this section I investigate the distribution of galaxy colours in the environments of the AGN sample. This was done by comparing the 24μm and 3.6μm catalogues; sources were counted as matching in the two catalogues if the coordinate offsets were within 2 pixels or 4.9 arcseconds of the 24μm source position. To compare the 24μm with the 3.6μm AGN fields I needed to use a flux-density limit for the source selection. For the 24μm fields I selected galaxies with fluxes above the 3σ flux limit of $f_{24\mu\mathrm{m}} > 450\mu$Jy. For the 3.6$\mu$m fields I selected galaxies with fluxes above the 8σ flux limit of $f_{3.6\mu\mathrm{m}} > 20.0\mu$Jy, which is a more conservative flux-density cut than the flux cut of 13.1μJy at 5σ used by Falder et al. (2010). This ensured that the 3.6μm sample does not suffer from incompleteness and that there is no need to use completeness corrections. I also ensured that the central AGN was not included in the source counts.

3.6.1 The SWIRE Field Colours

I found the average colour of galaxies in a general field which had corresponding 24μm and 3.6μm data. I used the average galaxy colours from the EN1, EN2 and LH SWIRE fields. A KS test was carried out to compare the colours of galaxies in these fields; the probability, p, gives the probability level of the test and ranges between 0 and 1. The lower the probability value, the more likely the

null hypothesis can be rejected, where the null hypothesis states that the samples are drawn from the same distribution. The null hypothesis probability was 0.81 when I compared EN2 and Lockman Hole fields, 0.449 when I compared EN1 and EN2 fields and 0.87 when I compared EN1 and Lockman Hole fields. For the colours in these fields the probability of the null hypothesis was close to 1, and so there is no evidence that their colour distributions differ. Therefore, all 3 fields will be able to be used as an estimate of the general background galaxy colours that I would expect in the AGN fields.

3.6.2 Statistical Tests

To investigate any differences in the galaxy colour distribution between the AGN field galaxies and the SWIRE background galaxy colours a K-S test was performed. The significance of the test can be found in Table 3.7; a K-S test was performed on 5 annuli over all of the AGN fields. There were no significant differences between the galaxy colours in the different annuli and therefore we could not reject the null hypothesis. K-S tests were then performed over the different AGN fields as a function of distance from the central AGN and total annuli area. These show that there is no significant difference between the galaxy colour distribution for each annulus and the colour distribution of the SWIRE fields.

However, I do find evidence that the Annulus 1+2 (24μm -3.6μm) colours of the galaxies within the RG environments are different to the SWIRE field at the 98.9% confidence level.

I also use K-S and M-W tests to compare the galaxy colours between the different AGN types and the combined QSOs. See Table 3.8 for the confidence

Table 3.7: The K-S test results for the excess galaxy colours compared to the SWIRE galaxy colours.

Annuli	Null Hypothesis Probability
ALL	
Annulus 1	0.062
Annulus 2	0.329
Annulus 3	0.965
Annulus 4	0.888
Annulus 5	0.846
RGs	
Annulus 1+2	0.011
Annulus 3+4	0.853
Annulus 4+5	0.631
All	0.170
RLQs	
Annulus 1+2	0.361
Annulus 3+4	0.058
Annulus 4+5	0.925
All	0.862
RQQs	
Annulus 1+2	0.410
Annulus 3+4	0.068
Annulus 4+5	0.670
All	0.261

levels between each of the comparisons. I find that the colours of the galaxies within the 300kpc of the RGs versus the combined QSOs are drawn from different populations at the $\sim 3\sigma$ confidence level and the median colour values are different at $\sim 2.5\sigma$, although, the true significance of these differences maybe lower due to the number of trials I have made. Therefore, the colours of the galaxies within the 300kpc region of the RGs are possibly different to those in the same annuli around QSOs and the background. This could be due to the radio galaxies influencing their environments; this will be discussed in Section 3.7.

Table 3.8: Statistical tests for the colours of different combination of the AGN types within 300kpc of the central AGN. The significance shown is the confidence level at which the null hypothesis can be rejected.

Comparison	K-S confidence level	M-W confidence level
RGs vs RLQS	0.891	0.920
RGS vs RQQs	0.891	0.956
RQQs vs RLQs	0.463	0.671
RGs vs all QSOs	0.988	0.959

3.7 Discussion

I have found that the large sample of 169 AGN have no significant 24μm overdensities associated with them in their 300kpc environments when compared to the SWIRE field galaxies. For the whole sample, I only found 0.148 ± 0.072 arcmin^{-2} source overdensity at 2σ within the 300kpc region of the AGN for galaxies with $f_{24\mu m} > 450\mu$Jy or a SFR of ~ 120 M$_\odot$ yr^{-1}.

This result contrasts with previous results by Falder et al. (2010), who used the same AGN sample but with 3.6μm data; they found the AGN environments within the 300kpc region to be more dense when compared to the field. They concluded that there is a substantially evolved population of two to three massive galaxies associated with each AGN, with a $> 8\sigma$ excess relative to the field. Along with this substantial evolved stellar population, I have found that there is no significant excess of star-forming galaxies associated with each AGN above a SFR limit of ~ 120 M$_\odot$ yr^{-1}.

3.7.1 Difference in the Environments in Type 2 (RGs) and Type 1 Quasar Environments

I have compared the distribution of source densities for the RGs against the source densities of the QSOs and I found that they are drawn from different distributions at the $\sim 4.5\sigma$ confidence level. Even though I do not detect significant source densities within each annulus there was a difference between the source density distributions. I investigated the distribution of S(24μm/3.6μm) colours of the galaxies within the vicinity of the RGs and I found that they have a $\sim 3\sigma$ significance of being drawn from different populations when compared to the background SWIRE colours and a $\sim 2.5\sigma$ signififcance of them being drawn from different populations when compared to the galaxy colours detected around the QSOs.

One possible reason for these differences could be that low-excitation RGs (LEGs), which are fueled by hot gas, generally inhabit rich environments which predominantly consist of older stellar populations rather than star-forming galaxies (Hardcastle, 2004; Hardcastle et al., 2012). However, only a small number of RGs were classified as LEGs in the sample; the majority are high-excitation RGs (HEGs). I was unable to determine whether the emission line class of RGs is related to the RG's environment. However, the RGs were found to reside in rich environments with older stellar populations compared to the RLQs and RQQs, which were found to reside within environments with both evolved stellar populations and star-forming galaxies.

Therefore, I suggest that the differences found in the 24μm source density between the AGN types were due to them residing in different environments, as

traced by the 3.6μm data. The RGs reside in the densest environments, which suppress star formation, whereas the RLQs/RQQs reside in less dense environments which allowed for more star formation. More sensitive observations are required to test this tentative conclusion, but I will return to the idea that radio-loudness traces a rich environment in Chapters 5 and 6.

Chapter 4

Classification of QSOs in the VIDEO Data

4.1 Introduction

A large number of quasars have been discovered since their first discovery by Schmidt (1963). Since then, 10,000 spectroscopic quasars have been catalogued by Croom et al. (2001) in the 2dF Quasar Redshift Survey (2QZ; Boyle et al. 2000) and currently there are more than a million quasars classified by Richards et al. (2009) in the Sloan Digital Sky Survey (SDSS; Adelman-McCarthy et al. 2008).

Previous surveys, such as SDSS, find optically selected quasars; however, there is a limit of $z < 6.5$ for optical surveys because there is no flux below Ly α due to the Gunn-Peterson trough, and so near-infrared (NIR) surveys are used to expand QSO detections to higher redshifts. The Two Micron All-Sky Survey (2MASS; Skrutskie et al. 2006) is the largest NIR survey but is too shallow, at a

depth of $J \sim 16.6$, to detect high redshift quasars (HZQs). The UKIRT (United Kingdom Infrared Telescope) Infrared Deep Sky Survey (UKIDSS; Lawrence et al. 2007) reaches depths of $Y = 20.3$, $J = 19.5$, $H = 18.6$ and $K = 18.2$ (Warren et al., 2007) and has already found several $z > 6$ quasars (Venemans et al. 2007; Mortlock et al. 2009; Venemans et al. 2012) and one $z > 7$ quasar (Mortlock et al., 2012). The new Visible and Infrared Survey Telescope for Astronomy (VISTA; Emerson et al. 2004) surveys, which this project uses, will be able to extend the UKIDSS results in large numbers at high redshifts.

However, not only is it necessary to have surveys with appropriate depth and area to detect QSOs, it is also necessary to be able to distinguish QSOs from stars, brown dwarfs, and galaxies. This is where the challenge of QSO detection lies.

Machine learning techniques, such as the use of artificial neural networks, have previously been successful at calculating the photometric redshifts of objects (Firth et al. 2003; Collister & Lahav 2004). They were originally used to classify stellar spectra (von Hippel et al., 1994). Large data-sets, such as SDSS (York et al., 2000), have used neural networks for morphology classifications. More recently, Banerji et al. (2010) have used neural networks to reproduce the morphology classifications of the Galaxy Zoo objects (Lintott et al., 2008). They were able to reproduce the human classifications for the Galaxy Zoo objects to better than 90 per cent in three morphology classes. The neural network is able to classify galaxies more efficiently compared to human classification of the Galaxy Zoo objects, which makes it a valuable technique to use to classify objects in large surveys.

In this chapter, I explain how I used artificial neural networks to classify

objects as either galaxies or QSOs in the VIDEO data. Using neural networks as opposed to colour and magnitude selection techniques I avoid the problems of rejecting possible QSO candidates at the edge of selection regimes. I described the VIDEO survey in Chapter 2. In Section 4.2 the artificial neural network method is presented. In Section 4.3 I show the possible QSO candidates. In Section 4.4 I explain the stellar locus removal and a comparison to a colour-selected QSO sample is presented in Section 4.5. In Section 4.6 I present the main conclusions. All magnitudes are quoted in the AB system unless stated otherwise.

4.2 Artificial Neural Networks

In this section I outline the main methods of selecting quasars and galaxies from the VIDEO survey using an artificial neural network.

4.2.1 The ANNz Code

I use the artificial neural network code ANNz (Ripley 1981; Ripley 1988; Lahav et al. 1995; Naim 1995; Collister & Lahav 2004) to classify objects in the VIDEO data. This is one of many tools that is primarily used to estimate photometric redshifts but I use it for the classification of objects. A comparison between these tools is given by Hildebrandt et al. (2010), who show that ANNz seems to perform similarly to other codes for the estimation of photometric redshifts. I chose the ANNz code because it is well-documented and easy to set up.

Generally, the aim of a neural network is to use an existing relationship between an input vector x and a target t. ANNz uses this relationship to learn a model of the training set and to produce an output y, which is close to the target
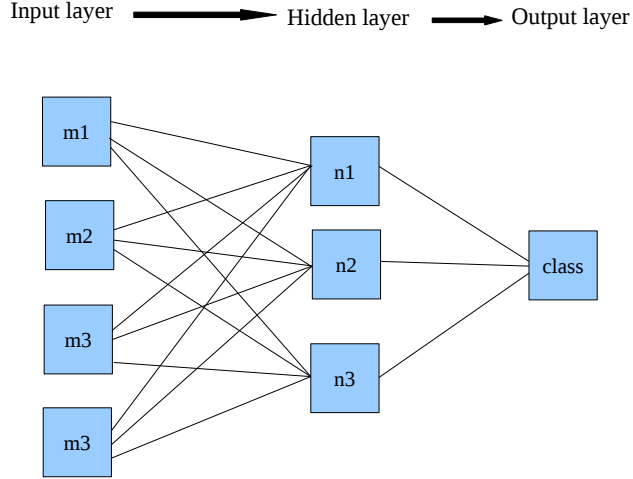
Figure 4.1: This illustration represents the setup of the ANNz code, where the input layer is the input magnitudes in different wavebands, the hidden layer is the chosen architecture and the output is the object class.

value t. These trained networks can then be used to estimate the classification of unknown objects in a sample.

ANNz is made up of a number of nodes contained in several layers, as shown in Figure 4.1. The first layer receives the input parameters, which are the known objects with an existing relationship, and the last layer gives the output, which is the classification of the unknown objects. All the hidden layers/nodes in between the input and output layers are interconnected and have associated weights. A training set is used to minimise the cost function, which is given by

$$E = \Sigma_k (z_{\mathrm{phot}}(w, m_k) - z_{\mathrm{spec,k}})^2 \qquad (4.1)$$

where w denotes the weights, $z_{photo}(w, m_k)$ is the network output for the given input and weight vectors, and the sum is over the galaxies/quasars in the training set.

To avoid over-fitting to the training set a separate *validation* set is used, which is a smaller part of the training data. This is done by evaluating the cost function on the *validation* set after each training iteration. Once the training terminates, after a chosen number of iterations, the final weights are chosen. These are chosen where the cost function is minimal on the *validation* set; for a full description see Collister & Lahav (2004).

The architecture of the neural network needs to be defined; it sets up how many layers to use and how many nodes are in each layer. For the neural network set-up I used 22 input nodes, which are the number of filters used with their associated uncertainty. These include photometric data in the bands u, g, r, i , z, Z, Y, J, H, K_s with their uncertainties, spectroscopic redshifts and object type. I used two hidden layers with 20 nodes each and two output nodes, object classification (0 for a galaxy and 1 for a QSO) and photometric redshift estimates. I found that this architecture used the optimum number of nodes, after experimenting with different setups. This was determined by running ANNz on the training data using different architectures and choosing the setup which produced the highest number of accurate classifications.

4.2.2 Input Parameters

For ANNz to accurately classify objects in the VIDEO data, I needed a sample of spectroscopically confirmed QSOs and galaxies with spectroscopic redshifts in the

training sets. This ensures that the neural network can learn which objects are QSOs and galaxies from accurately classified QSOs and galaxies in the training data. They also need to have data in the same near-infrared and optical bands as the VIDEO data because the choice of input parameters is crucial in determining how well ANNz can perform.

4.2.3   The Test Set

The VIDEO survey covers the VIDEO-XMM3 field, therefore I chose the VIMOS VLT Deep survey (VVDS, Gavignaud et al. 2006) for the initial training data. The VVDS, which also has coverage of the VIDEO-XMM3 field, is a deep 4 square degree survey with spectroscopically determined QSOs and their associated redshifts; this survey is described further in Chapter 2. This survey is used because it has spectroscopically determined QSOs and galaxies that are in the VIDEO field and which could be matched with the VIDEO objects to ensure the training data has exactly the same optical and near infrared data as the VIDEO catalogue.

I split the VVDS data into training, validation and test sets. The test set is a randomly selected sample from the training data. This is used for a comparison between the output classifications and the inputs, from the training sample, which ensured that the neural network was working accurately.

The VVDS data provided only 62 QSOs compared with 8011 galaxies. The more QSOs I have in the training sample the better the neural network will classify the quasars in the VIDEO data. I found additional QSOs from the SDSS and 2SLAQ; these gave me a list of QSO positions that I could then match with the

VIKING survey to obtain their near infrared photometry. The VIKING survey was used because it is a VISTA survey which uses the same near-infrared bands as the VIDEO data; more details on this survey can be found in Chapter 2. I then matched the QSO positions with the SDSS data (Data Release 7, Abazajian et al. 2009) to get accurate photometry.

I added slight corrections to the SDSS photometry and the VIKING near-infrared bands to make them similar to the CFHT optical and VIDEO near-infrared bands. The SDSS optical bands were corrected to the CFHTLS photometry using the following corrections:

$$u_{\mathrm{CFHTL}} = u_{\mathrm{SDSS}} - 0.241(u_{\mathrm{SDSS}} - g_{\mathrm{SDSS}}),$$

$$g_{\mathrm{CFHTL}} = g_{\mathrm{SDSS}} - 0.153(g_{\mathrm{SDSS}} - r_{\mathrm{SDSS}}),$$

$$r_{\mathrm{CFHTL}} = r_{\mathrm{SDSS}} - 0.024(g_{\mathrm{SDSS}} - r_{\mathrm{SDSS}}),$$

$$i_{\mathrm{CFHTL}} = i_{\mathrm{SDSS}} - 0.085(r_{\mathrm{SDSS}} - i_{\mathrm{SDSS}}),$$

$$z_{\mathrm{CFHTL}} = z_{\mathrm{SDSS}} + 0.074(i_{\mathrm{SDSS}} - z_{\mathrm{SDSS}}). \tag{4.2}$$

Details of how these were derived can be found on the web[1]. I then added a 2 per cent uncertainty to the statistical measurement errors to account for systematic uncertainties in all wavebands. All wavebands were then extinction corrected and the VIKING bands were corrected to the VIDEO apertures because they used 2.8 arcsec apertures whilst the VIDEO data used 3 arcsec apertures. I carried out this correction by cross-matching the VIDEO data with the VIKING data, finding where the two surveys overlapped (RA: 36.0 to 37.0 degrees and

---

[1]http://www3.cadc-ccda.hia-iha.nrc-cnrc.gc.ca/community/CFHTLS-SG/docs/extra/filters.html

Dec: -5 to -4.95 degrees), and then subtracting the mean difference of the flux values for each waveband between the VIKING and VIDEO wavebands.

This photometry made up the training, validation and test sets, which I then used to train the ANNz network. In total I used 9387 objects in the training set, including 1314 SDSS/2SLAQ QSOs, 62 VVDS QSOs and 8011 VVDS galaxies, all with spectroscopic redshifts. Once the network was trained I then used it with the VIDEO data, for which there is no prior redshift information, to estimate the photometric redshifts and, more importantly for the present project, the classification of the objects in the VIDEO data.

4.3 The Quasar Candidates

4.3.1 Results of ANNz on the Test Set

I randomly split the spectroscopically confirmed quasar/galaxy sample into training, validation and test data. I then ran ANNz on the full test set to enable a classification for all the known galaxies and quasars. This was done to check the accuracy of the ANNz classification and to see at which values I should call an object either a galaxy or a quasar.

In Figure 4.2 I present a histogram of the ANNz class of the test data. The known QSOs are represented by the bold line and the known galaxies are represented by the dotted line and their ANNz class distribution on the x axis. 1299 of the test QSOs are classified correctly if the separation is chosen to be 0.8 between QSOs and galaxies (explained further in Section 4.3.2); however, there are 73 test QSOs that ANNz classifies as galaxies (discarded QSOs). ANNz correctly classi-

111
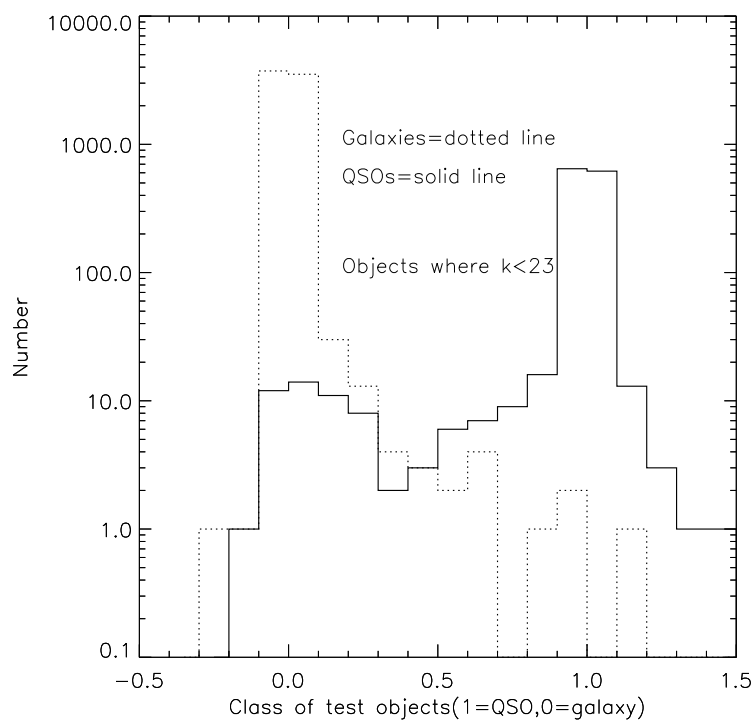
Figure 4.2: The classification of the training data using ANNz. Most of the galaxies (dotted line) are correctly classified, however some of the QSOs (bold line) are inaccurately classified as galaxies and some galaxies are classified as quasars, using a separation value of 0.8. Note the logarithmic y-axis of this histogram.

fies 7310 test galaxies, with only 5 misclassified as QSOs (galaxy contaminants).

The number of galaxy contaminants and discarded QSOs have been investigated further by looking at the ANNz class of the test data as a function of K_s-band apparent magnitude; see the left-hand panels of Figures 4.3, 4.4,

and 4.5.

In Figures 4.3, 4.4 and 4.5 I show the neural network classification of an object being a QSO versus the percentage of galaxy contaminants as well as the percentage of objects that are discarded; see right-hand panels. These figures show how many contaminants I get for each K_s band magnitude range and how many QSOs I discard with a given QSO/galaxy separation choice.

I found that the neural network cannot accurately classify QSOs that are fainter than $K_s = 21$, presumably because there are a limited number of training QSOs beyond $K_s = 21$ (see Figure 4.6). I was unable to investigate this effect further to see if I could go down to $K_s = 21.5$ due to the limited number of training objects found in each K_s band range. Therefore I impose a conservative limit of $K_s < 21$ on the QSO sample selection.

4.3.2 Separation choice

In Table 4.1 I show the test data split into a range of K_s band magnitude bins and have compared the percentage of galaxy contaminants and the percentage of discarded QSOs. This was calculated by finding the ratio between the number of classified quasars/galaxies using ANNz and the number of real quasars/galaxies in the test set for each K_s band. This shows the fraction of galaxies/quasars that are misclassified by ANNz.

From this table and Fig 4.3 it is clear that a magnitude cut at $K_s \sim 21$ provides the largest number of QSOs with the lowest number of galaxy contaminants. Beyond $K_s \sim 21$, the neural network has misclassified a lot of QSOs as galaxies and I will be discarding the majority of the QSO sample. Using Figures 4.3, 4.4,
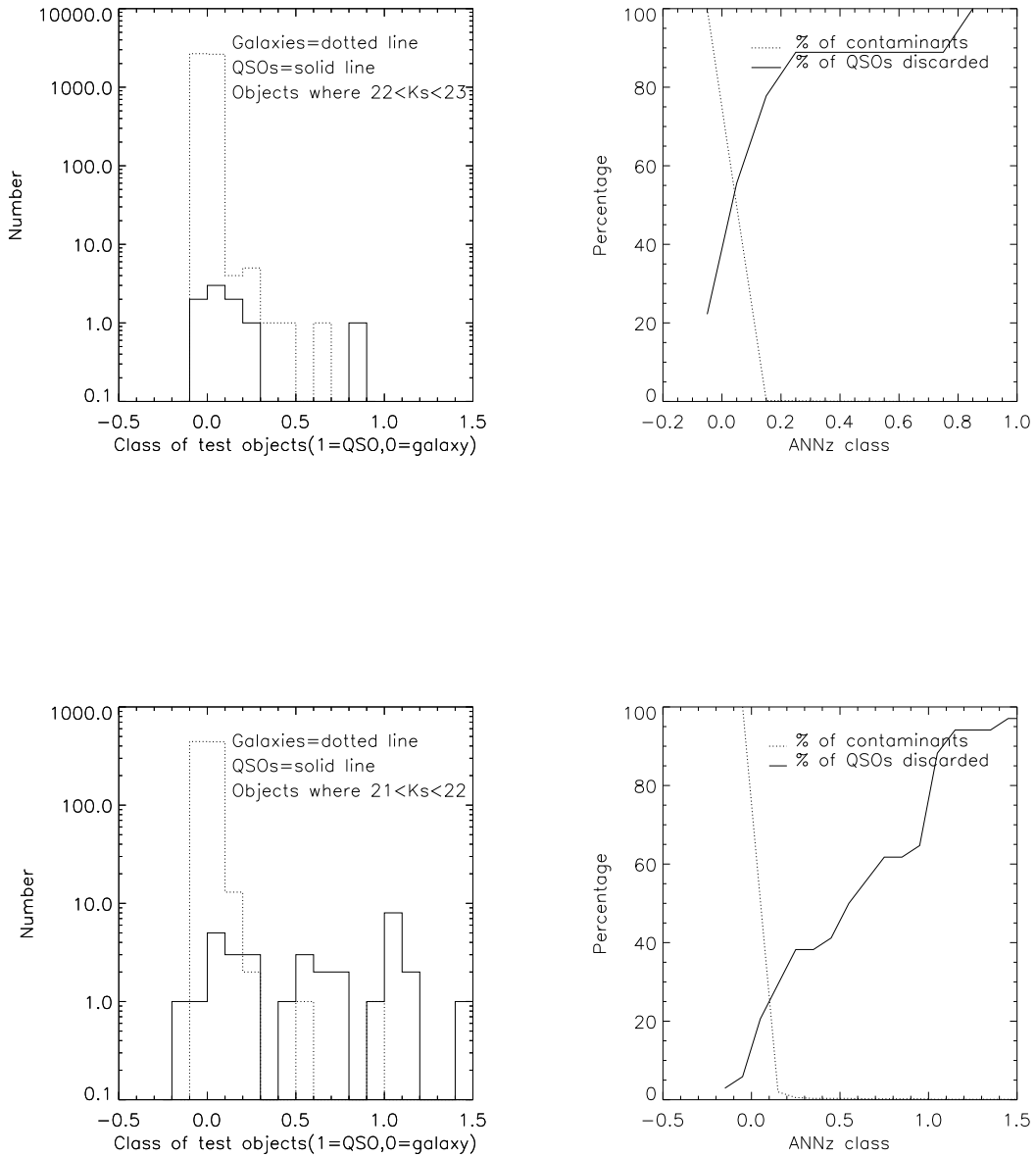
Figure 4.3: Left-hand panels: Classification of the test data using ANNz at $21 < K_s < 23$ magnitudes. The dotted line represents the known galaxies and the solid line represents the known QSOs from the test set. Right-hand panels: Corresponding plot of the neural network classification of an object being a QSO versus the percentage of contaminants (galaxies) as well as the percentage of objects that are discarded.

114
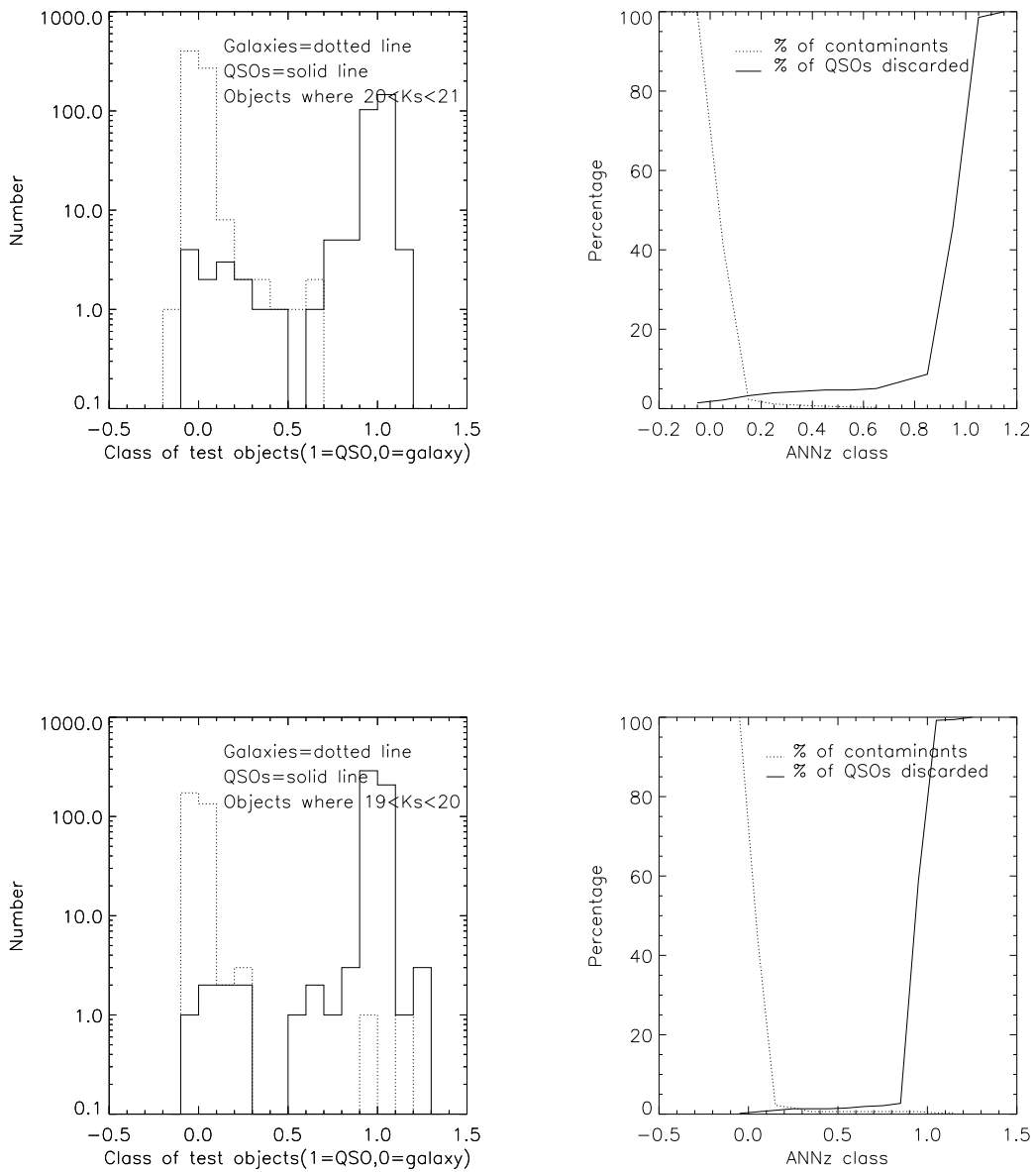
Figure 4.4: Left-hand panels: Classification of the test data using ANNz at $19 < K_s < 21$ magnitudes. The dotted line represents the known galaxies and the solid line represents the known QSOs from the test set. Right-hand panels: Corresponding plot of the neural network classification of an object being a QSO versus the percentage of contaminants (galaxies) as well as the percentage of objects that are discarded.
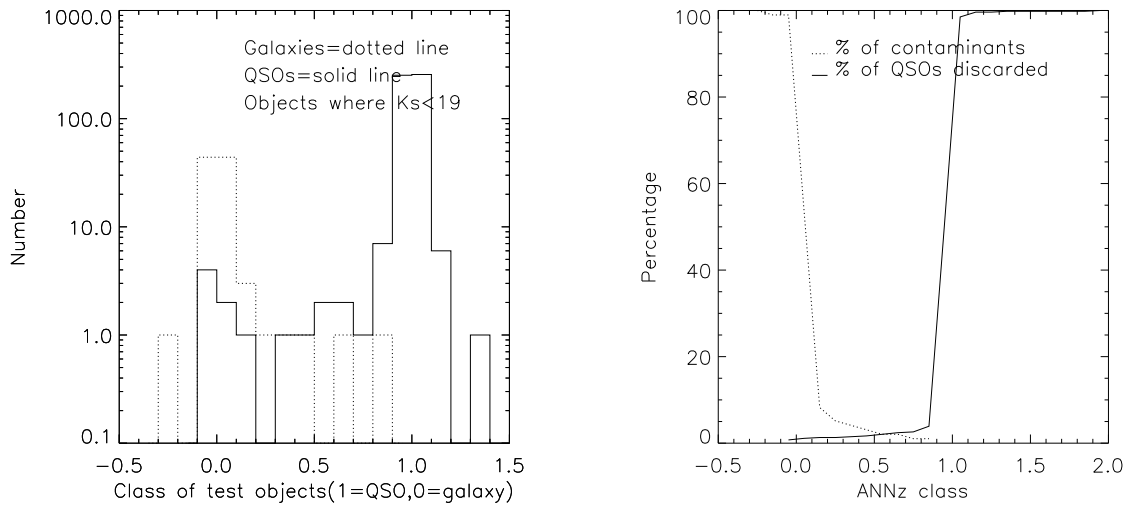
Figure 4.5: Left-hand panels: Classification of the test data using ANNz at $K_s <$ 19 magnitudes. The dotted line represents the known galaxies and the solid line represents the known QSOs from the test set. Right-hand panels: Corresponding plot of the neural network classification of an object being a QSO versus the percentage of contaminants (galaxies) as well as the percentage of objects that are discarded.
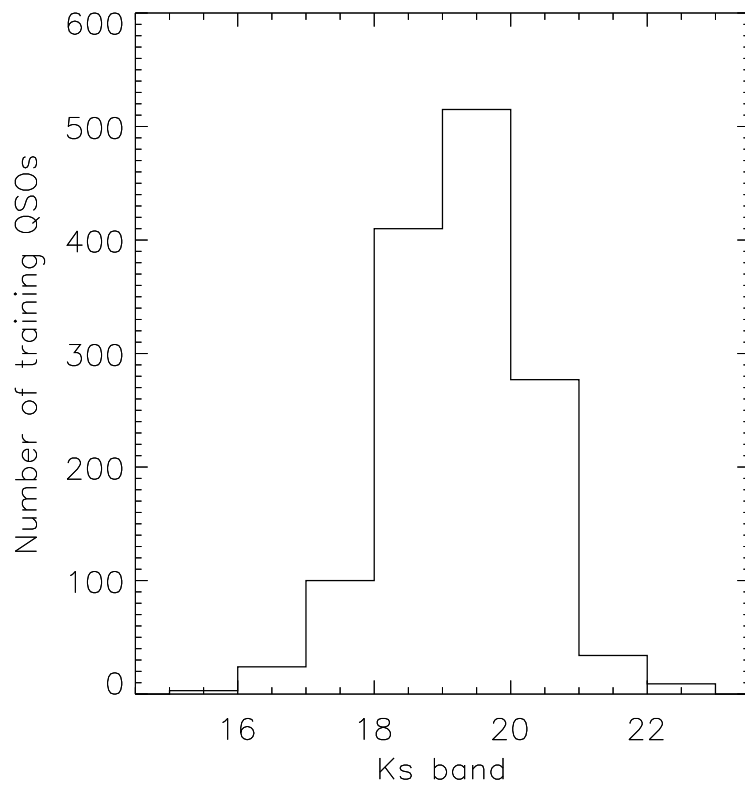
Figure 4.6: The number of training QSOs found in each given K_s band magnitude range.

4.5 and Table 4.1 I have investigated the percentage of misclassified quasars and galaxies for each separation choice. The separation value between galaxies and quasars is chosen to include as many QSOs as possible without including a lot of

Table 4.1: Percentage of discarded QSOs and the percentage of galaxy contaminants, for the test data, using boundaries $0.5 - 1.0$ for each K_s magnitude range. The boundary represents the separation between QSOs and galaxies.

Boundaries	K_s range	Contaminants (%)	Discarded (%)
1.0	$22 < K_s < 23$	0.0	100
1.0	$21 < K_s < 22$	0.11	70.5
1.0	$20 < K_s < 21$	0.0	64.98
1.0	$19 < K_s < 20$	0.31	77.7
1.0	$K_s < 19$	1.0	76.5
0.9	$22 < K_s < 23$	0.0	100
0.9	$21 < K_s < 22$	0.11	61.8
0.9	$20 < K_s < 21$	0.0	9.0
0.9	$19 < K_s < 20$	0.31	2.7
0.9	$K_s < 19$	1.0	4.3
0.8	$22 < K_s < 23$	0.0	88.8
0.8	$21 < K_s < 22$	0.22	61.7
0.8	$20 < K_s < 21$	0.0	6.8
0.8	$19 < K_s < 20$	0.32	2.1
0.8	$K_s < 19$	1.0	2.6
0.7	$22 < K_s < 23$	0.0	88.88
0.7	$21 < K_s < 22$	0.22	55.88
0.7	$20 < K_s < 21$	0.0	5.42
0.7	$19 < K_s < 20$	0.32	1.94
0.7	$K_s < 19$	1.03	2.42
0.6	$22 < K_s < 23$	0.018	88.88
0.6	$21 < K_s < 22$	0.22	50.00
0.6	$20 < K_s < 21$	0.15	4.69
0.6	$19 < K_s < 20$	0.64	1.55
0.6	$K_s < 19$	2.06	2.23
0.5	$22 < K_s < 23$	0.018	88.88
0.5	$21 < K_s < 22$	0.332	44.12
0.5	$20 < K_s < 21$	0.15	4.69
0.5	$19 < K_s < 20$	0.64	1.36
0.5	$K_s < 19$	2.06	1.68

galaxy contaminants. Initially 0.5 might seem like a sensible value, this is halfway between 1 (quasar) and 0 (galaxy). However, this might discard less QSOs but I want to reduce the number of galaxy contaminants in the QSO sample. Based

on Fig 4.3, 4.4 and 4.5 I have chosen to use a separation value of 0.8. This might discard more QSOs (e.g for $K_s < 19 : 2.6$ per cent discarded) compared to a separation value of 0.7 (e.g for $K_s < 19 : 2.42$ per cent discarded) but has fewer galaxy contaminants (e.g for $K_s < 19 : 1.0$ per cent contaminants) compared to 0.7 (e.g for $K_s < 19 : 1.03$ per cent contaminants). A higher value of 0.9 has the same percentage of galaxy contaminants in the $K_s < 19$ bin but increases the percentage of discarded quasars to 4.3 per cent. Therefore, a separation value of 0.8 is a sensible value to choose.

4.3.3 Efficiency

I now determine the efficiency of using ANNz to classify the known QSOs that are within the test set. This is the fraction of known QSOs amongst the total sample of known objects. ANNz has classified 1304 objects in the test data as QSOs (i.e. their corresponding ANNz class is > 0.8) out of 1372 known QSOs. This implies an efficiency of $1304/1372 = 95\%$.

4.3.4 Properties

I have investigated whether the misclassified QSOs/galaxies occupy a particular area in colour space without imposing a magnitude cut at $K_s = 21$. The $(g - i)$ versus $(J - K_s)$ colours of the objects in the test sample are shown in Figure 4.7 and Figure 4.8 for the quasars and galaxies respectively.

In Figure 4.7 I show the test QSOs that are misclassified as galaxies (purple diamonds). The misclassified QSOs do not seem to occupy a particular colour in $(J - K_s)$, however, they do occupy $(g - i) > 0.2$ colours. This is where ANNz

struggles to distinguish between QSOs and galaxies. This is because these QSOs are found in the galaxy regime (see Fig 6a Baldry et al. 2010) and 50 per cent of them have $K_s > 21$, so are too faint for ANNz to classify them correctly.

In Figure 4.8 I show the test galaxies that are misclassified as QSOs (purple diamonds). There are only 5 misclassified galaxies in the test data, so it is difficult to determine whether they occupy a particular region in colour space. However, 4 of them have $(J - K_s) > 0.8$, which is in the QSO regime (see Fig 6a Baldry et al. 2010). This is not a significant problem because there are a lot more misclassified quasars than galaxy contaminants. This is good because I am interested in getting a "clean" sample of quasars rather than a complete sample with more galaxy contaminants.

4.4   The Stellar Removal

To ensure that the ANNz does not classify any stars as QSOs within the VIDEO data I performed colour cuts on the VIDEO data to remove the stars. The ANNz only classifies what are galaxies and QSOs in the VIDEO data and does not classify stars. The easiest way to remove the stars in the data is to use colour cuts which have been used previously (Baldry et al., 2010; Jarvis et al., 2013).

The colour cuts I used to define the star-galaxy separation, taken from Baldry et al. (2010) are found in equation 4.3 and are over-plotted on Figure 4.9, where the dashed line represents a fit to the stellar locus over the range $0.3 < g - i < 2.3$ and constant $J - K$ either side of the fitted range. The dotted-dashed line is $+0.1$ in $J - K$ from this fit which is a slight adjustment of the location of the locus to account for the difference between the K filter (UKIDSS) and the K_s filter
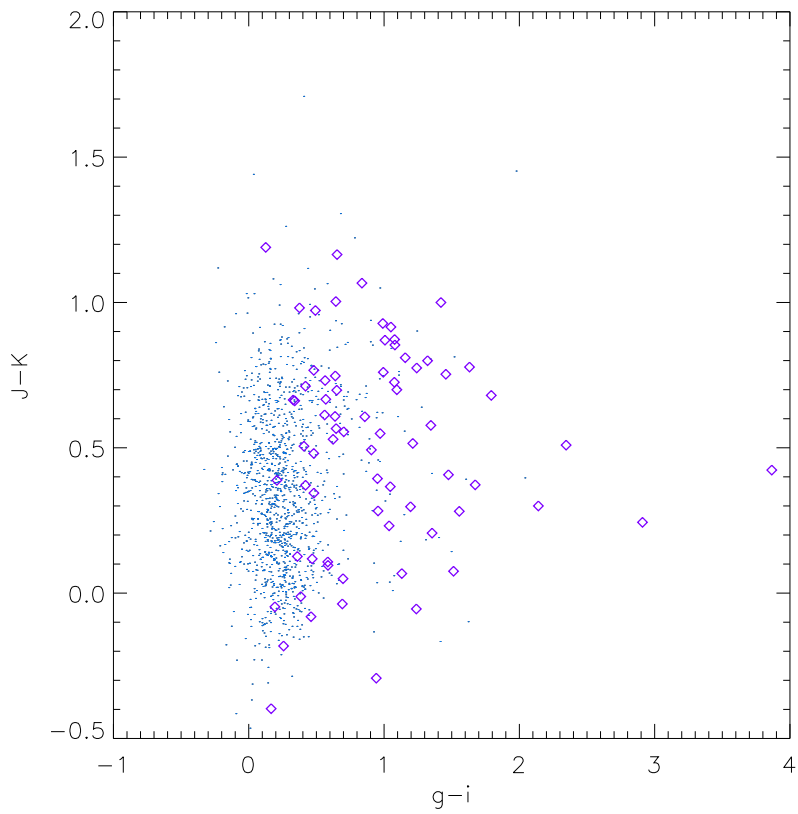
Figure 4.7: The $(g - i)$ versus $(J - K_s)$ colour of the test quasars that have class> 0.8 (blue); overplotted are the test quasars which are misclassified, class< 0.8 (purple).

(VISTA, Jarvis et al. 2013).
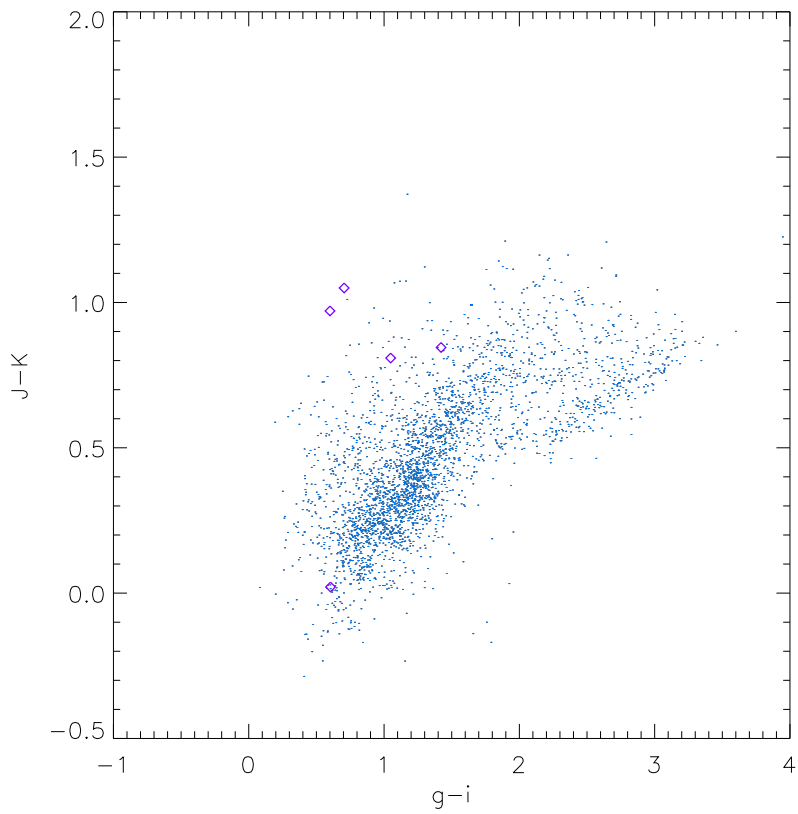
Figure 4.8: The $(g - i)$ versus $(J - K_s)$ colour of the test galaxies that have class< 0.8 (blue); overplotted are the test galaxies which are contaminants to the QSO candidates where class> 0.8 (purple).

$$
f_{\text{locus}}(x) = -0.79 + 0.615x - 0.13x^2 \quad \text{for } 0.3 < x < 2.3, \qquad \begin{matrix} -0.6172 \ x < 0.3, \\ \\ -0.0632 \ x > 2.3. \end{matrix} \tag{4.3}
$$
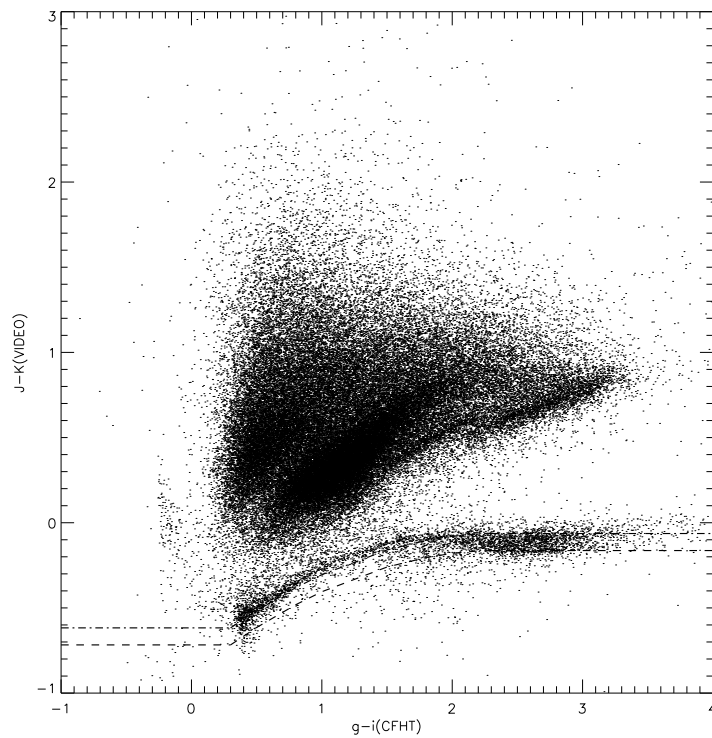
Figure 4.9: The VIDEO data with the stellar region defined between the dashed lines, for sources with $K_s < 23$ in VIDEO. The dotted-dashed line denotes the stellar locus fit from Baldry et al. (2010) offset by 0.1 mag in $(J - K_s)$ colour as described in the text.

I performed a preliminary run of ANNz on the VIDEO data after using the cuts defined by equation 4.3 and found a lot of contaminants from possible main sequence stars and low mass stars due to their close location to the stellar boundary; see Figure 4.10. Therefore, I decided that a stricter cut would be needed to

ensure there is little contamination from stars in the VIDEO data. I decided to cut the VIDEO data at $J - K_s = 0$ to ensure I removed the contamination from low mass stars with $J - K_s < 0$, see Figure 4.10. Using these stricter cuts I may lose possible quasars; however, this is preferable to stellar contamination in the quasar candidate sample for the science I am doing.

4.4.1 The VIDEO QSO Candidates

Figure 4.11 shows the ANNz classification of the VIDEO data using the training set. For completeness, all of the objects where $K_s < 23$ are shown in the first panel of this figure; objects are classified as quasars if class > 0.8 and as galaxies if class < 0.8. The bold line shows all of the objects classified as quasars and the dotted line is all of the objects classified as galaxies using this criterion. The right-hand panel of Figure 4.11 shows the VIDEO classification with objects with $K_s < 21$ as discussed in Section 4.3.1. I find that with my choice of separation criterion there are 274 possible quasars in the VIDEO data for this conservative magnitude limit.

4.4.2 Number of misclassified objects

The number of galaxy contaminants/discarded QSOs can be estimated in the VIDEO data in each K_s bin. This is done by using the fraction of misclassified QSOs/galaxies in the test data (see Table 4.1) and assuming this fraction would be the same for the VIDEO objects. This is just an estimation because the number of test objects is a limiting factor.

To calculate the possible misclassified galaxies in the whole VIDEO sample
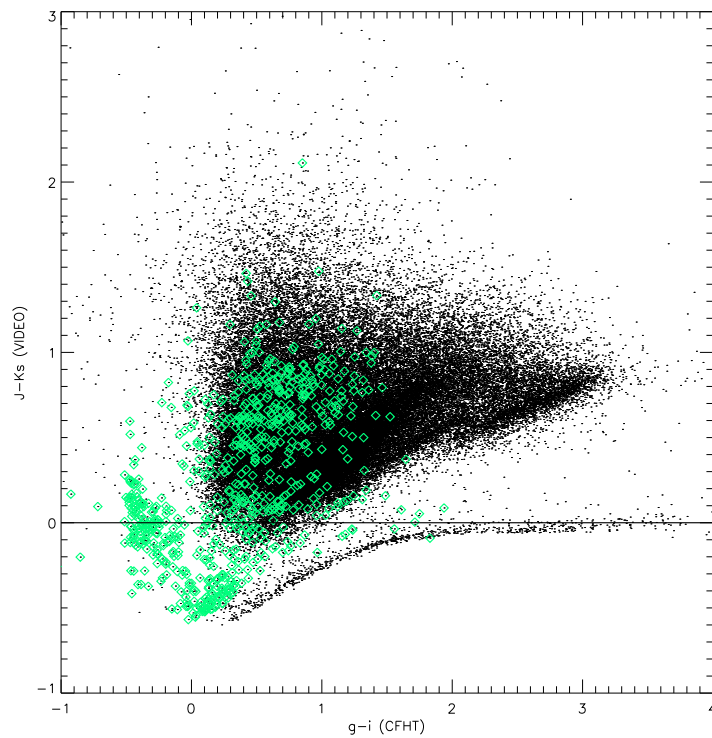
Figure 4.10: The VIDEO data are represented by the black points and the candidate QSOs ($K_s < 21$) are represented by the turquoise diamonds. The bold line represent the location of the strict stellar locus cut at $J - K_s = 0$, where I removed all objects below the bold line. Only VIDEO objects with $K_s < 23$ are shown.

I multiply the fraction of misclassified galaxies for the test data in each K_s bin with the number of VIDEO objects. I find a possible 16 galaxy contaminants all out of 17149 VIDEO objects with $K_s < 21$. To calculate the number of discarded QSOs I use 258 ($274-$ number galaxy contaminants) and multiply by $f_Q/(1-f_Q)$,
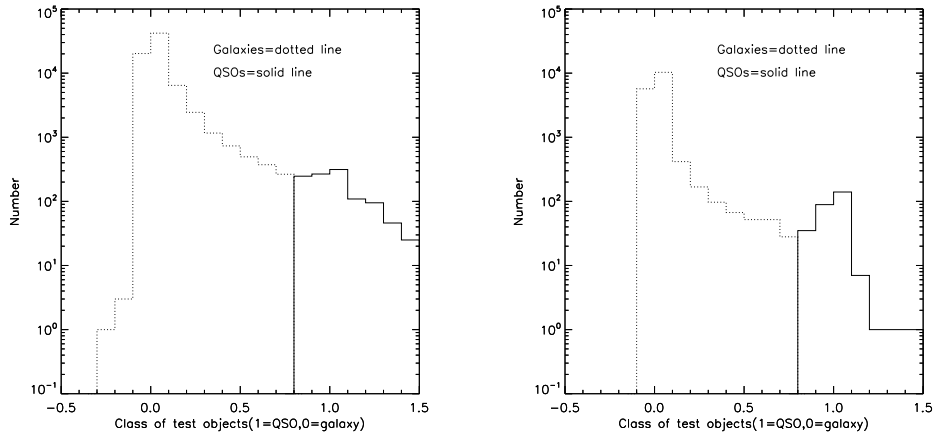
Figure 4.11: Left-hand plot: A histogram of the classification of the VIDEO data ($K_s < 23$) using the complete training data to train the ANNz. Galaxies are represented by the bold line and QSOs are represented by the dotted line. The boundary between them is at an ANNz class of 0.8. Right-hand plot: A histogram of the classification of the VIDEO data ($K_s < 21$) using the complete training data to train the ANNz. There are 274 QSOs with $K_s < 21$.

where $f_Q \sim 0.07$ is the fraction of misclassified QSOs in the test data. This gives 19 misclassified QSOs in the QSO candidate sample. So in my candidate QSOs sample I will have 16 misclassified galaxies and discarded 19 QSOs based on the fraction of misclassified objects in the test set.

These values seem quite large, with 16 possible galaxy contaminants which is approximately 5 per cent of the candidate QSOs sample. However, these values are based on the percentages of galaxy contaminants/discarded QSOs in the test data, thus are preliminary estimates. Spectroscopic follow-up is necessary to accurately determine the classification of QSOs.

4.4.3 Checking the Colours

To check the QSO classification I compared the ANNz-classified QSOs and galaxies in colour space to see if they occupy the correct colour space for their object type.

Figure 4.12 shows the $(g - i)$ vs $(J - K_s)$ colours of the candidate QSOs (magenta and green points) and the SDSS/2SLAQ training QSOs (black crosses). The objects that have an ANNz class > 0.8 are shown as green and blue crosses. I also show the objects that have a stricter ANNz classification of > 0.9 (only blue cross). Most of the objects are in the correct location for QSOs except a few objects at $(g - i) < 0$, which are possibly low mass stars. The candidate QSOs are within the same location, in colour space, as the SDSS/2SLAQ QSOs. This is a check for the ANNz selected candidate QSOs.

Chiu et al. (2007) have shown that it is possible to classify QSOs using the (u-z) vs (Y-K) colours which separate Galactic stars from quasars. They use a colour selection cut which is illustrated in equation 4.4,

$$
\begin{aligned}
(\mathrm{u} - \mathrm{z}) &< 4.5, \\
(\mathrm{Y} - \mathrm{K}) &> 0.6, \\
(\mathrm{Y} - \mathrm{K}) &> 0.35(\mathrm{u} - \mathrm{z}) + 0.425.
\end{aligned} \tag{4.4}
$$

By using this colour selection I can check whether the candidate QSOs are in the correct colour region for QSOs. Figure 4.13 shows $(u_{Vega} - z_{Vega})$ vs $(Y_{Vega} - K_{s,Vega})$ for the candidate QSOs and the VIDEO objects ($K_s < 23.5$).
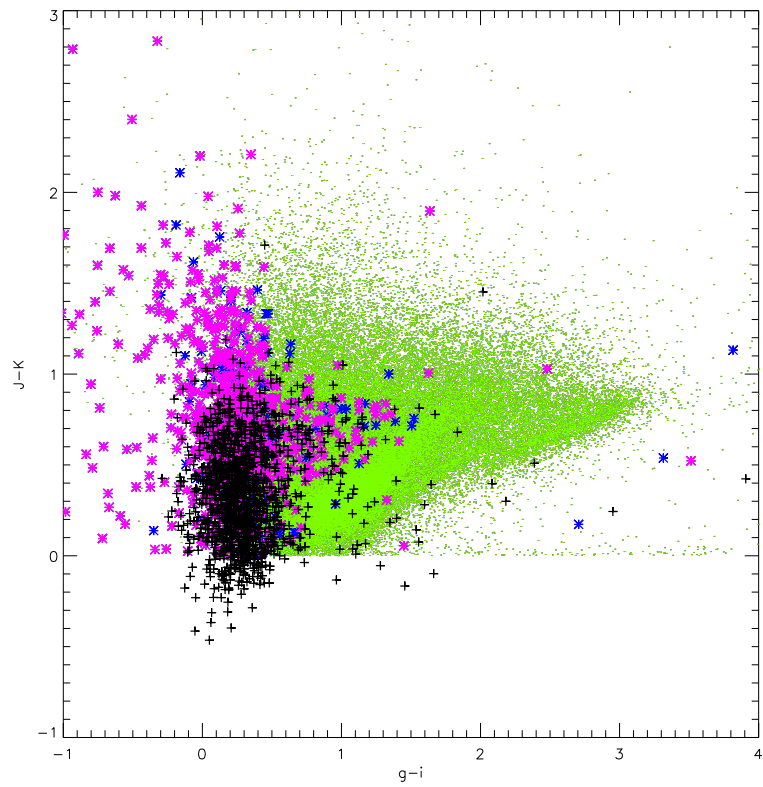
Figure 4.12: $(g-i)$ vs $(J-K_s)$ colours for the sample of VIDEO candidate QSOs when class> 0.8 (magenta asterisk and blue asterisk) and for the QSOs when class> 0.9 (magenta asterisk). The green points are all of the VIDEO objects and the black crosses represent the SDSS/2SLAQ training QSOs.
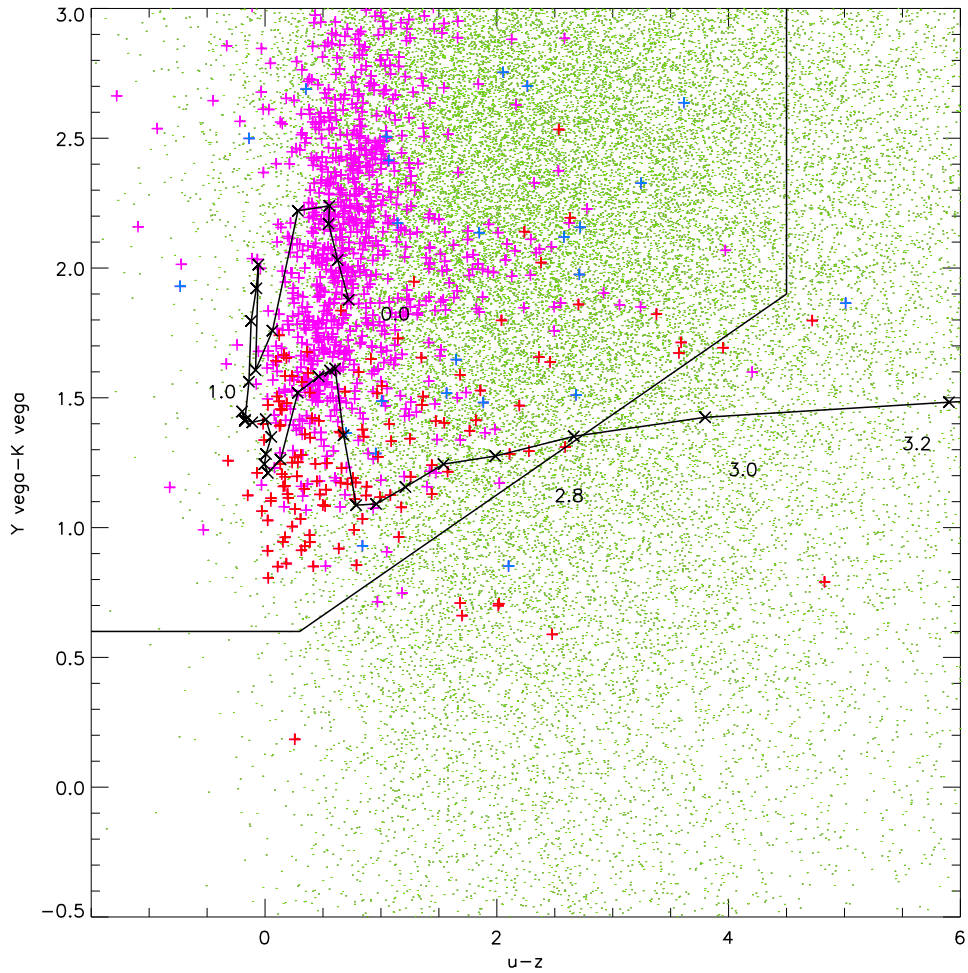
Figure 4.13: $(u-z)$ vs $(Y_{Vega}-K_{s,Vega})$ colours for the sample of VIDEO candidate QSOs where class> 0.8 (magenta cross) and for the QSOs where photo z> 2.8 and class> 0.8 (blue cross). The green points are the VIDEO objects and the red crosses are the objects with $z < 0.5$. The lines represent the divide between QSOs (upper left, magenta cross) and possible contamination from stars (magenta lower right) or high redshift QSOs ($z_{phot} > 2.8$, blue cross lower right). A quasar track, from $z = 0$ to $z > 3$, from Maddox et al. (2012) is over-plotted.
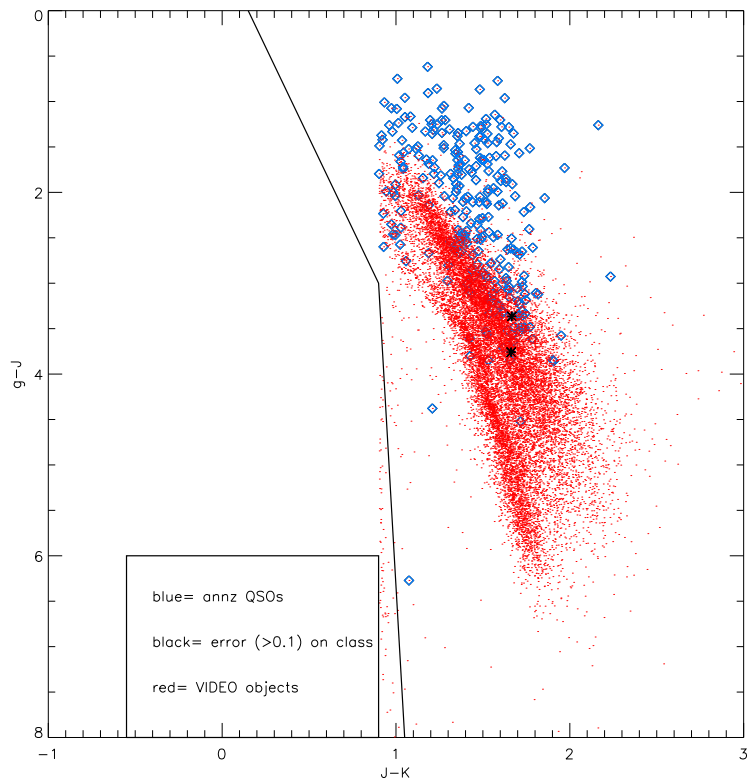
Figure 4.14: $(J_{Vega} - K_{s,Vega})$ versus $(g_{Vega} - J_{Vega})$ colours for the QSO candidates (blue diamonds) and the VIDEO objects $K_s < 21$ (red points). The black asterisks represent the QSOs with the largest uncertainties (> 0.1) in ANNz class. The solid line is the stellar selection boundary from Maddox et al. (2012, 2008).

I converted the wavebands from AB mags to Vega using equation 4.5 to be able to compare the colours of the VIDEO QSOs to those of the QSOs described by Chiu et al. (2007) and to use their QSO selection cuts.

$$u_{\text{Vega}} = u_{\text{AB}} - 0.93,$$
$$g_{\text{Vega}} = g_{\text{AB}} + 0.10,$$
$$z_{\text{Vega}} = z_{\text{AB}} - 0.53,$$
$$Y_{\text{Vega}} = y_{\text{AB}} - 0.937,$$
$$J_{\text{Vega}} = J_{\text{AB}} - 1.384.$$
$$K_{\text{s,Vega}} = k_{\text{AB}} - 1.839. \tag{4.5}$$

There is a clear divide in colour space within Figure 4.13. Chiu et al. (2007) found any objects that lie in the upper-left section of the plot to be possible candidate QSOs and any objects that lie in the lower-right section of the plot possible stellar or galaxy contaminants. Most of the ANNz QSOs lie in the QSO region of Figure 4.13, which shows how successful the ANNz is at classifying candidate QSOs with the adopted boundary at class> 0.8. There are a few objects which lie below the line and these could be stellar contaminants, particularly as 14 of them have $z_{photoz} < 0.5$ (red crosses).

I also consider the candidate QSOs which reside at higher redshifts ($z_{\text{photo}} > 2.8$) because these will move over to the right-hand side of Figure 4.13, i.e. to redder colours compared to their lower-redshift counterparts. I have created a sub-sample of high redshift QSOs, within the classification scheme, which are

represented as the blue crosses. These all have $z_{photo} > 2.8$ and class> 0.8; some of them lie in the stellar contaminant region in Figure 4.13. On Figure 4.13 a typical QSO evolutionary track is shown to check how the QSOs evolve with redshift. Above $z > 2.6$ the QSOs move from the QSO region to the stellar region. Therefore, I would expect that colour cuts will not be as successful at classifying QSOs at higher redshifts.

Figure 4.14 shows a further check on the QSO colours in which I compare the $(J_{Vega} - K_{s,Vega})$ versus $(g_{Vega} - J_{Vega})$ colours of the candidate QSOs with the location of the SDSS QSOs in Fig 2 of Maddox et al. (2012). The location of the candidate QSOs matches well with the location of the SDSS QSOs, with the exception of the QSOs with the largest uncertainties.

Therefore I conclude that artificial neural networks can be successful at classifying a large number of objects in large surveys with only photometric data and no prior spectroscopic redshift information. The neural networks rely heavily on the training data and it is important to have a large enough sample of known quasars and galaxies with spectroscopic redshifts and the same photometric bands as the unknown sample. This is because neural networks learn the relationships between type of objects and their photometric magnitudes and the more objects (QSOs) there are in the training sample the more efficiently/accurately the neural network can classify the unknown data. Obviously there are limitations to the training data: to get a large sample of QSOs in photometric bands that match those of the unknown data can be a challenge. However, the work I have carried out in this chapter shows that neural network classification can be a robust method to find candidate QSOs, which can then be used in follow-up observations to spectroscopically confirm whether they are QSOs and to determine accurate

redshifts.

4.5   Comparison with a Colour Selected QSO Sample

QSOs can be selected using other methods, such as the colour selection criteria outlined in Maddox et al. (2012, 2008). This enables me to compare the ANNz selected QSOs to a colour-selected sample to see if the ANNz QSO selection method selects the same objects as the colour selected QSOs. The colour selected sample was created by S. White (private communication) and uses a stellar boundary described by Maddox et al. (2008)

$$\mathrm{g - J} = 4(\mathrm{J - K}) - 0.6 \text{ for } \mathrm{J - K} \leq 0.9, \mathrm{g - J} \leq 3,$$
$$\mathrm{g - J} = 33.33(\mathrm{J - K}) - 27 \text{ for } \mathrm{J - K} > 0.9, \mathrm{g - J} > 3. \tag{4.6}$$

The colour method is capable of going down to magnitude depths of $K_s < 23$, whereas the neural network method that I use is limited at $K_s < 21$, due to limited number of faint training objects. However, colour selection methods can only be very conservative when selecting QSOs, to ensure they have limited contamination from galaxies.

The colour selection method selected 88 QSOs from the VIDEO data and the neural network method selected 274. I cross-matched the QSOs selected by both methods within 1 arcsecond of their coordinates and found that 44 of the neural network selected QSOs matched to the colour selected QSOs. Figure 4.15
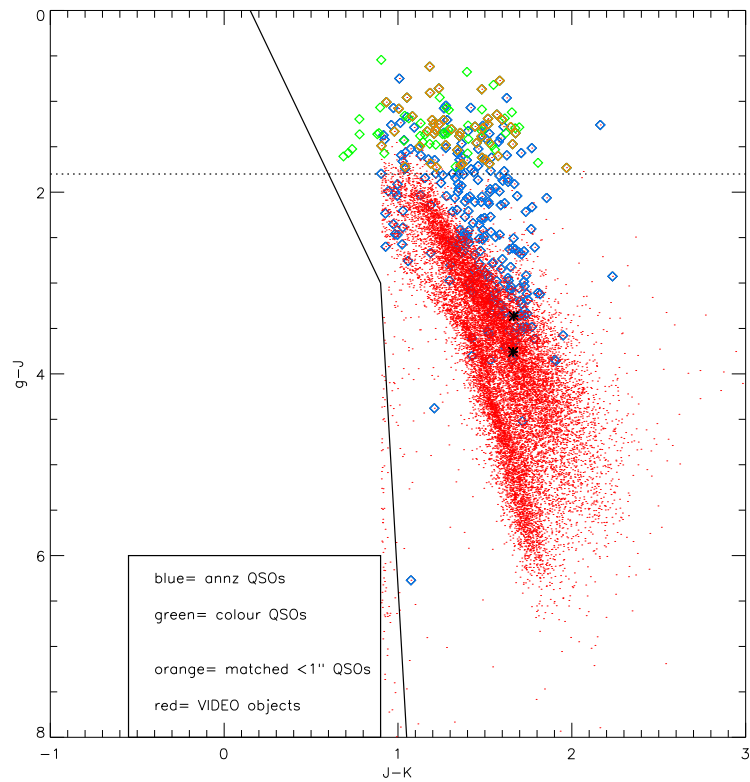
Figure 4.15: A colour-colour plot of $(J-K_s)$ versus $(g-J)$ in VEGA magnitudes. The neural network selected QSOS are represented by blue diamonds, the colour selected QSOs by green diamonds, the cross matched QSOs by orange diamonds, the VIDEO objects $(K_s < 21)$ by red points and the possible outliers from the neural network selection method by black asterisks. 44 QSOs which were selected with ANNz cross-match with the colour selected QSOs. The solid line is the stellar selection boundary from Maddox et al. (2012, 2008) and the dashed line represents the $g - J$ cutoff used for the colour selected QSOs.
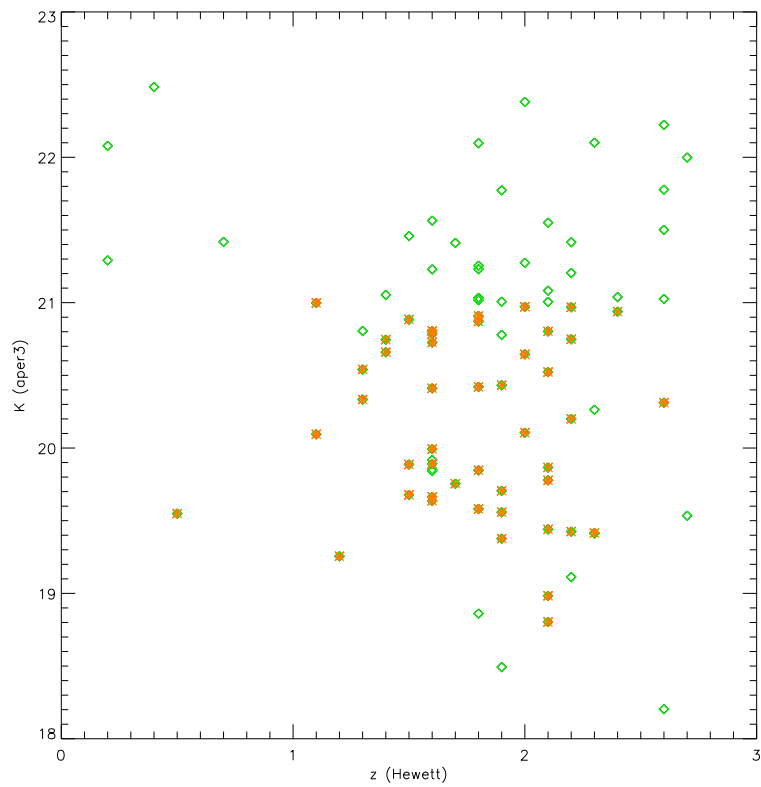
Figure 4.16: The K_s magnitude, from aperture 3, versus the redshift from Hewett for the colour selected QSOs (green diamonds) and the 44 ANNz QSOs matched to the colour selected QSOs (orange asterisks).

shows the (J-K) versus (g-J) colours, in Vega magnitudes, where they select QSOs that are on the right-hand side of the stellar boundary (solid line) and use a conservative limit of $g - J = 1.8$ (dashed line), where the QSOs are above this line. The conservative limit ensures that all of the objects in the colour sample are QSOs.

This shows the limitations of the colour selection method: it can only select objects at the very edge of their colour boundary, due to the galaxy region right below. The neural network method can assign a classification value to each object to determine whether it is a QSO or a galaxy and therefore it can select QSOs throughout the colour plot. The only limitation the neural network method is that it cannot select QSOs in the stellar region, as I removed all objects within this region, or magnitudes beyond $K_s = 21$.

To show how the different selection methods select different QSOs I have plotted the 44 matched QSOs in Figure 4.16 which are represented by the orange asterisks, while the green diamonds represent the colour selected QSOs. This shows that no ANNz selected QSOs match the colour selected QSOs beyond $K_s = 21$ and some QSOs are not matched below $K_s = 21$; this is because the colour selection method has selected some QSOs within the stellar region of the colour plot. This plot also shows that ANNz is capable of detecting ~ 80 per cent of the colour selected QSOs at $K_s = 21$.

There are limitations to both selection methods but I conclude that neural networks can classify a larger sample of QSOs when compared to the colour selection methods.

4.6   Conclusion

I have used a machine-learning algorithm based on artificial neural networks to classify the objects in the VIDEO data as either galaxies or quasars. The neural network is trained on a total of 9387 objects, 1392 of them being spectroscopically determined QSOs and all with spectroscopic redshifts with data in optical and near-infrared bands. I have used ANNz to classify 1304 QSOs from the known 1372 QSOs from the training data, this gives an efficiency of 95% at using ANNz to classify the training QSOs. The main conclusions are as follows.

1. The optimum separation value between galaxies and QSOs was found to be an ANNz class of 0.8, where objects with ANNz class > 0.8 are candidate QSOs and those with class < 0.8 are galaxies. If I chose a lower boundary I would get a more complete QSO sample but have more contaminants from galaxies and if I chose a higher sample I would get a more reliable sample but would be very incomplete. Using this boundary I have been able to identify 16875 possible galaxies and 274 possible quasars within the VIDEO data ($K_s < 21$).

2. The ANNz QSO classification method was limited to $K_s < 21$ because above this the number of galaxy contaminants and discarded QSOs increased. This was because there were fewer QSOs in the training sample with $K_s > 21$.

3. The estimated number of galaxy contaminants in the VIDEO data is 16 and the estimated number of discarded QSOs is 19, all out of 17149 VIDEO objects. These values are based on the percentages of galaxy contami-

nants/discarded QSOs in the test data, thus are preliminary estimates. Spectroscopic follow-up is necessary to accurately determine the classification of QSOs.

4. I have checked that the candidate quasars lie in the correct colour space for QSOs by using a $(u - z)$ versus $(Y - K_s)$ colour space with a stellar-quasar boundary from Chiu et al. (2007). The majority of the candidate QSOs are found within the quasar boundary; only a few are found in the stellar region, which could be because some of them are high-redshift quasars or stellar contaminants.

5. The candidate QSOs were also compared to the spectroscopically confirmed SDSS/2SLAQ QSOs in the training sample using $(g - i)$ versus $(J - K_s)$ colours (Baldry et al., 2010). The majority of the candidate QSOs were in the same colour space as the training sample.

6. I have compared the $(J_{Vega} - K_{s,Vega})$ versus $(g_{Vega} - J_{Vega})$ colours of the candidate QSOs with the location of the SDSS QSOs in Fig 2 of Maddox et al. (2012). The location of the candidate QSOs match well with the location of the SDSS QSOs, with the exception of the QSOs with the largest uncertainties.

7. The 274 neural network candidate QSOs were compared to 88 colour selected QSOs in the VIDEO data. There were 44 QSOs in common between the two samples. The limitations of the neural network selection is the limit on the depth $K_s < 21$ whereas the colour selected QSOs could be selected down to $K_s < 23$. However, the neural network can select beyond the con-

servative colour selection boundary and thus can classify a larger number of QSOs.

8. The colour sample is limited to a strict boundary of $(J - K_s) < 1.8$ but with future spectroscopic confirmation of the QSOs I could define a more complete and reliable boundary in colour space than previous colour cuts. This would increase the number of detected QSOs using the colour-selection technique.

Chapter 5

The Environments of Candidate Quasars in the VIDEO Survey

5.1 Introduction

Searching for high-redshift clusters in blind surveys is observationally expensive and time inefficient; therefore numerous alternative methods have been used. Previous methods of detecting galaxy clusters have made use of the red sequence of galaxies, which are non-starforming passive galaxies that preferentially populate denser regions. These have been used to detect clusters of galaxies out to high redshifts, $z \sim 1.5$ (Bower et al. 1992; Mei et al. 2006; Lidman et al. 2008; Kurk et al. 2009).

Another method of finding galaxy clusters is to detect the extended X-ray emission from the intracluster medium, (Stanford et al. 2005; Stanford et al. 2006; Rosati et al. 2004; Rosati et al. 2009). For example, a Spitzer selected galaxy cluster at $z \sim 1.62$ has been found using concentrations of red galaxies

and detections in X-rays using data from XMM (Tanaka et al. 2010; Papovich et al. 2010). The cluster was detected in the XMM-LSS field of the Spitzer Wide-Area Infrared Extragalactic survey (SWIRE; Lonsdale et al. 2003b). This cluster has 15 confirmed cluster members, is dominated by a population of red galaxies with $(z - J) > 1.7$ mag and has a weak detection of thermal X-ray emission, which is expected for galaxy clusters.

However, when trying to detect high redshift clusters beyond $z \sim 1.5$ a very efficient method is to use bright AGN, such as QSOs as "signposts" to these denser environments. Using near-infrared bands rather than optical makes detecting objects to high redshifts easier. There is also significantly less dust extinction in the near-infrared which makes the prediction and interpretation of galaxy colours, counts and K-corrections easier. In addition, using the near-infrared rather than the optical bands makes it possible to detect the obscured AGN population.

Cluster searches in the near-infrared have been made possible by the UKIRT Infrared Deep Sky Survey (UKIDSS, Lawrence et al. 2007) and the Ultra Deep UKIDSS Survey, which is part of UKIDSS; it has data in the J, H and K bands, reaching depths of $J = 24.9, H = 24.2$ and $K = 24.6$ (AB Mags). 13 clusters between $0.6 < z < 1.4$ have been detected in the UKIDSS Ultra Deep Survey using a cluster-detection algorithm (van Breukelen et al. 2006; van Breukelen et al. 2009). However, to obtain a large sample of clusters out to high redshifts ($z > 1$) is difficult.

In this chapter I investigate the possibility of using AGN as "signposts" to search for high redshift clusters in the VIDEO data. This enables me to investigate whether AGN trace the densest regions and, in particular, the level of star formation in these denser environments, to see whether star formation

is suppressed in high redshift clusters (compared to the picture in the low red-shift Universe, where the highest density regions are dominated by early-type red galaxies rather than star-forming galaxies: Dressler 1980; Tanaka et al. 2005; Postman et al. 2005; Balogh et al. 2007; Poggianti et al. 2009).

In this project I use the near-infrared bands (Z, Y, J, H and K_s) from the VIDEO survey (Jarvis et al., 2013) and optical photometry (u, g, r, i and z) from CFHTLS (Ilbert et al., 2006) to detect galaxy overdensities to $z \sim 3$. I use a sample of 274 QSO candidates ($0.5 < z < 3$), that I have selected using an artificial neural network (Chapter 4). A full description of VISTA and the VIDEO data can be found in Chapter 2.

In Section 5.2 I present the candidate QSO sample and their K-corrections, photometric redshifts, spectroscopic redshifts and completeness values. In Section 5.3 I discuss the density analysis used. In Section 5.4 I show the results for the stacked candidate QSO environments. In Section 5.5 I present the density analysis of the environments for the colour selected candidate QSOs. In Section 5.6 I explain the cross match to the radio data and in Section 5.7 I present the density results separated by galaxy type within the environments of the candidate QSOs. I then discuss the comparison between the candidate QSO environments and galaxy environments in Section 5.8. Finally, I present a discussion in Section 5.9 and a summary in Section 5.10.

5.2 The VIDEO QSO Sample

The construction of the candidate QSO sample was described in Chapter 4. In this section I discuss the further work I did on it to prepare it for the density

analysis.

5.2.1   K-corrections

To estimate the rest frame luminosities for the candidate QSOs, their magnitudes need to be corrected to a common rest-frame wavelength, called the K-correction.

I have determined the K-corrections for the candidate QSOs by assuming that their spectra are described by a simple power law, which is conveniently parameterised through the spectral index α (Richstone & Schmidt 1980). This means that

$$\mathrm{Kcorr} = -2.5(\alpha + 1)\log_{10}(1 + z) \qquad (5.1)$$

where $\alpha = -0.5$ (Richards et al., 2006) and z is the candidate QSOs photometric redshift.

I calculated the absolute magnitude of the candidate QSOs by using the distance modulus

$$\mathrm{M} - \mathrm{m} = 5 - 5\log D_L(z) + \mathrm{K}(z) \qquad (5.2)$$

where $D_L(z)$ is the luminosity distance and $\mathrm{K}(z)$ is the K correction.

The candidate QSOs are detected out to $z \sim 3$ and span 7 magnitudes in i-band absolute magnitude over the photometric redshift range $0.5 < z < 3$. Figure 5.1 shows the photometric redshifts versus absolute i-band magnitude of the candidate QSOs (purple asterisks) selected by ANNz using the VIDEO data. For a comparison with the work of Chapter 3, I have also overplotted the SDSS QSOs (blue points) and the Spitzer QSOs (orange dots); these samples
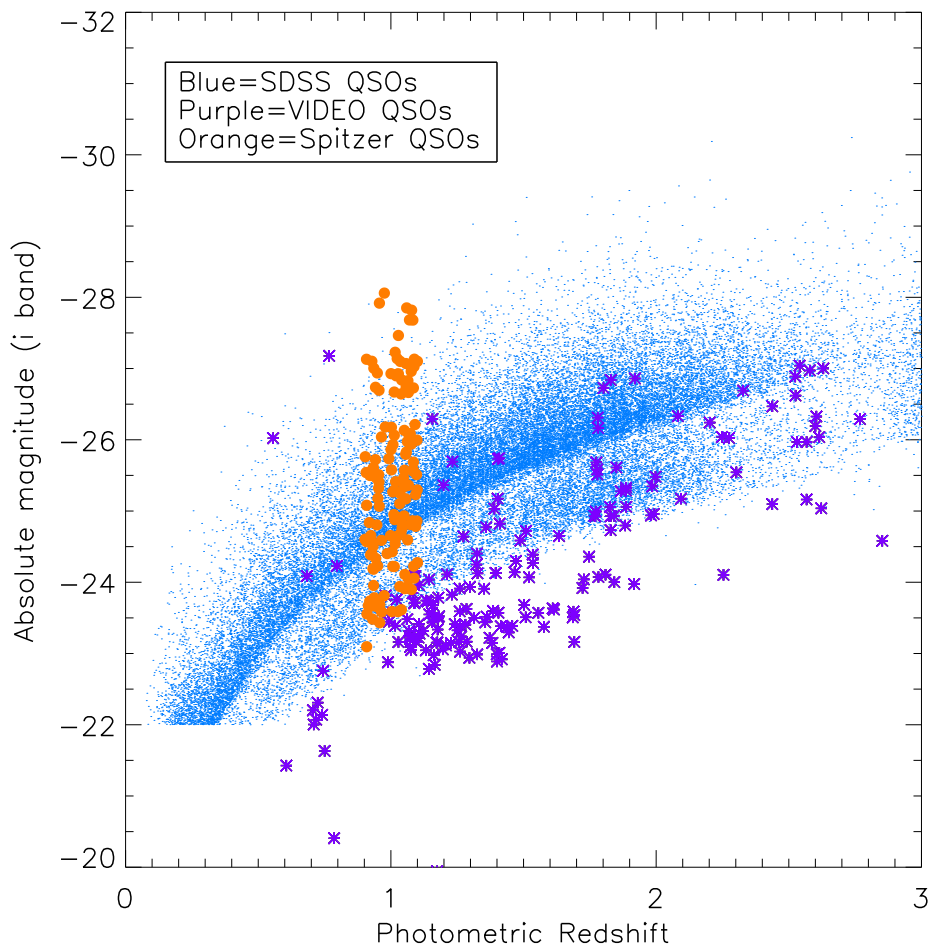
Figure 5.1: Photometric redshifts of the VIDEO QSO candidates (purple asterisks) versus absolute i-band magnitude. SDSS QSOs (Schneider et al., 2005) are overplotted as blue dots and the Spitzer QSOs, which I use in Chapter 3, are overplotted as filled orange circles.

are described in Chapter 3 and both have spectroscopic redshifts. The VIDEO candidate QSOs span the same photometric redshift range as the SDSS QSOs but they are at fainter magnitudes than the SDSS/Spitzer QSOs. This is because the VIDEO survey reaches depths of $K_s < 23.8$ with candidate QSOs identified down to $K_s < 21$, whereas SDSS (Schneider et al., 2005) reaches depths of $i < 19.1$ for QSOs with redshifts $z < 3$.

5.2.2   Photometric redshifts

The photometric redshifts for the VIDEO candidate QSOs/galaxies were determined using the photometric redshift code Le Phare (Ilbert et al., 2006), which is publicly available. They were estimated using the optimised galaxy and quasar templates which are produced by Arnouts et al. (2007). Further details of the photometric redshift estimates can be found in Jarvis et al. (2013).

To investigate the accuracy of the photometric redshifts in the VIDEO data I have cross-matched the VVDS training data (QSOs and galaxies) with the VIDEO data, within < 1 arc seconds, to compare the spectroscopic redshifts to the photometric redshifts; Figure 5.2 shows the results for training galaxies and QSOs. I have only used the galaxies and QSOs with the highest confidence levels in their redshifts from the VVDS data. These have quality flags 4 for galaxies and 14 for QSOs.

I show $(z_{spec} - z_{photo})/(1 + z_{spec})$ for the VVDS data in Figure 5.2. This shows how much the photometric redshifts differ from the spectroscopic redshifts. Jarvis et al. (2013) define photometric-redshift outliers as objects that have $|(z_{spec} - z_{photo})/(1 + z_{spec})| > 0.15$ and I find that only 3.5 per cent of the galaxies in

VVDS, and 36 per cent of the QSOs, are outliers by this definition. The large fraction of QSO outliers is a cause for concern, but it can be seen from the plots that many of the outliers have $z_{photo} < 0.5$. To reduce the number of incorrect photometric redshifts I have restricted my candidate QSO sample to $0.5 < z < 3$; this leaves 187 candidate QSOs.

The ANNz code also produces photometric redshifts for the candidate QSOs. I have followed the above technique to compare the ANNz photometric redshifts for the VVDS training data with the spectroscopic redshifts; see Figure 5.3. Using $|(z_{spec}-z_{photo})/(1+z_{spec})| > 0.15$ to define the outliers I find that 11 per cent of the VVDS galaxies, and 56 per cent of the VVDS QSOs, are outliers; see Figure 5.3. Given these values I elect to use the photometric redshifts determined using Le Phare.

5.2.3   Completeness

For the VIDEO candidate QSOs I need to estimate how complete the sample is to the limiting magnitude. Jarvis et al. (2013) give the completeness of the VIDEO sample at certain magnitudes in each waveband. I can classify the candidate QSOs in the VIDEO data accurately down to $K_s = 21$; beyond this I will get a higher contamination from galaxies in the candidate QSO sample, as discussed in Chapter 4. For the VIDEO-XMM3 field the $K_s = 20.75 - 21.25$ depth ranges from 0.986 to 0.976 complete; at brighter magnitudes the data are even more complete. The galaxies in the VIDEO data are detected down to $K_s = 23.8$ and are found by Jarvis et al. (2013) to be 0.935 complete. Due to the high completeness values I am confident that any incompleteness will not significantly affect the analysis
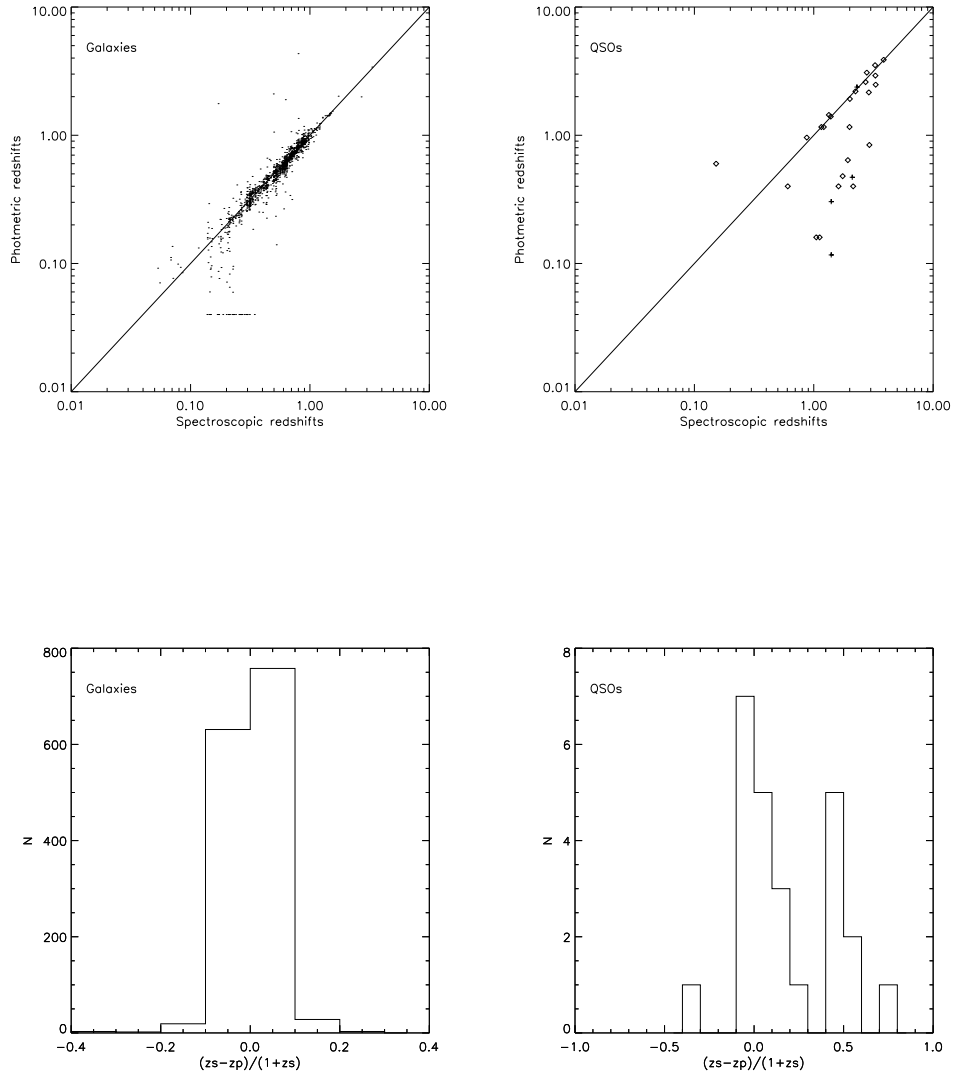
Figure 5.2: Left-hand panel: The spectroscopic redshifts versus photometric red-shifts for the VVDS training galaxies (top) and $\Delta z/(1+z)$ for the template photometric redshifts (bottom). Right-hand panel: The spectroscopic redshifts versus photometric redshifts for the VVDS training QSOs (asterisks) and the VIDEO candidate QSOs with spectroscopic redshifts (crosses) from Southern African Large Telescope (SALT, White et al. (prep)) (top) and $\Delta z/(1+z)$ for the template photometric redshifts (bottom).
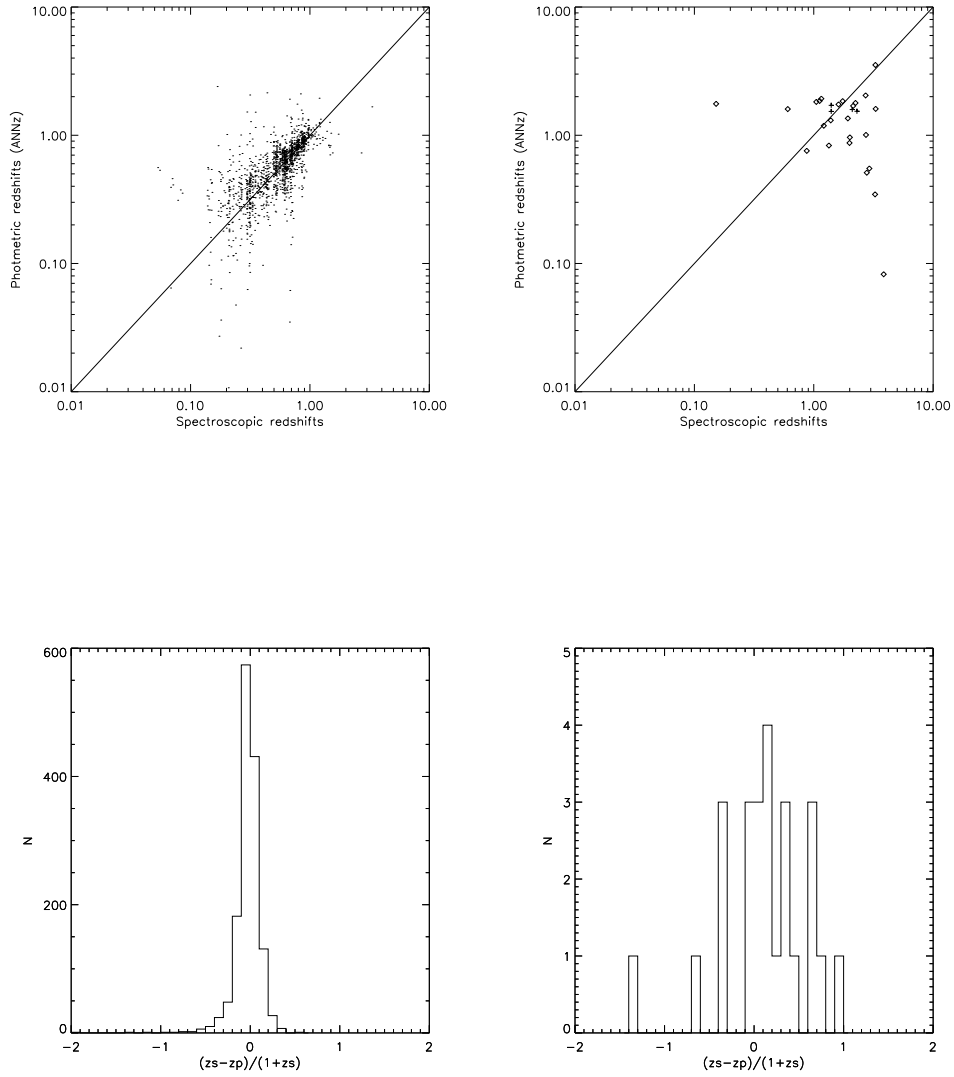
Figure 5.3: Left-hand panel: The spectroscopic redshifts versus ANNz photometric redshifts for the VVDS training galaxies (top) and $\Delta z/(1+z)$ for the template photometric redshifts (bottom). Right-hand panel: The spectroscopic redshifts versus ANNz photometric redshifts for the VVDS training QSOs (asterisks) and the VIDEO candidate QSOs with spectroscopic redshifts (crosses) from Southern African Large Telescope (SALT, White et al. (prep)) (top) and $\Delta z/(1+z)$ for the template photometric redshifts (bottom).

and therefore I can neglect any completeness corrections.

5.3   Density Analysis

5.3.1   Analysis

To study the candidate QSO environments I count the number of VIDEO sources (galaxies) detected in 9 annuli around the candidate QSOs. The annuli are kept to a fixed area to ensure the Poisson noise is similar in each bin. For the radial distances used see Table 5.1. I excluded any objects within 1 arcsec of the candidate QSOs position, which ensured that I did not include the candidate QSOs in the calculation of source density, since including them would give rise to bias in the first bin. I included any objects that have redshifts satisfying

$$\mathrm{photoz_{all}} = \mathrm{photoz_{qso}} \pm (0.3 \times (\mathrm{photoz_{qso}} + 1)) \tag{5.3}$$

where $\mathrm{photoz_{all}}$ is the photometric redshifts of all the objects in the VIDEO catalogue and $\mathrm{photoz_{qso}}$ is the photometric redshift of the candidate QSO. The scaling factor of 0.3 was chosen to get small increments of redshift that took into account the higher uncertainty in the photometric redshifts of the candidate QSOs, especially at high redshifts. From Fig 5.2 it is clear that the vast majority of the galaxy population have photometric redshifts that do not deviate strongly from their spectroscopic redshifts, $|(z_{spec} - z_{photo})/(1 + z_{spec})| < 0.1$; however, the photometric redshifts for the candidate QSOs are more uncertain. For the redshift range of $0.5 < z < 3$, 81 per cent of the candidate QSOs have $|(z_{spec} - z_{photo})/(1 + z_{spec})| < 0.3$. Therefore, taking into account the larger uncertainties

on the candidate QSOs' photometric redshifts, I have chosen to use a scaling factor of 0.3 to determine the redshift range. This ensures that I include most of the galaxies that are associated with the candidate QSOs, creating a complete sample.

5.3.2   Background level

To see if there is an overdensity around the candidate QSOs the expected number of galaxies (the background level) needs to be calculated.

A method of determining the background level is to find the average global background, which is the number of objects detected within a large area of the VIDEO field. This was done for photometric redshift slices, based on each candidate QSO's photometric redshift and counting all the galaxies with photometric redshifts within the range defined by equation 5.3 of the candidate QSO's photometric redshift. I counted the number of sources within a radius of 1.0 Mpc and 3.0 Mpc of 100 randomly placed coordinates for each of the candidate QSO's photometric redshifts within the VIDEO-XMM3 field.

The average source density was then found and the corresponding sample variance error and Poisson error, which were added in quadrature, were calculated. This was done by calculating the standard deviation on the average source density for 100 background values and the Poisson error on each value. The sample variance errors were calculated by

$$\mathrm{CV_{errors}} = \sqrt{\sigma^2 - \sigma_\mathrm{P}{}^2} \qquad (5.4)$$

where σ is the standard deviation of the distribution of background source

densities and σ_P is the Poisson uncertainty. This enabled a calculation of the background level for each candidate QSO with corresponding sample variance and Poisson errors. See Figure 5.4 for the distribution of Poisson and cosmic variance uncertainties for the background values. This shows that the Poisson uncertainties are the dominant source of uncertainty.
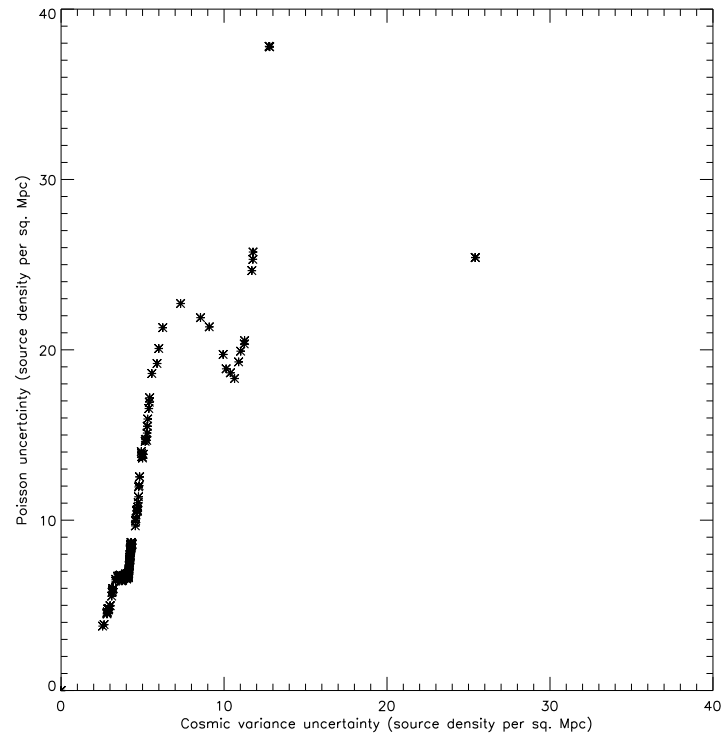
Figure 5.4: The Poisson and cosmic variance uncertainties on each of the background values.

5.3.3   Radial distance

Initially, I chose an outer radius of 3 Mpc for the annuli. This was because I wanted to have a large enough area to include all of the overdensity in a plausible cluster and also enough area to see where the overdensity falls to zero, i.e. the background level. This acts as a check to the results to see where the most overdense regions are, and allows me to investigate whether I can reduce the radial distance to include a larger candidate QSO sample. Falder et al. (2010) found that source overdensities that were associated with candidate QSOs were within a 1 Mpc radius of the candidate QSOs, therefore 3 Mpc should be a large enough radius to include all of the source overdensities and to see where they fall off to the background level.

In Figure 5.5 it can be seen that many candidate QSOs are detected near the edge of the field. This will cause problems for the environmental analysis because there will not be enough area around these candidate QSOs to investigate their source overdensities out to 3 Mpc. Therefore, these candidate QSOs need to be removed from the environmental analysis. This was done by excluding candidate QSOs which were within 3 Mpc of the edge of the field at the photometric redshift of the candidate QSOs.

Using a region of radius 3 Mpc I found the largest source overdensities were within 1 Mpc of the candidate QSOs and then they decreased to the background level at 3 Mpc. However, the 3 Mpc radial analysis only included 58 per cent of the 187 candidate QSOs between $0.5 < z < 3$. Therefore, I extended the analysis to include more candidate QSOs using an extraction region of radius 1 Mpc. This allowed me to include 159 candidate QSOs out of the 187 that are

between $0.5 < z < 3$, which is 85 per cent of the candidate QSO sample.
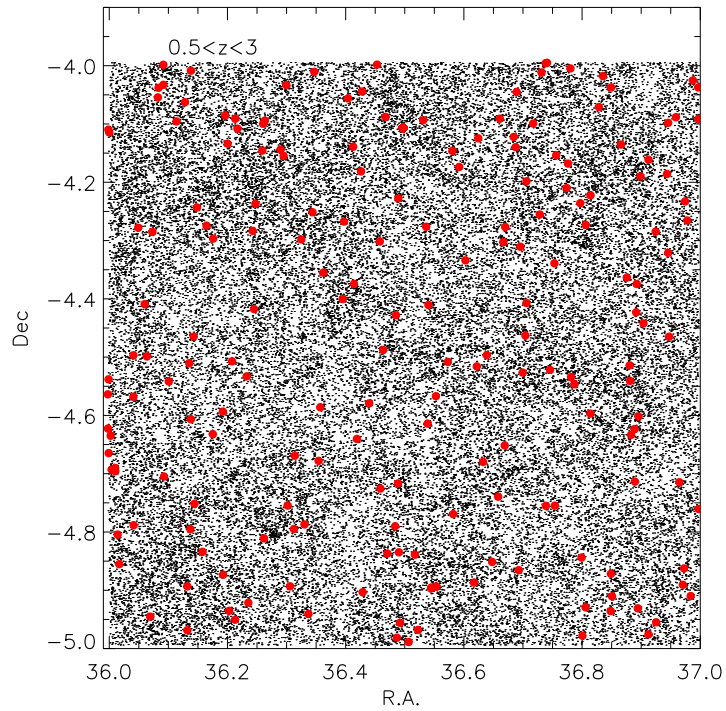
Figure 5.5: Plot of the R.A. and Dec of the candidate QSOs (red dots) and the VIDEO data (black points) in the VIDEO-XMM3 field.

5.3.4 Checking Background

I have checked the background values by calculating the density around 109 random coordinates in the VIDEO data, avoiding the edge of the field, but with the

Table 5.1: Table of the stacked source over-densities (Mpc^{-2}) found in the 3 Mpc region of the random coordinates and the corresponding uncertainty and significance. The inner and outer radius (Mpc) of each annulus is given in the table.

Annulus	inner radius (Mpc)	outer radius (Mpc)	Over-density (Mpc^{-2})	$\pm$ error	σ
A1	0	1.0	0.42	1.032	0.40
A2	1.0	1.4	0.25	1.032	0.25
A3	1.4	1.7	-0.51	1.031	-0.50
A4	1.7	2.0	-0.39	1.031	-0.38
A5	2.0	2.2	-0.17	1.032	-0.16
A6	2.2	2.4	-0.73	1.031	-0.71
A7	2.4	2.6	-0.06	1.032	-0.06
A8	2.6	2.8	-0.54	1.031	-0.53
A9	2.8	3.0	0.13	1.032	0.12

same photometric redshift values as the candidate QSOs. I chose to use the 3 Mpc radial distance to check the background values out to the largest radii. If the background values are correct, this process should give a uniform, flat radial profile and the overdensities obtained should be consistent with zero within the errors. The results are consistent with this; see Table 5.1 and Figure 5.6.

5.4 Stacked Results

5.4.1 Stacking in 3 Mpc annuli

In Figure 5.7 I show the result of stacking the source densities for the 109 $0.5 < z < 3.0$ candidate QSOs that are more than 3 Mpc from the edge of the field and subtracting the background source densities to find the mean source overdensity that is associated with the candidate QSOs. The source overdensity uncertainties are the Poisson uncertainties, added in quadrature with the average background uncertainties.
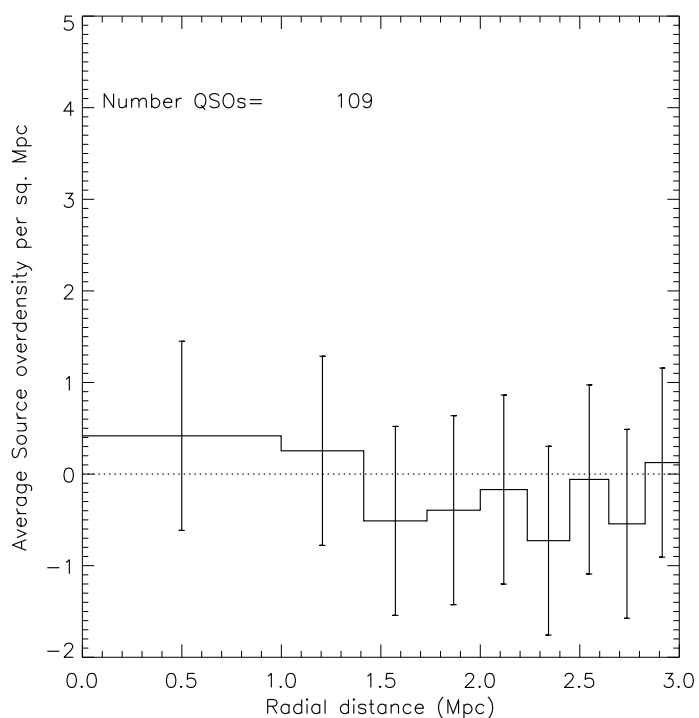
Figure 5.6: Radial profile of the source overdensity for random coordinates, at the candidate quasar photometric redshifts, where photoz > 0.5. The error bars represent the Poisson errors on the source overdensity added in quadrature with the background Poisson errors and the cosmic variance errors.

Significant ($> 3\sigma$) source overdensities are found in the < 1 Mpc environments of the candidate QSOs; in this region I detect an excess of $\sim 3.49 \pm 0.893$ galaxies at a significance of 3.90σ. This indicates that the candidate QSOs are associated with significant overdensities in the inner regions (< 1 Mpc) in their

Table 5.2: Table of the stacked source over-densities (Mpc^{-2}) found in the 3 Mpc region of the central candidate QSO and the corresponding uncertainty and significance. The inner and outer radius (Mpc) of each annulus is given in the table.

Annulus	Inner radius (Mpc)	Outer radius (Mpc)	Over-density (Mpc^{-2})	± error	σ
A1	0	1.0	3.49	0.893	3.90
A2	1.0	1.4	2.25	0.891	2.53
A3	1.4	1.7	0.93	0.889	1.05
A4	1.7	2.0	1.11	0.889	1.25
A5	2.0	2.2	0.42	0.888	0.48
A6	2.2	2.4	0.59	0.888	0.67
A7	2.4	2.6	1.14	0.889	1.29
A8	2.6	2.8	0.92	0.889	1.03
A9	2.8	3.0	0.41	0.888	0.46

Table 5.3: Stacked source overdensities (Mpc^{-2}) found in the 1 Mpc region of the central candidate QSO and the corresponding uncertainty and significance. The inner and outer radius (Mpc) of each annuli is given in the table.

Annulus	Inner radius (Mpc)	Outer radius (Mpc)	Over-density (Mpc^{-2})	± error	σ
A1	0	0.6	3.83	1.140	3.36
A2	0.6	0.84	3.19	1.139	2.80
A3	0.84	1.0	3.27	1.138	2.87

environments. The source overdensity then reduces to the background level at radii > 2 Mpc.

5.4.2 Stacking in 1 Mpc annuli

As discussed above, to include more candidate QSOs in the analysis, I have performed the same density analysis on the 1 Mpc environments of the candidate QSOs, which allows me to include 85 per cent of the candidate QSO sample that are between $0.5 < z < 3$. Most of the overdensity seen in Fig 5.7 is found within 1 Mpc, therefore this is a sensible radial distance to use.

I used three radii for the annuli: R1= 0.6 Mpc, R2= 0.84 Mpc and R3= 1
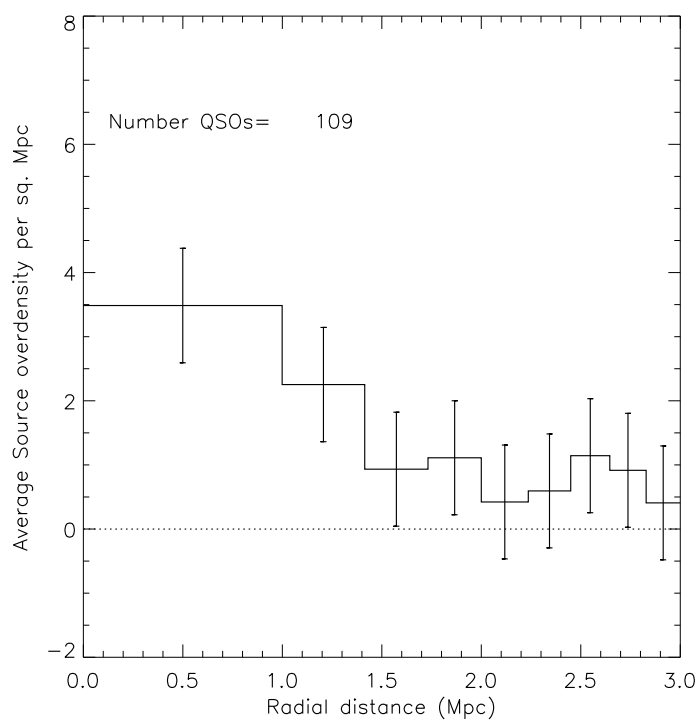
Figure 5.7: Radial profile of the source overdensity for all of the candidate QSOs within 3 Mpc, where photoz > 0.5. The error bars represent the Poisson errors on the source overdensity added in quadrature with the background Poisson errors and the cosmic variance errors.

Mpc; the area of the annuli were chosen to ensure the Poisson errors were of similar size from bin to bin. Figure 5.8 and Table 5.3 show the source overdensity within 1 Mpc environments for the 159 stacked candidate QSOs. The background values were found by counting the number of sources within 0.6 Mpc of 100 randomly

157

placed coordinates for each candidate QSO's redshift. The radius of 0.6 Mpc was chosen to calculate the sample variance between annuli. The corresponding Poisson errors were found and the sample variance errors were calculated using equation 5.4.

The first annulus has a source overdensity of 3.83 ± 1.140 galaxies Mpc^{-2} at a significance of 3.36σ, the second 3.19 ± 1.139 galaxies Mpc^{-2} at a significance of 2.80σ and the third 3.27 ± 1.138 galaxies Mpc^{-2} at a significance of 2.87σ. The first annulus, with a radius of 0.6 Mpc, has the most significant overdensity.

5.5 Density Analysis of Colour Selected candidate QSOs

Following the density analysis of my neural network selected candidate QSOs, I next performed the same density analysis on the colour selected QSOs described in Section 5.3. This checks whether the candidate QSOs that are detected using the two different methods still provide "signposts" to denser regions within $0.5 < z < 3$.

The positions of the 45 colour-selected candidate QSOs, within 3 Mpc of the edge of the field and between $0.5 < z < 3$, are shown in Figure 5.9. I chose an outer radius of 3 Mpc to investigate where the source overdensity goes to the background level and to compare to 3 Mpc environments of the ANNz selected candidate QSOs. The method described in Section 5.3 was used to perform the same density analysis for the colour selected candidate QSOs.
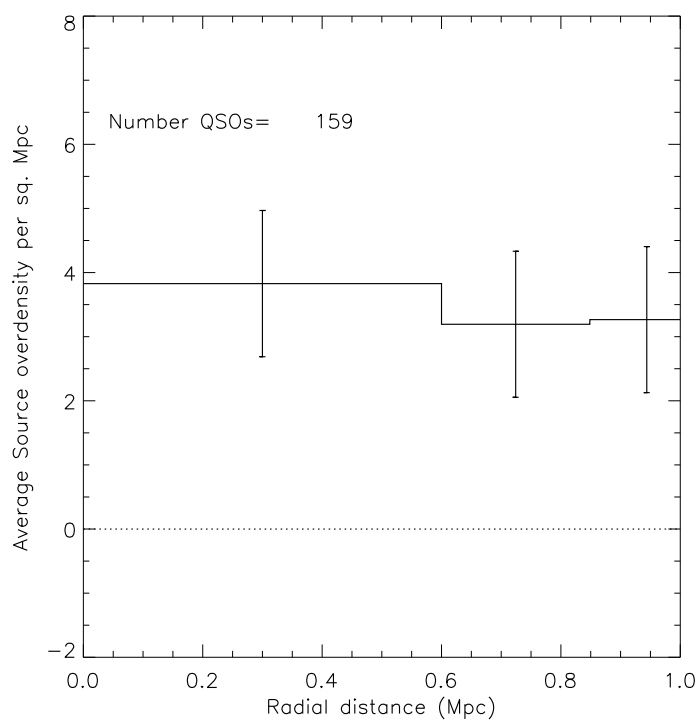
Figure 5.8: Radial profile of the source overdensity for all of the candidate QSOs within 1 Mpc, where photoz > 0.5. The error bars represent the Poisson errors on the source overdensity added in quadrature with the background Poisson errors and the cosmic variance errors.

5.5.1   Stacked candidate QSOs

I have stacked the candidate QSOs, in the manner described in Section 5.4, to see how overdense on average they are; see Figure 5.10 and Table 5.4 for the results. I find that there are no significant overdensities detected in the 3 Mpc
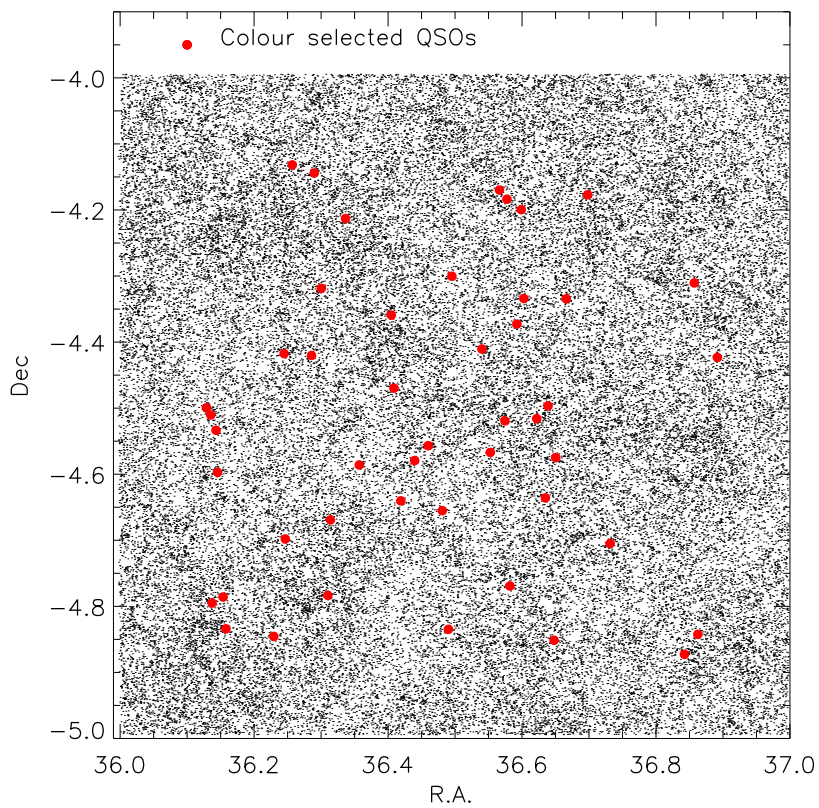
Figure 5.9: Plot of the R.A. and Dec of the colour selected candidate QSOs (red dots) and all of the VIDEO data (black points) that are 3 Mpc away from the edge of the field.

environments for the colour-selected candidate QSOs.

Comparing these values to the neural network selected candidate QSOs (Figure 5.10) I find that the colour selected candidate QSOs do not show a significant

Table 5.4: Table of the stacked source over-densities (Mpc^{-2}) found in the 3 Mpc region of the central colour selected candidate QSOs and the corresponding uncertainty and significance. The inner and outer radius (Mpc) of each annuli is given in the table.

Annulus	Inner (Mpc)	Outer (Mpc)	Over-density (Mpc^{-2})	$\pm$ error	σ
A1	0	1.0	0.69	1.202	0.58
A2	1.0	1.4	1.56	1.204	1.30
A3	1.4	1.7	-1.10	1.197	-0.93
A4	1.7	2.0	1.12	1.203	0.93
A5	2.0	2.2	-0.52	1.198	-0.43
A6	2.2	2.4	-0.25	1.199	-0.21
A7	2.4	2.6	0.15	1.200	0.12
A8	2.6	2.8	-0.13	1.199	-0.11
A9	2.8	3.0	-0.54	1.200	-0.45

overdensity within 1 Mpc. I have compared the ANNz candidate QSOs with the colour selected candidate QSOs (45 within $0.5 < z < 3$) and I only find 4 ANNz candidate QSOs that are also found in the colour selected sample. The differences between the environments of the two candidate QSO samples may be due to the candidate QSOs in both the colour and ANNz selected samples having significantly different photometric redshift distributions. Figure 5.11 shows the different photometric redshift distributions for both samples. This needs to be taken into account because the colour-selected candidate QSOs, which are found at higher photometric redshifts, will trace clusters that have fewer galaxies and thus the overall source overdensity will be lower compared to the ANNz-selected candidate QSOs. A fair comparison between the samples thus requires a redshift-independent density measurement; this will be discussed further in Chapter 6.
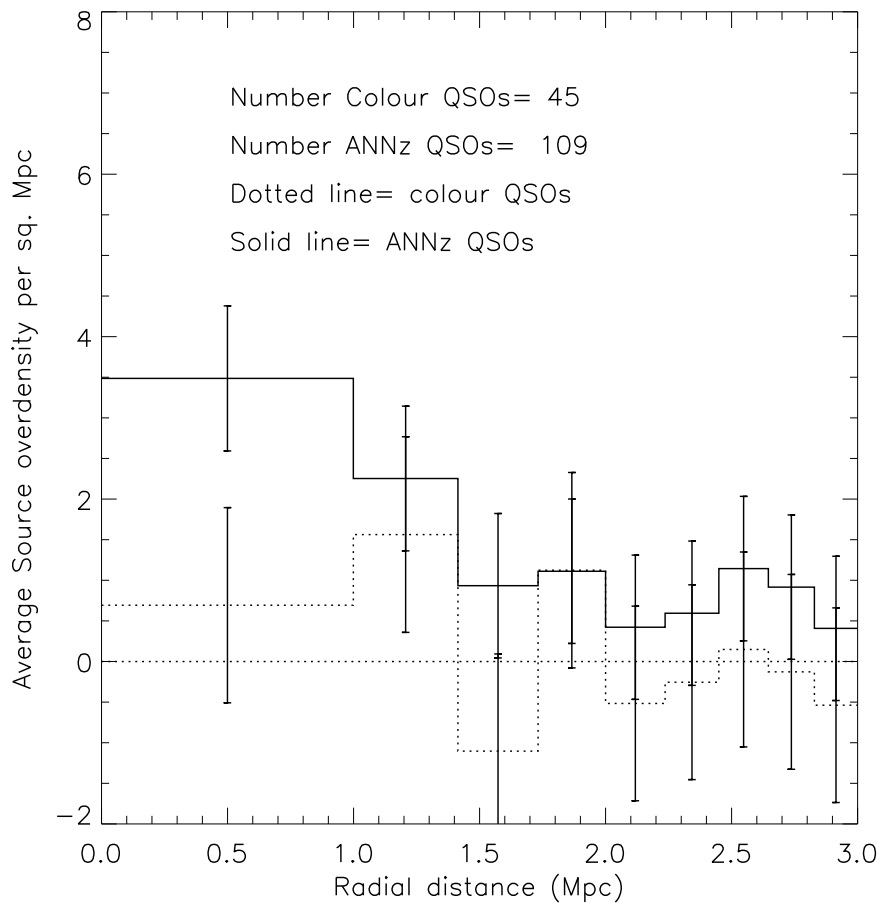
Figure 5.10: Histograms of the source overdensity of the environments of the stacked colour selected candidate QSOs between $0.5 < z < 3.0$ (dotted line) overplotted on the histogram of the ANNz candidate QSOs source overdensity (solid line). The error bars are the Poisson uncertainties added in quadrature with the cosmic variance uncertainties.
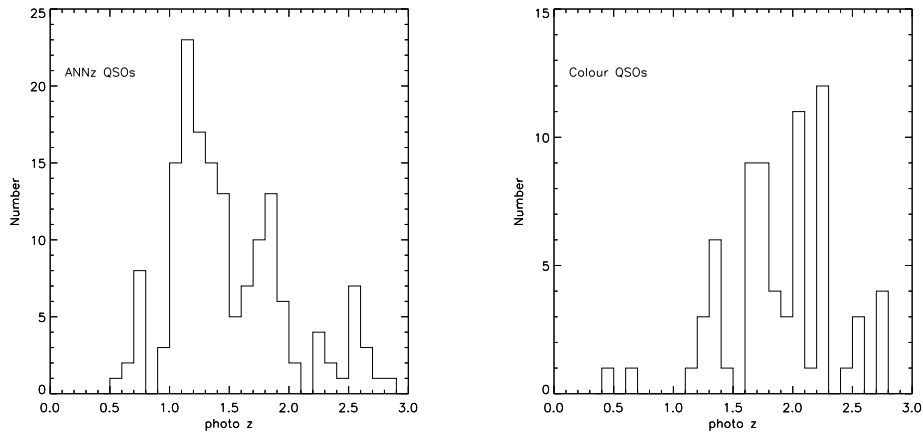
Figure 5.11: The photometric redshift distribution for the ANNz and colour selected candidate QSOs.

5.6 The Environments of Radio-Loud and Radio-Quiet candidate QSOs

5.6.1 Cross Matching

To split the candidate QSOs into radio-loud and radio-quiet subsets I have cross matched them with the VLA 1.4 GHz radio catalogue which is described by Bondi et al. (2003) and is outlined in Chapter 2. The resolution of the radio data is 6 arcsecs with a positional accuracy of up to 0.9 arcsecs (1σ) for the faintest sources from Bondi et al. (2003) and the positional accuracy of the VIDEO data is < 0.1 arcsecs, so the dominant source of uncertainty on the positions is from the radio data (McAlpine et al., 2012). I chose to cross match the coordinates of the candidate QSOs within 5 arcsec of the coordinates of the radio data. This

was chosen to obtain the largest number of cross matched candidate QSOs but to also take into account the uncertainty on the radio positions. I found that 37 of the candidate QSO sample had radio counterparts: 24 of these were between $0.5 < z < 3$ and were beyond 1 Mpc of the edge of the field, and so could be included in the radio-loud sample.

The radio-detected candidate QSOs were chosen to have 1.4 GHz flux density of greater than 85μJy which is the 5σ limit of the VLA survey; see Fig 5.12 for their range of radio luminosities. The radio luminosities were calculated using

$$L_{1.4\text{GHz}} = \frac{4\pi \text{ Flux}_{1.4\text{GHz}} D_L^2}{(1+z)^{1-\alpha}}, \tag{5.5}$$

where flux is in $\text{Wm}^{-2}\text{Hz}^{-1}$, D_L is the luminosity distance in metres, z is the candidate QSO's photometric redshift and I assume the spectral index is $\alpha = 0.7$ (Falder et al., 2010).

To estimate the luminosity of the non-detected objects I chose to assign them an upper limit of 85μJy which is at the 5σ limit of the survey and by assigning them a spectral index of 0.7 I was able to calculate upper limits on their radio luminosities. I compare these to a standard definition of radio loudness (Ivezić et al., 2002), which was outlined in Chapter 3. In Figure 5.13 I show the optical flux density versus the radio flux density for the radio-detected candidate QSOs and upper limits for the non-radio detected candidate QSOs. The line defines the radio loudness criteria of $R_i = 1$; above this line the candidate QSOs are radio-loud by the definition of Ivezić et al. (2002) and below they are radio-quiet. Figure 5.13 shows that almost all radio-detected objects are genuine RLQs, though it is possible that some RL objects also contaminate the non-detected

Table 5.5: Table of the stacked source over-densities (Mpc^{-2}) found in the 1 Mpc region of the central radio and non-radio selected QSOs and the corresponding uncertainty and significance. The inner and outer radius (Mpc) of each annulus is given in the table.

Annulus	Inner radius	Outer radius	Over-density (Mpc^{-2})	$\pm$ error	σ
Radio loud					
A1	0	0.6	10.63	2.853	3.72
A2	0.6	0.84	4.47	2.814	2.59
A3	0.84	1.0	6.94	2.830	2.45
Radio quiet					
A1	0	0.6	2.62	1.243	2.11
A2	0.6	0.84	2.97	1.244	2.38
A3	0.84	1.0	2.61	1.233	2.10

sample. For simplicity, I will refer to the radio-detected sample as RLQs and the non-detected objects as RQQs in what follows.

I have also created a conservative candidate QSO sample, which I will use in Chapter 6. I used all of the radio-detected objects except for the 3 that the radio loudness criterion designates as RQQs (total 22 RLQs). I have also used all of the radio non-detected objects that the radio loudness criterion designates as RQQs (total 30 RQQs). The environments of these will be compared in Chapter 6.

5.6.2 Radio Density Environments

To compare the RLQ sample with the RQQ sample I checked the match between their redshift and absolute magnitude (K_s-band) distributions using a K-S test. The probability under the null hypothesis was 0.53 for the redshift distributions and 0.12 for the absolute magnitude distributions, so the null hypothesis is not rejected and the distributions are not significantly different. Figure 5.15 shows the photometric redshift and absolute magnitude distributions for the two candidate
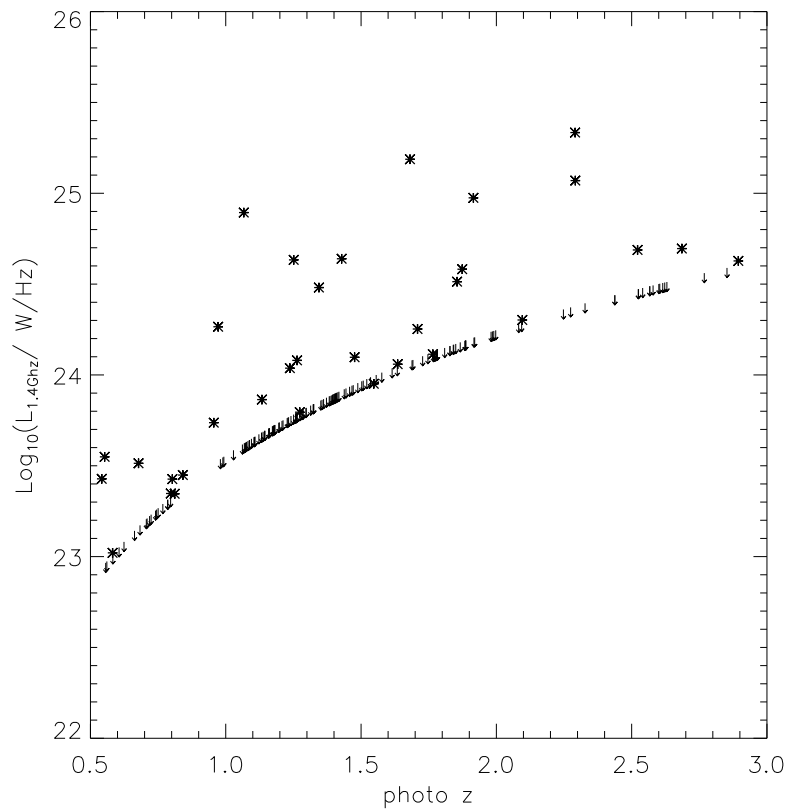
Figure 5.12: Radio luminosity (1.4 GHz) for the radio-detected candidate QSOs (asterisks) and the upper limits for the non-radio detected candidate QSOs (arrows).
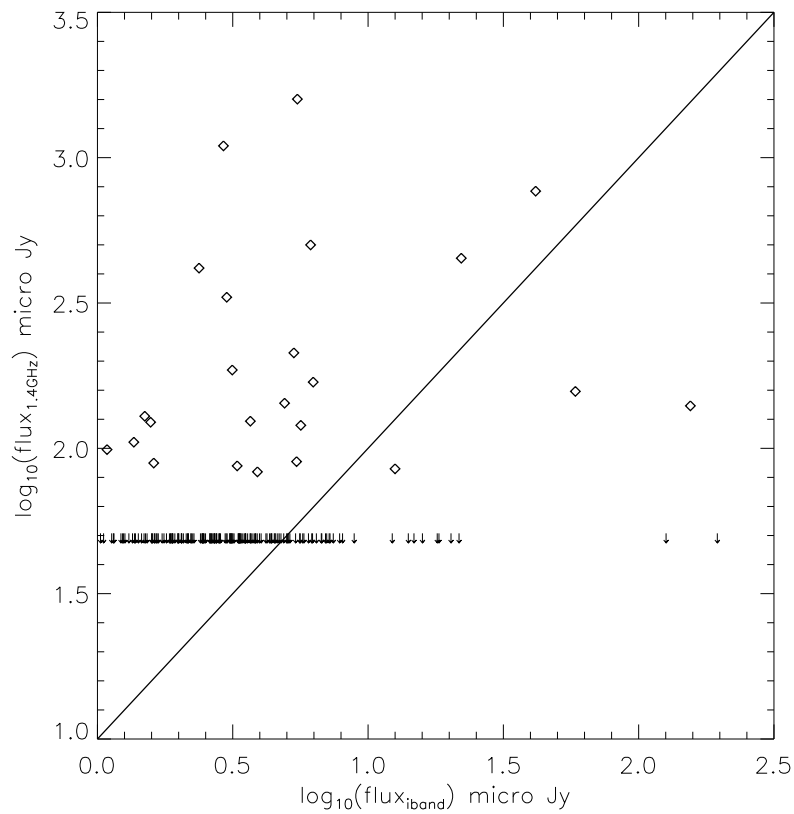
Figure 5.13: The optical flux (i band) versus the radio flux (1.4GHz) for the candidate quasar samples. The radio-detected objects are plotted as diamonds while the non-detections are shown as upper limits. The line shows the parameter $R_i = 1$, which is used to determine radio-loudness (Ivezić et al., 2002).
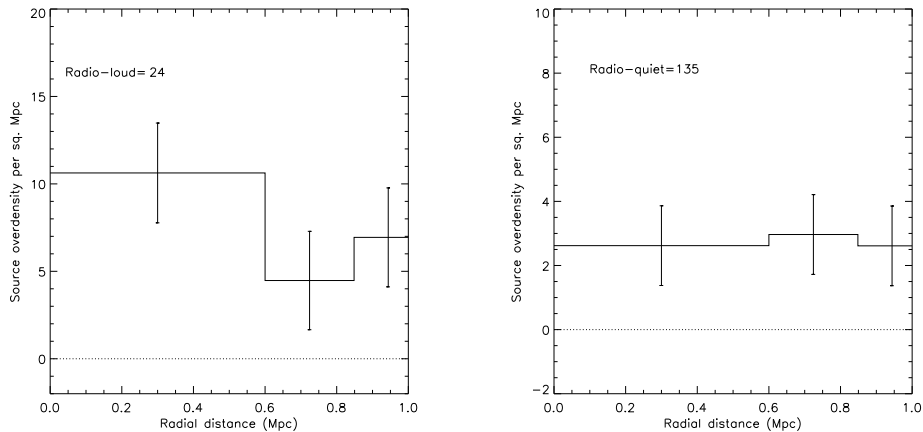
Figure 5.14: Radial profiles of the stacked source overdensity of the environments of the radio-loud and radio-quiet ANNz selected candidate QSOs between $0.5 < z < 3.0$. The error bars are the Poisson uncertainties added in quadrature with the cosmic variance uncertainties.

QSO samples. As the candidate QSO samples do not have significantly different distributions in either quantity, I do not expect any bias when comparing the source overdensity of their environments.

I compared the source overdensity within the 1 Mpc candidate QSO environments for the radio-loud and radio-quiet candidate QSOs; see Figure 5.14 and Table 5.5 for the source overdensities. I find that the radio-loud candidate QSOs lie in significant ($> 3\sigma$) source overdensities within 0.6 Mpc and have a factor of 4.06 ± 2.21 larger source overdensity than the RQQs. This agrees with the findings of Falder et al. (2010), who showed that the radio-loud QSOs are in denser environments compared to the radio-quiet QSOs. These results will be discussed in more detail in Chapter 6.
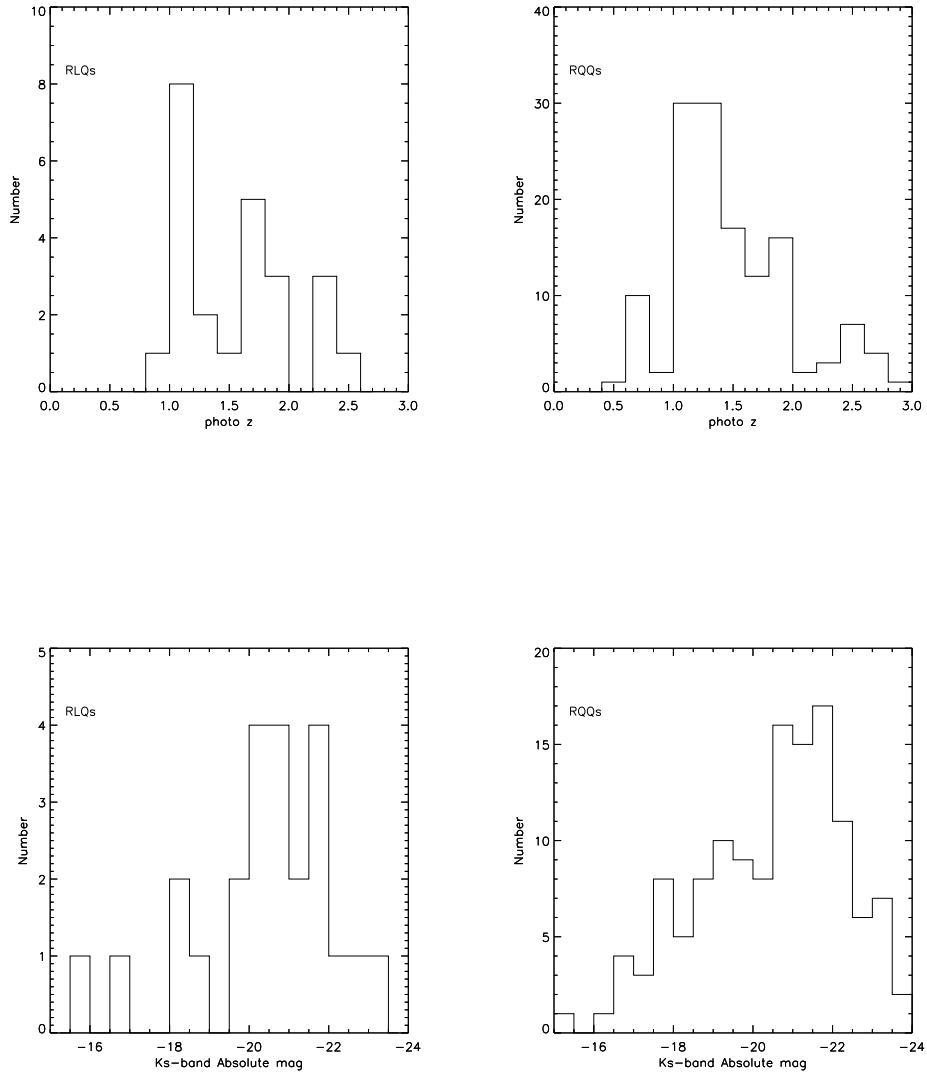
Figure 5.15: The redshift and absolute magnitude (K_s-band) distribution for the RLQs and the RQQs.

5.7 Galaxy Types

In this Section I investigate the types of galaxies in the overdense environments of the VIDEO candidate QSOs. The main aims are to see what type of galaxies are found in the environments of the candidate QSOs, to see what fraction of ellipticals, Sbc, Scd, irregular or star-forming galaxies are the main contributors and to investigate whether these change depending on the radial distance, photometric redshift or radio loudness of the candidate QSOs. This will allow me to look for evidence for candidate QSOs affecting their environments and to investigate whether there is a difference in the type of galaxy in the environments of the RLQs and RQQs. This is possible because a galaxy template was fitted to each of the objects in the VIDEO catalogue to determine the photometric redshifts and therefore I have the best estimate of galaxy type for each object.

The galaxies were fitted using 6 types of galaxy templates which were produced by Arnouts et al. (2007). The templates included an elliptical (E11), two spirals (Sbc, Scd), an irregular galaxy (Irr) and two starburst (SB) galaxies.

This analysis uses the same method described in Section 5.3. I use a radial analysis of the 3 Mpc environments to investigate whether the type of galaxies changes depending on radial distance from the central candidate QSO. Each radial bin is kept to the same area to ensure the Poisson errors are similar from bin to bin. The main difference is that I split the number of galaxies up into 3 types; ellipticals, Sbc/Scd/Irregular and star-forming.

I also perform a background density analysis, similar to that of Section 5.3.2, using a radius of 1 Mpc (radius of 1 annulus) and counting the number of galaxies in the three sub types that I find. This allows me to remove the expected back-

ground level from the number of galaxies in the candidate QSO environments, leaving me the excess number of galaxies for each galaxy type. Using a radius of 1 Mpc allows me to calculate the sample variance and Poisson uncertainties for each annulus.

5.7.1 Stacked Galaxy Type

In Figure 5.16 I have stacked the source overdensities for all of the candidate QSOs between $0.5 < z < 3$ and split them into the 3 galaxy types. A 3 Mpc radial profile was used to investigate whether galaxy type changed as a function of radius. From this figure it is clear that the type of galaxies does not change as a function of radius. I find that the majority of the source overdensity in the candidate QSOs environments comes from an overdensity of spiral and irregular galaxies rather than starburst and elliptical galaxies. The fraction of the galaxy types are shown in Table 5.6 for the whole candidate QSO sample and the background sample. The fraction of galaxies in the QSO environments are consistent with the fraction of galaxies in the background field.

5.7.2 Galaxy type and RLQ/RQQ class

I have split the candidate QSOs up into RLQs and RQQs as described in Section 5.6 and have investigated the type of galaxies in their environments. In Figure 5.17 I show the overdensities in the vicinity of the RLQs for the spiral/irregular, elliptical and starburst galaxies. I find that the spiral/irregular galaxies make the largest contribution to the source overdensity with 4.56 ± 1.46 Mpc^{-2} at a significance of 3.11σ within a radius of 1.4 Mpc when compared
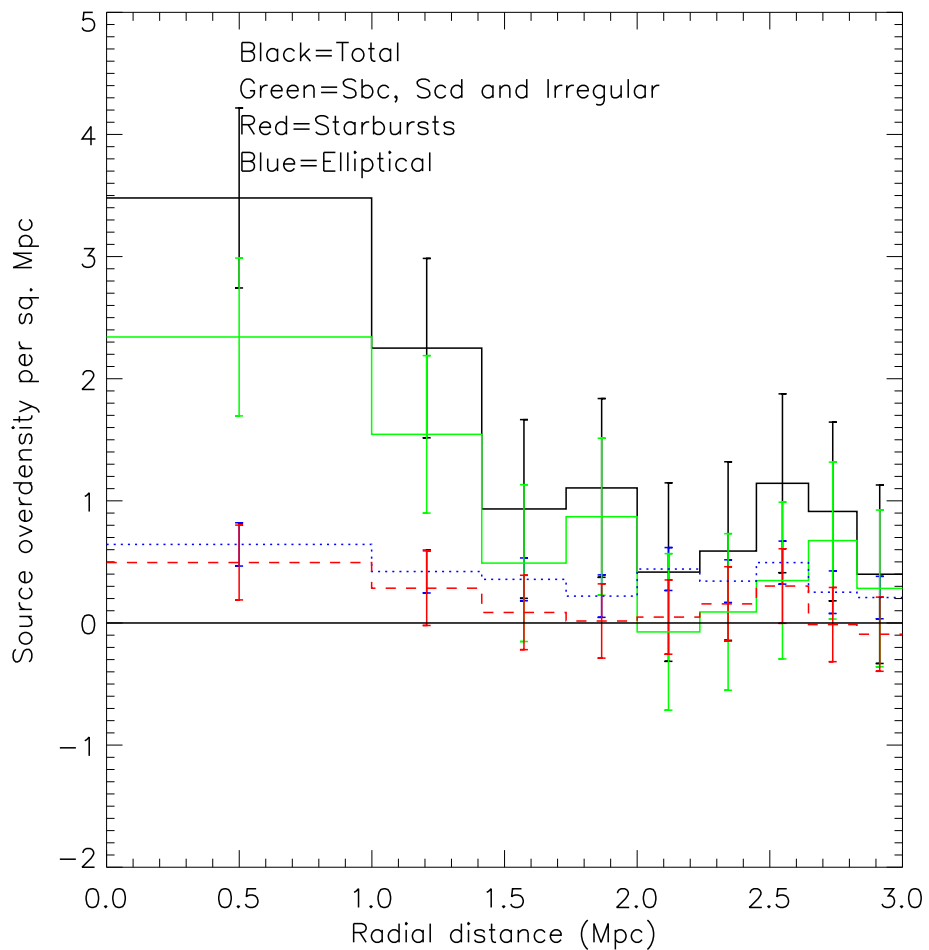
Figure 5.16: The source overdensity per Mpc^2 for elliptical (blue dotted line), spiral and irregular (green solid line), starburst (red dashed line) and the total galaxies (black solid line) in the environments of the 109 QSOs ($0.5 < z < 3$). The error bars represent the Poisson errors on the source overdensity added in quadrature with the background Poisson errors and the cosmic variance errors.

to the starburst galaxies. The starburst galaxies do show a source overdensity of 1.57 ± 0.71 beyond 1.4 Mpc radial distance at a significance of 2.22σ. Similar to what is seen in Fig 5.16 the source overdensity is made up of mainly spiral and irregular galaxies with a small contribution of starburst galaxies and elliptical galaxies.

I have also investigated the source overdensities within the environments of the RQQs. In Figure 5.18 I compare the source overdensities of the spiral/irregular galaxies with the starburst galaxies in the 3 Mpc RQQ environments. I find no difference between the type of galaxies found in the RLQ and RQQ environments.

In Table 5.6 I show the fraction of spiral, irregular, elliptical and starburst galaxies found in the 1 Mpc environments of the RLQs and RQQs. I choose 1 Mpc because it has the largest source overdensity.

From these it is clear that the Spiral/Irregular galaxies contribute the bulk of the overdensity for the whole, RQQs and RLQs samples. The fraction of starburst galaxies in all of the candidate QSO and galaxy environments tend to be below the fraction in the background; however, the uncertainties are large so it is difficult to say for certain whether they are being suppressed in the densest environments.

5.8 Comparison to Galaxy Samples

To compare my density results for the candidate QSOs environments to dense regions around galaxies without QSOs I have created galaxy samples and investigated their environmental density. I have chosen two different methods to create galaxy samples, one chooses galaxies at random within certain redshift increments
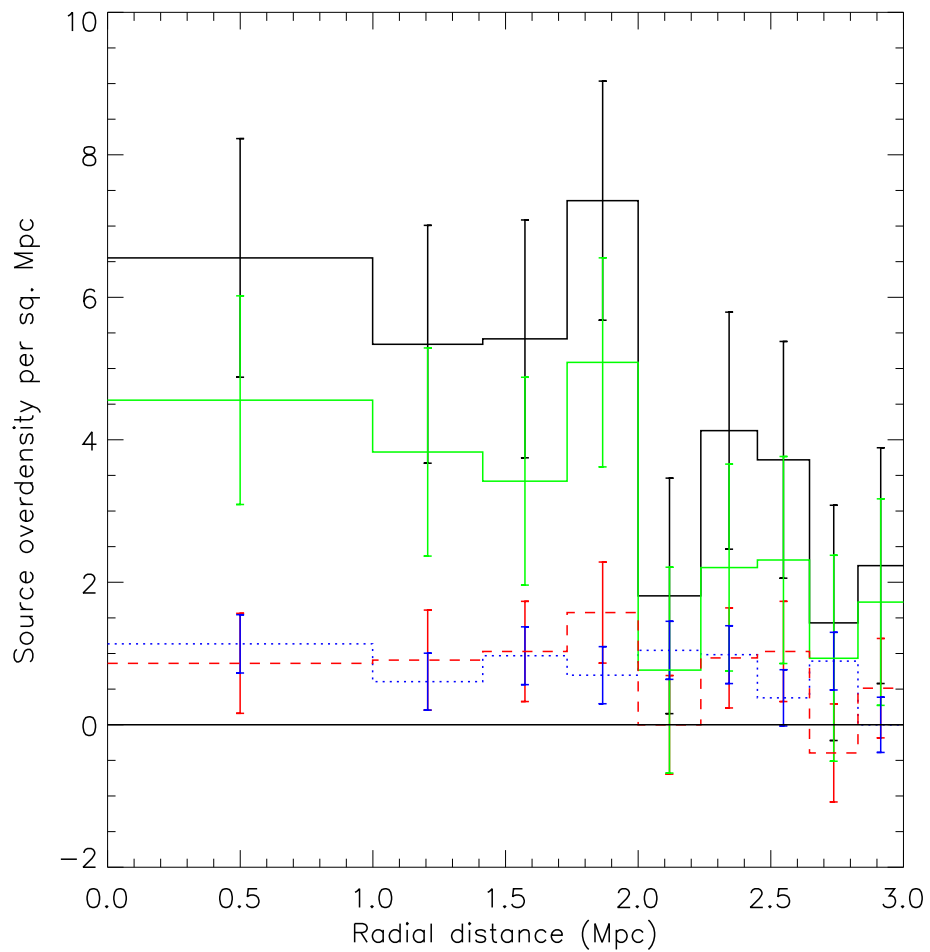
Figure 5.17: The source overdensity per Mpc^2 for spiral/irregular (green solid line), elliptical (blue dotted line), starburst (red dashed line) and the total galaxies (black solid line) in the environments of the 21 RLQs. The error bars represent the Poisson errors on the source overdensity added in quadrature with the background Poisson errors and the cosmic variance errors.
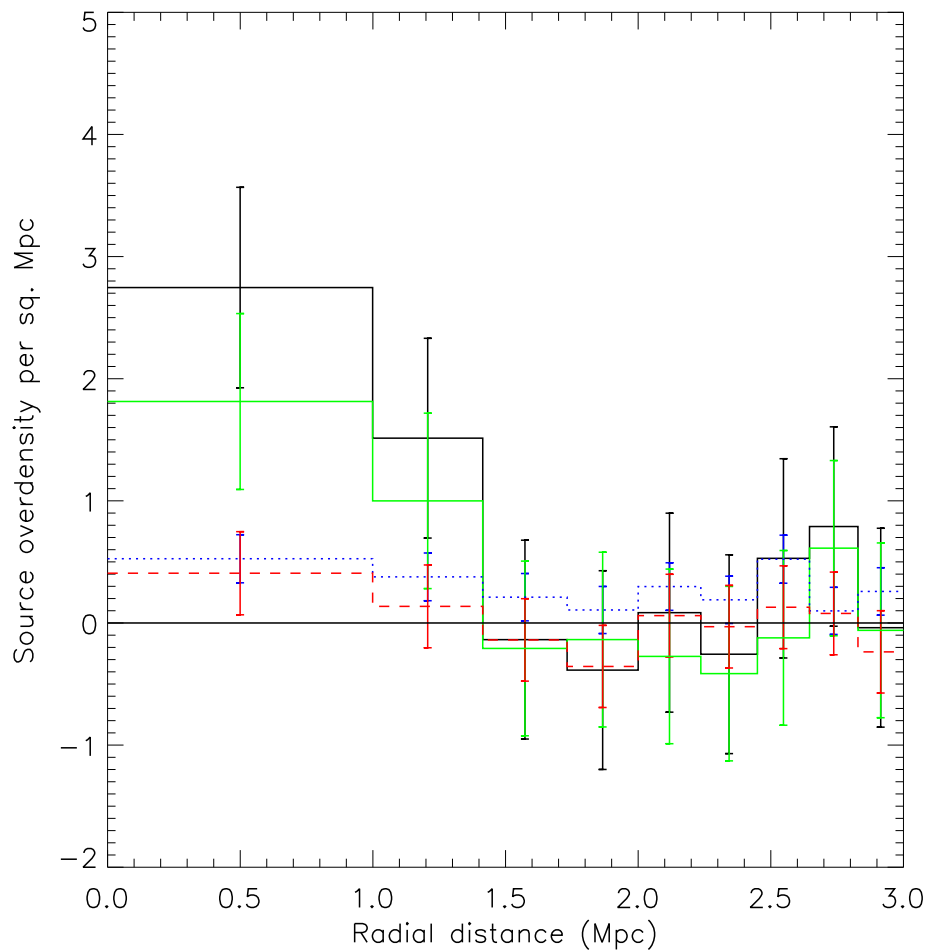
Figure 5.18: The source overdensity per Mpc^2 for spiral/irregular (green solid line), elliptical (blue dotted line), starburst (red dashed line) and the total galaxies (black solid line) in the environments of the 88 RQQs. The error bars represent the Poisson errors on the source overdensity added in quadrature with the background Poisson errors and the cosmic variance errors.

Table 5.6: The fraction of the 3 type of galaxies found in the 1 Mpc region of the whole sample, QSOs subsamples and Galaxy subsamples.

Sample	Elliptical	Spiral/Irr	Starbursts
Whole	0.185± 0.064	0.673 ± 0.234	0.142 ± 0.093
Background	(0.087 ±0.002)	(0.697 ± 0.006)	(0.216 ± 0.004)
RLQs	0.173 ± 0.062	0.695 ± 0.223	0.132 ±0.107
Background	(0.086 ± 0.005)	(0.697 ±0.015)	(0.217 ± 0.008)
RQQs	0.191± 0.072	0.660 ± 0.262	0.148 ± 0.124
Background	(0.087 ± 0.002)	(0.697 ± 0.007)	(0.216 ± 0.004)
Galaxy B	0.054± 0.089	0.739 ± 0.28	0.206 ±0.125
Background	(0.099 ± 0.002)	(0.699 ± 0.006)	(0.202 ± 0.003)

(Galaxy sample A) and the other chooses the 10 brightest galaxies brighter than a magnitude limit and matched to the candidate QSO's redshifts (Galaxy sample B). I adopted these two different methods to investigate which one is successful at detecting overdensities.

5.8.1 Galaxy Sample A

I have created a random sample of 290 galaxies in total. These were chosen by choosing 10 random galaxies in each bin of 0.1 photometric redshift increments between $0.1 < z < 3$ and brighter than a K_s magnitude of -22.0 ($L_\star$). I then performed the same density analysis, which is outlined in Section 5.3 on the environments of the galaxies. I have used the same redshift slices to keep it consistent with the analysis of the candidate QSO environments. This provided the number density of objects and a background value all within 1 Mpc of the galaxies. From these I could then perform the analysis on the types of galaxies found in the environments of the galaxies.

In Figure 5.19 I show the source overdensity for the different galaxy types in the 3 Mpc environments of the random selected galaxy sample. There are

no significant overdensities found in the environments of the randomly selected galaxies.
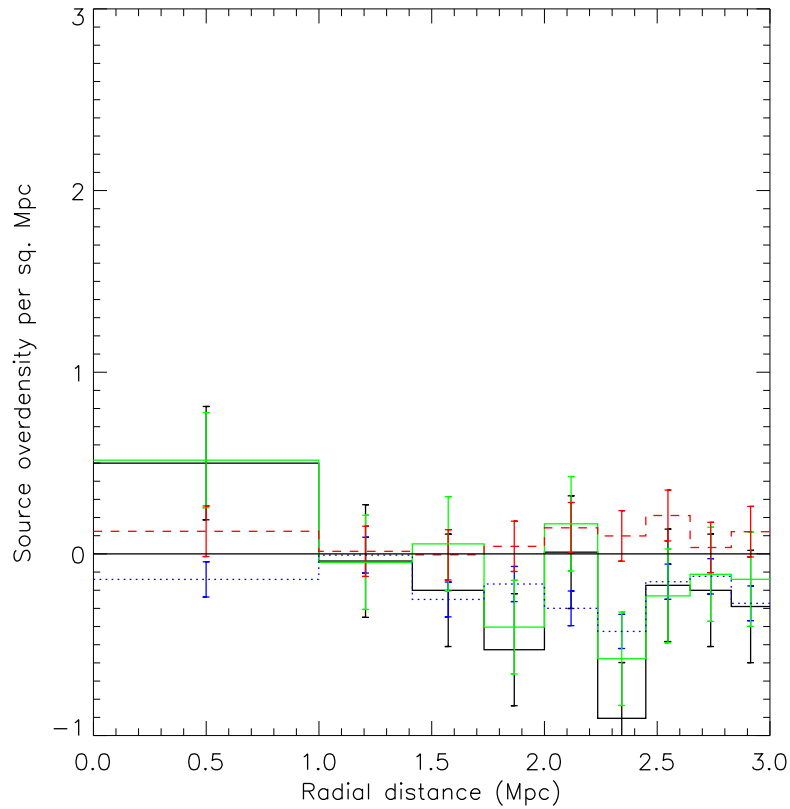
Figure 5.19: The source overdensity per Mpc^2 for spiral/irregular (green solid line), elliptical (blue dotted line), starbursts (red dashed line) and the total galaxies (black solid line) in the environments of the 290 random galaxy sample. The error bars represent the Poisson errors on the source overdensity added in quadrature with the background Poisson errors and the cosmic variance errors.

5.8.2 Galaxy Sample B

I have created another sample of 274 galaxies. These were matched with the candidate QSO's photometric redshifts to be able to compare the galaxy environments with the QSO environments. This was done by choosing the nearest galaxy in redshift space within $z = \pm 0.01$ of the candidate QSO's photometric redshifts and choosing the nearest galaxy that was brighter than $K_s = -22.0$. The photometric redshift distributions for the candidate QSO and galaxy samples are similar; see Figure 5.20. The same density analysis was performed on the galaxy environments as described in Section 5.3.

In Figure 5.21 the source overdensity is shown for the brightest galaxy sample. They trace dense regions in the VIDEO-XMM3 field, see Table 5.7 for the source overdensities. The largest source overdensity of 2.89 ± 0.642 Mpc^{-2} at a significance of 4.5σ is found within < 1 Mpc of the brightest galaxies.

The main type of galaxies that contribute to these overdensities are spiral/irregular galaxies; there is very little contribution from starburst and elliptical galaxies. The fraction of the galaxy types in the galaxy environments is shown in Table 5.6. The spiral/irregular galaxies contribute the most to the background and galaxy overdensities but the fraction of starbursts differ between these.

5.9 Discussion

In this section I discuss the differences between the source overdensities within the environments of the candidate QSO and galaxy samples. I also discuss the type of galaxies found in both type of environments. A full discussion of the possible reasons why the RLQs are found in denser environments is presented in
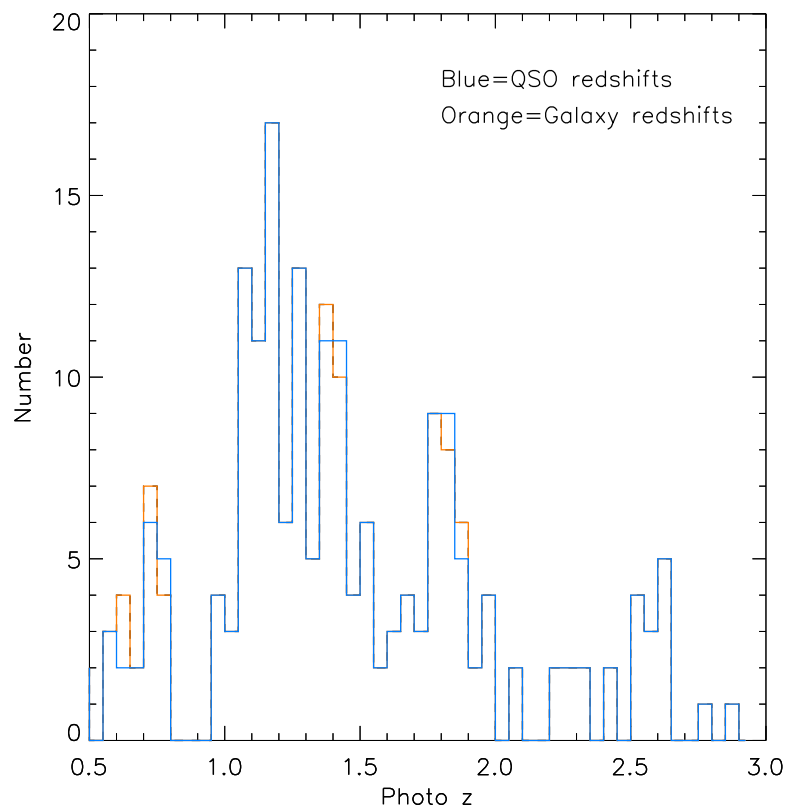
Figure 5.20: Photometric redshift distribution of the candidate QSOs (blue) and the galaxies (orange).

Section 6.5 (Chapter 6).

Table 5.7: Table of the stacked source over-densities (Mpc^{-2}) found in the 3 Mpc region of the brightest selected galaxies and the corresponding uncertainty and significance. The inner and outer radius (Mpc) of each annulus is given in the table.

Annulus	Inner radius	Outer radius	Over-density (Mpc^{-2})	$\pm$ error	σ
A1	0	1.0	2.89	0.642	4.50
A2	1.0	1.4	2.87	0.642	4.46
A3	1.4	1.7	2.22	0.641	3.47
A4	1.7	2.0	2.10	0.641	3.29
A5	2.0	2.2	1.92	0.640	3.00
A6	2.2	2.4	2.07	0.641	3.23
A7	2.4	2.6	1.64	0.640	2.56
A8	2.6	2.8	1.83	0.640	3.86
A9	2.8	3.0	1.76	0.639	2.75

5.9.1 The QSO and galaxy environments

I have investigated the source overdensity in the 1 Mpc candidate QSO environments and found that they reside in overdensities of 3.49 ± 0.893 Mpc^{-2} at a significance of 3.90σ. I found that they also reside in overdensities of 3.83 ± 1.140 Mpc^{-2} at a significance of 3.36σ when I investigated their 0.6 Mpc environments. There are many authors that find similar overdensities associated with QSOs (e.g Falder et al. 2010; Galametz et al. 2010; Mayo et al. 2012; Wylezalek et al. 2013). Therefore, I find that QSOs are "good" tracers of dense regions in the high redshift Universe.

However, models by Angulo et al. (2012) and Fanidakis et al. (2013) have found that quasars are associated with average density environments rather than the most dense environments up to $z \sim 4$. This seems to contradict observations because quasars have been found to trace dense environments at high redshifts.

To test whether quasars do reside in the most overdense regions I have determined the source overdensity in the environments of the brightest selected
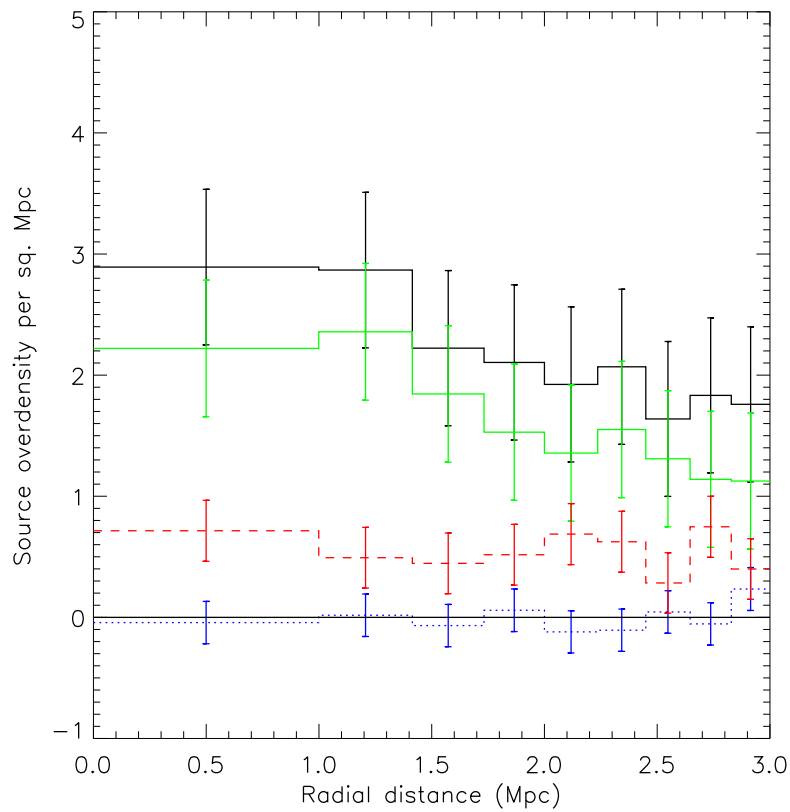
Figure 5.21: The source overdensity per Mpc^2 for spiral/irregular (green solid line), elliptical (blue dotted line), starbursts (red dashed line) and the total galaxies (black solid line) in the environments of the 290 brightest galaxy sample. The error bars represent the Poisson errors on the source overdensity added in quadrature with the background Poisson errors and the cosmic variance errors.

galaxies. This shows whether bright galaxies are "good" tracers of dense regions because the more luminous galaxies are thought to live in more massive haloes than less luminous galaxies (Norberg et al. 2001; Zehavi et al. 2005). I have found that the bright galaxies do reside in overdensities of 2.89 ± 0.642 Mpc^{-2} at a significance of 4.50σ within 1 Mpc of the central galaxy. This implies that not only quasars are useful at tracing dense regions but bright galaxies are too.

The associated source overdensity for the candidate QSOs as a whole in their 1 Mpc environments is consistent with the source overdensity of the galaxies (the ratio between them is 1.208 ± 0.41). This suggests that, in our sample, candidate quasars and the brightest galaxies are found in the largest source overdensities compared to the field.

However, the associated source overdensity for the RLQs in their 0.6 Mpc environments is a factor of 3.678 ± 1.28 greater than the source overdensity found for the galaxy environments, this is at a significance of $\sim 3\sigma$. This suggests that RLQs are better traces of overdensities compared to the galaxy sample. Further discussion of these differences can be found in Section 6.5.

5.9.2 Environments and galaxy types

I have investigated the type of galaxies found in the RLQ, RQQ, galaxy and background environments. I found that the largest contribution to the overdensity was from spiral/irregular galaxies with small contributions from elliptical and starburst galaxies in all AGN and galaxy samples. I might expect there to be a lower fraction of starburst galaxies in the most dense environments because the level of star-formation has been found to be suppressed in the denser environments

through process such as galaxy interactions and ram pressure stripping (Gunn & Gott 1972; Oemler 1976; Larson et al. 1980; Moore et al. 1996). AGN feedback, such as the mechanical mode, has also been found to suppress the level of star formation in massive galaxies (Bower et al. 2006; Croton et al. 2006).

However, I find no evidence for this happening in the denser environments. This might suggest that at high redshifts ($z > 0.5$) there is still a lot of star formation compared to the level of star formation found in clusters at low redshifts ($z < 0.5$) (Butcher & Oemler 1984). Many studies have found a large amount of star-formation in the environments of AGN between $2 < z < 6$ (Ivison et al. 2000; Stevens et al. 2003; Stevens et al. 2004; Priddey et al. 2008; Stevens et al. 2010). This may suggest that processes such as AGN feedback and processes found in dense environments have not yet had an effect at high redshifts. For example, ram pressure stripping (Gunn & Gott, 1972) is not expected to be as effective at high redshifts (Dolag et al., 2009), this is because ram pressure stripping depends on the ICM density and the lower ICM densities found at high redshifts can lead to inefficient removal of halo gas (Bekki, 2009).

The lack of star formation suppression might be expected in the context of the picture of cosmic downsizing (Cowie et al., 1996), where the number density of galaxies increases towards low redshifts (Mo & White, 2002) but star formation decreases. This is possibly due to AGN feedback and processes occurring in denser environments to suppress star formation (Quilis et al. 2001; Brüggen & Kaiser 2002; Churazov et al. 2002; Dalla Vecchia et al. 2004; Sijacki & Springel 2006).

These are tentative results because the uncertainties on the fraction of galaxy types are large. To improve on the significance of the statistics a larger sample

is needed.

5.10 Summary

In this chapter I have investigated the density environments of the ANNz selected VIDEO candidate QSO environments and the colour selected candidate QSO environments. This was done by stacking the source overdensities and investigating the candidate QSO's environments individually. Furthermore, I investigated whether the radio-loud QSOs resided in denser < 1 Mpc environments than the radio-quiet QSOs. This was made possible by the VLA 1.4 GHz radio catalogue which could be matched with the VIDEO catalogue.

1. Significant overdensities have been found in the 1 Mpc environments of the stacked and the individual selected VIDEO candidate QSOs. This is consistent with the results of Falder et al. (2010) and Falder et al. (2011), where the main overdensities were found within 1 Mpc of the QSOs.

2. For a comparison, the colour selected candidate QSO sample does not show significant detections of overdensities. This is plausibly due to the different photometric redshift distributions between the ANNz selected and colour selected sample.

3. The radio-loud QSOs are found to reside in significant ($> 3\sigma$) source overdensities within their 1 Mpc environments. The radio-loud QSOs reside in larger overdensities, 10.63 ± 2.85 sources Mpc^{-2}, at a significance of 3.72σ within 0.6 Mpc, compared to the radio-quiet quasars which have source overdensities of 2.62 ± 1.243 sources Mpc^{-2} at significances of 2.11.

4. The main galaxies found in both the RLQ and RQQ environments and the brightest galaxy environments are spiral and irregular galaxies, with small contributions from elliptical and starburst galaxies.

5. I find no evidence to suggest that star formation is suppressed in the candidate QSO or galaxy environments compared to the field. This may suggest that there is a difference between the level of star formation found in low redshift clusters compared to high redshift clusters, however, due to the uncertainties it is difficult to say for certain that this effect is happening.

Chapter 6

The B_{gq} Density Analysis

In this Chapter I use an alternative density measurement, the B_{gq} clustering amplitude measurement, to investigate whether the RLQs occupy environments that are different from those of RQQs.

The B_{gq} clustering analysis is a density analysis which was devised by Longair & Seldner (1979) to investigate the clustering of galaxies around extragalactic radio sources. This clustering analysis has further been used by McLure & Dunlop (2001b) and Wold et al. (2001) to investigate the clustering of powerful radio-loud and radio-quiet AGN. This enables me to compare the B_{gq} values found using the VIDEO sample to the values found in the literature.

This clustering analysis is used because it includes the integrated luminosity function in the calculations. This enables a comparison between the environments of the QSOs at different redshifts, as the density results are normalized by the expected number of objects at each redshift given the absolute magnitude limit of the data.

Table 6.1: Best-fitting parameters for the Schechter LF as found by Cirasuolo et al. (2010).

Parameter	Value
α	-1.07 $\pm$ 0.1
$M_K^*(z = 0)$	-22.26 (fixed)
Z_M	1.78 $\pm$ 0.15
K_M	0.47 $\pm$ 0.2
Z_ϕ	1.70 $\pm$ 0.09
K_ϕ	1.47 $\pm$ 0.1
$\phi_0(z = 0)$	$(3.5 \pm 0.4) \times 10^{-3} (\mathrm{Mpc}^{-3})$

6.1 K-band Luminosity Function

I used the rest-frame K-band luminosity function (LF) derived by Cirasuolo et al. (2010) which describes the cosmological evolution of the galaxy LF from $z = 0$ to $z \simeq 4$. They assume the shape of the luminosity function to be of the form of the Schechter function (Schechter, 1976):

$$\phi(\mathrm{M}) = 0.4\ln(10)\phi_0 10^{-0.4\Delta\mathrm{M}(\alpha+1)}\exp(-10^{-0.4\Delta\mathrm{M}}) \tag{6.1}$$

where $\Delta\mathrm{M} = \mathrm{M_K} - \mathrm{M_K^*}$. They assume both a luminosity and density evolution with redshift which is parametrised as

$$M_K^*(z) = M_K^*(z = 0) - \left(\frac{z}{z_M}\right)^{K_M}, \tag{6.2}$$

$$\phi_0(z) = \phi_0(z = 0) \times \exp\left[-\left(\frac{z}{z_\phi}\right)^{K_\phi}\right]. \tag{6.3}$$

The best fitting values of the free parameters are given in Table 6.1. These parameters were used in equation 6.1 to calculate the LF at each of the QSO's redshift.

6.2 K-Corrections

To calculate the absolute magnitude at the magnitude limit of my sample at each QSO's redshift I need the K-correction at each redshift. I used equation 6.4 to determine the K-corrections for the galaxies in the VIDEO data,

$$K - \text{correction} = m - 5 \times \log_{10}(D_L) - 25 - M \qquad (6.4)$$

where m is the apparent magnitude in the K_s band, D_L is the luminosity distance at the QSOs redshift and M is the absolute magnitude in the K_s band. This was possible because each object in the VIDEO data has an associated absolute magnitude which was determined from the template fitting method. The absolute magnitude at the magnitude limit of the sample was calculated by finding the median K-correction for all of the galaxies within 1 Mpc of each QSOs position and within a given redshift of the QSO's redshift and setting $m = 23.5$; see equation 5.3. I also compared this method to the median K-corrections found using the whole galaxy sample for each QSO's redshift and both methods were consistent with each other. I chose to use the median K-corrections found using the galaxies which were in the QSOs' environments because this ensured that I was using the K-corrections for the galaxies that were found associated with the QSOs.

6.3 B_{gq} Calculations

To calculate the B_{gq} values for the given QSOs the following calculations were performed. Firstly the A_{gq} value is calculated, which is a measure of the excess

number of objects surrounding the QSOs compared to the expected background count:

$$A_{gq} = \left[\left(\frac{N_t}{N_b} \right) - 1 \right] \left(\frac{3 - \gamma}{2} \right) \theta^{\gamma - 1}, \tag{6.5}$$

where N_t is the number of galaxies contained within a given radius θ, which is the angular separation that corresponds to 1 Mpc at the QSOs redshift, and N_b is the expected background counts in the same radius. I chose 1 Mpc because the largest source overdensities were found within this distance from the central QSOs (Section 5.4). The central QSOs have all been excluded from the number counts. The value of the γ constant is taken to be $\gamma = 1.77$ and represents the slope of the two-point correlation function (Groth & Peebles 1977; Geach et al. 2007). Using A_{gq}, the spatial clustering amplitude B_{gq} is calculated as follows:

$$B_{gq} = \frac{A_{gq} N_g}{I_\gamma \Phi(z)} \left[\frac{D}{1 + z} \right]^{\gamma - 3}, \tag{6.6}$$

where N_g is the expected background count per steradian, D is the angular diameter distance of the QSOs and z is the QSO's redshift. The value of the I_γ constant is 3.77 when $\gamma = 1.77$ (McLure & Dunlop, 2001b). The value $\Phi(z)$ is the K-band galaxy luminosity function at the redshift of the QSOs, which is integrated from the bright end of the LF up to the absolute magnitude which corresponds to the apparent magnitude limit of the data (m = 23.5) at the redshift of the QSOs. The uncertainties on the B_{gq} values are calculated using the following equation:

$$\frac{\Delta B_{gq}}{B_{gq}} = \frac{[(N_t - N_b) + 1.3^2 N_b]^{1/2}}{(N_t - N_b)} \tag{6.7}$$

Table 6.2: The relation between the Abell classification and the spatial clustering amplitude.

Abell class	0	1	2	3	4	5
$B_{gq}(\mathrm{Mpc}^{1.77})$	300	700	1100	1500	1900	2300

which is used by McLure & Dunlop (2001b) and described by Yee & López-Cruz (1999). The conservative factor of 1.3^2 has been used by the quoted references to account for the fluctuation from the clustered nature of the background counts, in addition to the Poisson uncertainties from the background counts. I have also included it to ensure the uncertainty estimates are as conservative and realistic as possible.

6.3.1 B_{gq} and Abell classification

I have compared the B_{gq} spatial clustering amplitudes to the nominal boundary values for the Abell classification (Abell, 1958) in order to get a sense of the richness of the environments inhabited by the quasars. I have chosen to follow Yee & López-Cruz (1999) and McLure & Dunlop (2001b) to classify my cluster measurements, such that Abell class 0 clusters correspond to $B_{gq} > 300$ Mpc$^{1.77}$. Table 6.2 gives the adopted relation between spatial clustering amplitude and Abell classification.

6.3.2 B_{gq} for colour and ANNz selected QSOs

In Figure 6.1 the spatial clustering amplitudes for the colour and ANNz selected QSOs are shown and in Table 6.3 I show their mean and median values. A K-S test on their B_{gq} distributions does not find any significant difference between the two samples. This is interesting because in Chapter 5 their source overdensities were
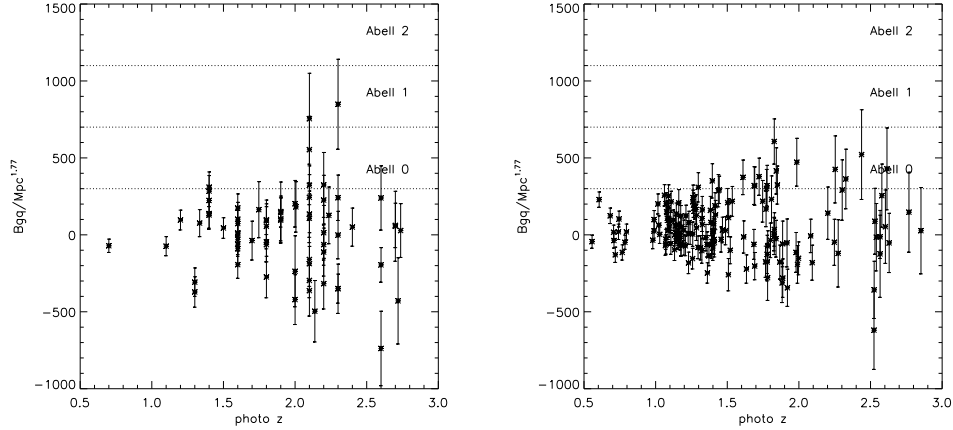
Figure 6.1: Left panel: Spatial clustering amplitude for the colour selected QSOs. Right panel: Spatial clustering amplitude for the ANNz selected QSOs.

found to be very different. The fact that the B_{gq} distributions are not different is consistent with the idea that it is simply the different redshift distribution of the samples that is responsible for this apparent difference (Section 5.5). The B_{gq} analysis enables me to compare samples at different redshifts because they are normalised to the galaxy luminosity function. Therefore, the colour-selected sample is still tracing dense environments of similar Abell classification as the ANNz selected QSOs sample.

Even though the two B_{gq} distributions are similar, the ANNz selected QSO sample is larger than the colour-selected QSO sample, and so, as in the previous Chapter, I use the ANNz selected QSOs sample to investigate whether there are correlations between the spatial clustering amplitudes and the redshift, radio type, and radio luminosity of the QSOs.

Table 6.3: Summary of the spatial clustering amplitude results for the ANNz and colour selected QSOs. N is the sample size and $\langle B_{gq} \rangle$ is the mean values.

QSOs selection	N	$\langle B_{gq} \rangle$	Median
ANNz	159	46 $\pm$14	20
Colour	68	14$\pm$33	55

Table 6.4: Summary of the spatial clustering amplitude results for the RLQs, RQQs, the whole sample and the conservative RLQ/RQQ samples. N is the sample size and $\langle B_{gq} \rangle$ is the mean values.

Type	N	$\langle B_{gq} \rangle$	Median
All	159	46 $\pm$14	20
RQQs	135	31$\pm$15	8
RLQs	24	131$\pm$31	101
Conservative RQQs	14	-39 $\pm$36	8
Conservative RLQs	21	143 $\pm$34	102
Galaxies	157	62 $\pm$12	32

6.3.3 B_{gq} and Radio type

In Section 5.6 I compared the stacked source overdensity for the RQQs and the RLQs and found that both samples exhibited significant source overdensities with the RLQs being in the densest regions. I can now use the spatial clustering amplitude to compare these two samples.

In Figure 6.2 the spatial clustering amplitudes of the RQQs and RLQs are shown. A K-S test on the two B_{gq} distributions shows that they have significantly different distributions at the 99.99 per cent confidence level. Following this I have performed a M-W test on the on the two B_{gq} distributions and find that their mean values are different at the 97 per cent confidence level. See Figure 6.3 for the B_{gq} distributions of the RLQs and the RQQs.

The mean and median values for the two QSOs samples and for the combined QSOs sample is shown in Table 6.4. These results support the idea that the RLQs

occupy denser regions when compared to the RQQs. The RLQs have a mean B_{gq} value of 131 ± 31 and a median value of 101, whilst the RQQs have a mean of 31 ± 15 and a median value of 8.

It is clear from Fig 6.2 that the RLQs occupy environments with large B_{gq} values, whilst the RQQs occupy environments with a range of different B_{gq} values. Both samples have QSOs which span Abell classes of Abell 0 and below. These results show that the RLQs occupy denser regions, as their mean and median B_{gq} values are consistently higher. This confirms previous results found in Chapter 5, and the implications of this result will be discussed in Section 6.5.

In addition to these results, I have also performed the same analysis on the conservative QSO sample, which is outlined in Section 5.6. This is a sample of radio-detected and non-radio detected QSOs that are confirmed RLQs and RQQs using the radio loudness criteria. The mean and median values for these conservative samples are shown in Table 6.4. I found that a K-S test showed the B_{gq} distributions of the conservative RQQ and RLQ sample were significantly different at the 97 per cent confidence level. A M-W test also showed that their means are different at the 99 per cent confidence level. This shows that the RLQ/RQQ definition is not producing this effect.

6.3.4 B_{GQ} and Absolute Magnitude

I also investigated whether the environmental density of the QSOs is linked to the absolute magnitude of the QSOs. In Figure 6.4 I show the absolute K_s-band magnitudes of each QSOs versus their B_{gq} values for < 1 Mpc. I tested each of these using a partial correlation analysis because there is a correlation between
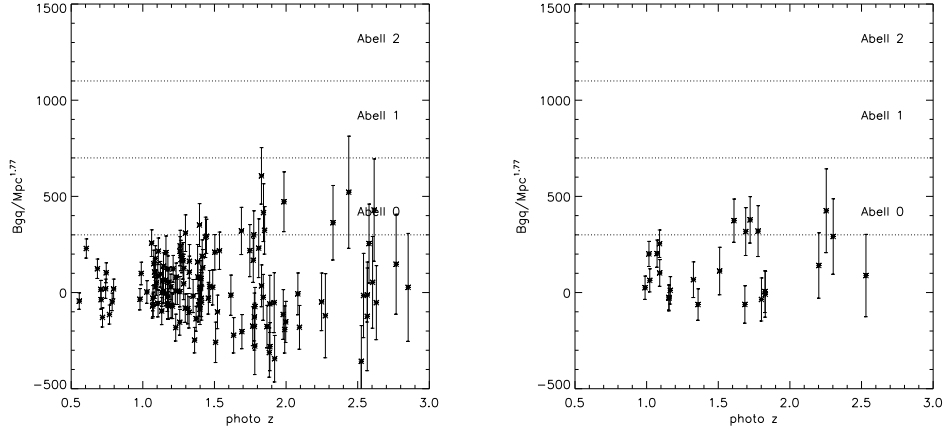
Figure 6.2: The spatial clustering amplitudes of the RQQs (left-hand panel) and the RLQs (right-hand panel) between $0.5 < z < 3.0$. The uncertainties ΔB_{gq} are described by equation 6.7.

redshift and absolute magnitude for the QSOs (see Fig 5.1 in Chapter 5). The partial correlation analysis can account for the correlation between redshift and absolute magnitude and determine whether there is a correlation between B_{gq} and redshift/absolute magnitude. The resulting coefficients and their probabilities are listed in Table 6.5.

The partial correlation coefficient does not show any significant correlation between clustering amplitude and redshift/absolute magnitude for either the RLQs or the RQQs. This is because the partial correlation removes the correlation between absolute magnitude and redshift, therefore I find that there is no correlation between clustering amplitude and absolute magnitude of the QSOs.
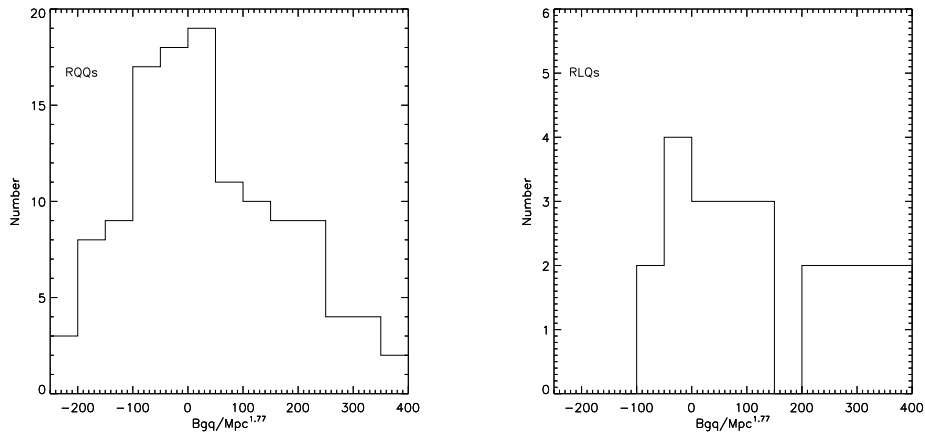
Figure 6.3: Histograms of the spatial clustering amplitudes of the RQQs (left-hand panel) and the RLQs (right-hand panel) between $0.5 < z < 3.0$.

Table 6.5: Table of the partial correlation coefficients (ρ) for correlations between the RLQs and RQQs absolute magnitude and redshift versus their B_{gq} values. The significances at which the null hypothesis of no correlation is rejected is also shown.

Type	ρ	Significance
B_{gq} vs K_s abs mag		
RLQs	0.14	$< 1\sigma$
RQQs	0.16	$< 2\sigma$
B_{gq} vs z		
RLQs	0.32	1.5σ
RQQs	-0.06	$< 1\sigma$

6.3.5 B_{gq} and Radio Luminosity

I have compared the B_{gq} values for the individual RLQs with their radio luminosities to see if there is any correlation between radio luminosity and environmental density.

195
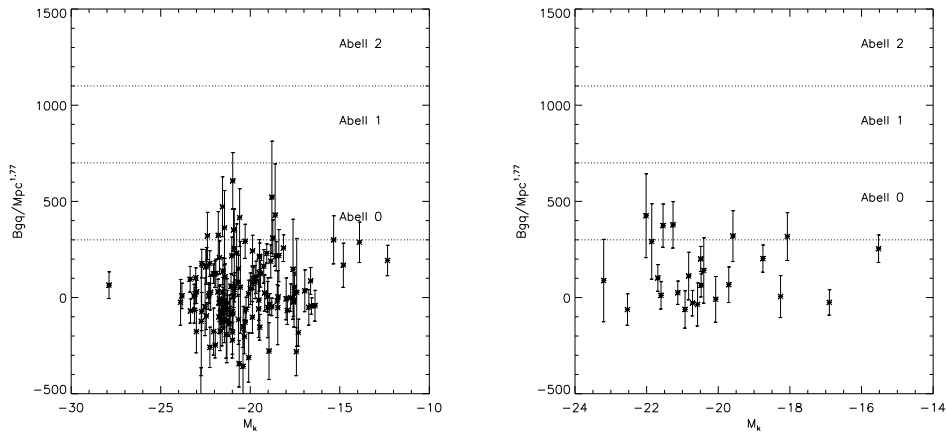
Figure 6.4: The spatial clustering amplitudes of the RQQs (left-hand panel) and the RLQs (right-hand panel) between $0.5 < z < 3.0$ versus their K_s-band absolute magnitudes. The uncertainties ΔB_{gq} are described by equation 6.7.

In Figure 6.5 the 1.4 GHz radio luminosities for the RLQs are plotted against the B_{gq} values. From this it is clear that there is no significant correlation between environmental density and radio luminosity. A Spearman rank correlation gives a coefficient of 0.33 with a significance of 89 per cent; this confirms that there is no strong evidence for a correlation between the radio luminosity of the RLQs and the spatial clustering density.

6.3.6 B_{gq} and redshift

I have compared the B_{gq} across the redshift distribution to investigate whether they change as a function of redshift. I have split up the B_{gq} distribution into two samples, one where $0.5 < z < 1.5$ and the other where $z \geq 1.5$ which compared the
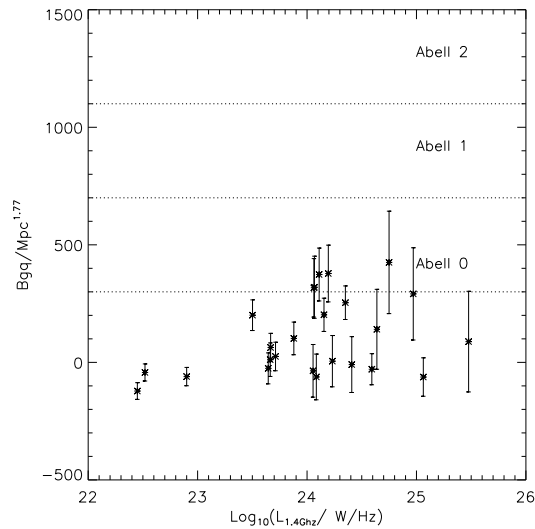
Figure 6.5: The spatial clustering amplitudes of the RLQs versus their 1.4GHz radio luminosities. The uncertainties ΔB_{gq} are described by equation 6.7.

mean values in these two redshift distributions. I found no significant differences between the two samples, the lower redshift sample has a mean 47 ± 11 and the highest 44 ± 32. The uncertainties are largest for the highest redshift QSOs, this is due to the uncertainty in the photometric redshifts. Therefore, I do not find, on average, more clusters at higher redshifts compared to the lower redshifts.

6.4   Comparison to Galaxy Samples

To compare my density results for the QSOs' environments to dense regions around galaxies without QSOs I created galaxy comparison samples and investi-

gated their environmental density, as described in Section 5.8.

In Figure 6.6 I show the B_{gq} values for the sample of bright galaxies matched to the quasar redshifts, which have been previously shown to reside in overdensities (Fig 5.21). This figure shows that the brightest galaxies reside in Abell classes of 1 and below, and have a mean of 62 ± 12 and a median of 32. In figure 6.7 I show the number of galaxies found in bin sizes of $B_{gq} = 50$; many are found around 0 and below but some have spatial clustering amplitudes $B_{gq} > 300$. This means that some of the bright galaxies are found in Abell classes of 0 and above.

In Table 6.4 I show the mean B_{gq} values for the galaxy sample. The galaxy sample is approximately 2σ above the mean of the RQQ sample and approximately 2σ below the mean of the RLQ sample. I will discuss these results further in Section 6.5.

6.5   Discussion

In this section I discuss the results found for the RLQ, RQQ and galaxy samples and possible explanations for them.

6.5.1   Comparison to the literature - clustering amplitude

To put my results in context I have compared my results for the spatial clustering amplitude (B_{gq}) for both the QSOs and galaxies to results found in the literature. Due to large scatter in the individual B_{gq} values for the QSO/galaxy samples I have compared the mean and median values of the RLQs, RQQs and galaxies to the literature. It is important to note that this large scatter means that many QSOs do not appear to reside in overdense regions even though there is
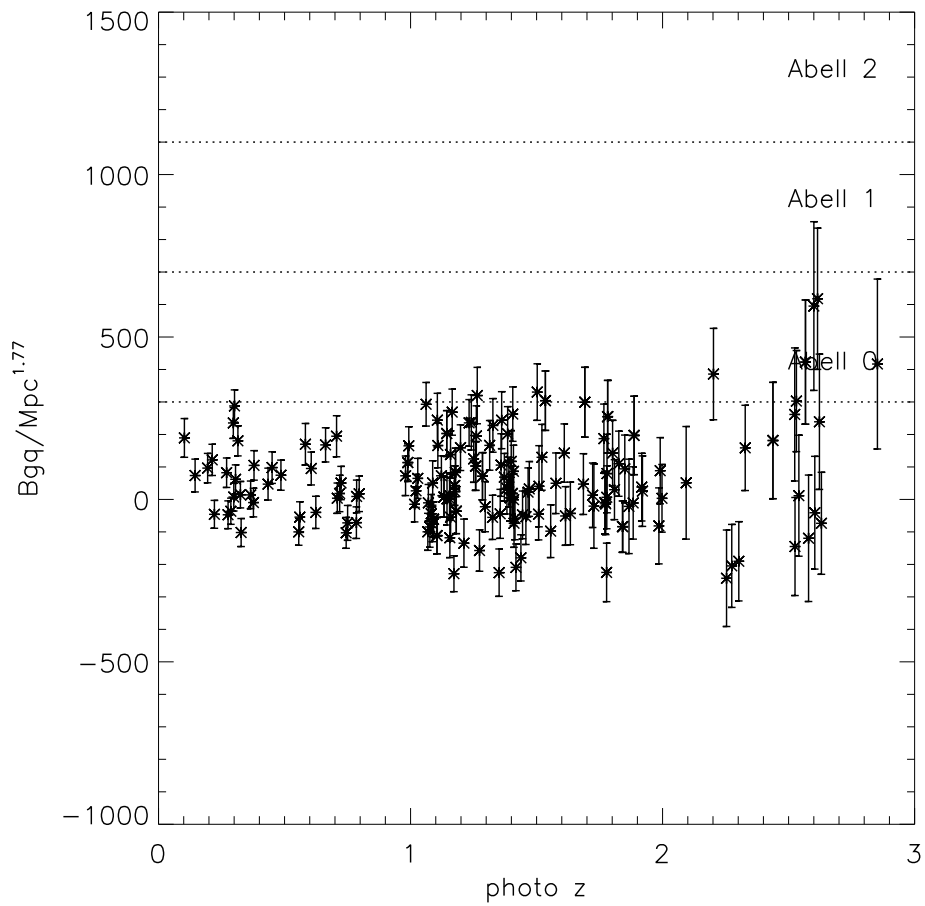
Figure 6.6: The spatial clustering amplitudes of the brightest galaxy sample. The uncertainties ΔB_{gq} are described by equation 6.7.
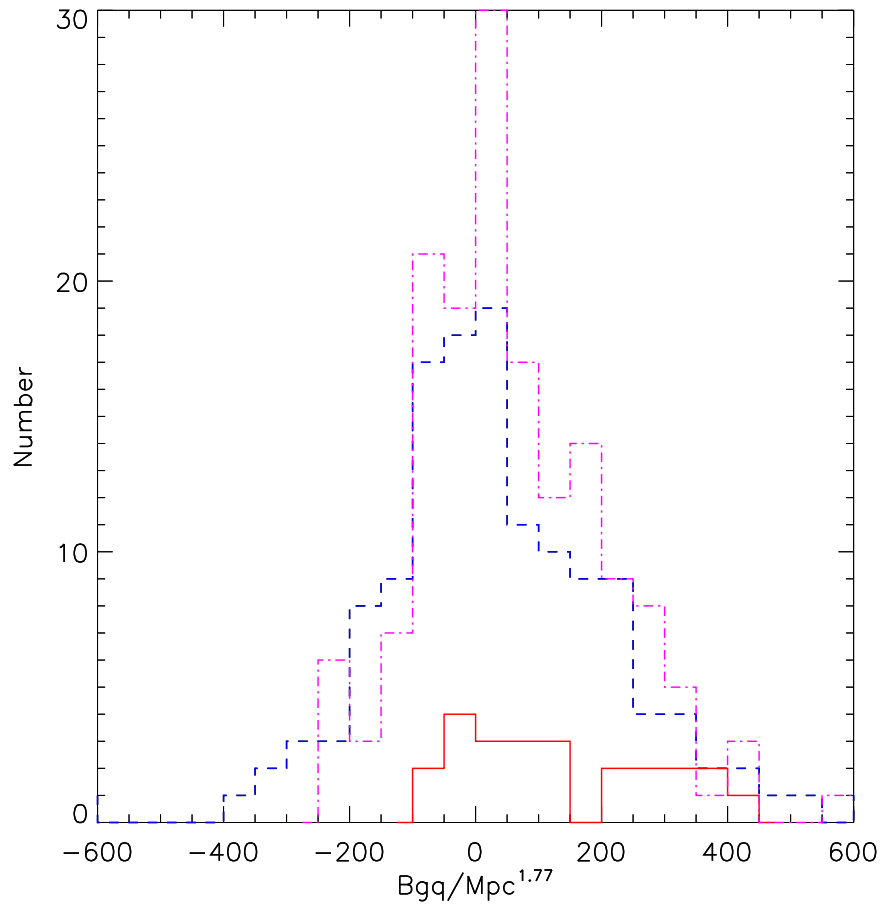
Figure 6.7: The spatial clustering amplitudes of the brightest galaxy sample (magenta dashed-dotted line), the RQQ sample (blue dashed line) and the RLQ sample (red solid line).

an overall overdensity. Similar to what was seen in Chapter 3, it is possible that the mean overdensity is strongly influences by a small number of objects in rich environments. However, in what follows I consider the mean overdensity as it provides the most robust measurement available to me.

I find that the RQQ sample has a mean B_{gq} value of $B_{gq} = 31 \pm 15$ Mpc$^{1.77}$ with a median of 8, while the RLQ sample has a mean of $B_{gq} = 131 \pm 31$ Mpc$^{1.77}$ and a median of 101. The galaxy sample has a mean of $B_{gq} = 62 \pm 12$ Mpc$^{1.77}$ and a median of 32.

I first compare these values to that of McLure & Dunlop (2001b), whose AGN sample consists of 44 objects at $z \sim 0.2$. They find that their RG sample is the most overdense at a mean of $B_{gq} = 575 \pm 165$ Mpc$^{1.77}$, the RLQs have a mean of $B_{gq} = 267 \pm 51$ Mpc$^{1.77}$ and the RQQs have a mean of $B_{gq} = 326 \pm 94$ Mpc$^{1.77}$. My results are consistently lower compared to these values. A possible reason for the lower clustering amplitudes could be that the QSOs in my sample are found at higher redshifts compared to the other sample, and therefore wouldn't be residing in the most overdense clusters which are found at low redshifts. They are also a lot less luminous than the QSO sample in McLure & Dunlop (2001b) and therefore is not expected to be found in the same environments.

The B_{gq} analysis allows me to compare my clustering amplitudes to the Abell cluster classification. At low redshifts ($z = 0.2$) McLure & Dunlop (2001b) find that there is no significant difference between the environments of radio-loud and radio-quiet QSOs, with both typically inhabiting environments as rich as Abell class 0. I do find differences between the average clustering of the RLQ and RQQs samples but overall they both occupy environments as rich as Abell class 0, consistent with the results of McLure & Dunlop (2001b). Wold et al. (2001) also

find that on average the RQQs prefer poorer clusters of Abell class 0 rather than richer environments. Their RQQ sample has a mean of $B_{gq} = 210 \pm 82$ Mpc$^{1.77}$ and their RLQ sample has a mean of $B_{gq} = 213 \pm 66$ Mpc$^{1.77}$. Their study is at intermediate redshifts ($0.5 < z < 0.8$) and they find the environments of RQQs and RLQs were indistinguishable, concluding that the process that determines the radio-loudness of a quasar is not dependent on the Mpc scale environment but may be caused by the central regions of the host galaxy.

6.5.2 Comparison to the literature - radio-loud and radio-quiet

In my sample, on average, the RLQs reside in denser environments compared to the RQQs, which is in agreement with previous results by Falder et al. (2010). This may point to the idea that different radio-loud QSOs prefer different types of environments. Possibly at higher redshifts ($z > 0.5$) the Mpc scale environments do have some influence on whether a QSO is radio-loud. Recently, Ramos Almeida et al. (2013) found significant differences between the angular clustering amplitudes of radio galaxies, radio-quiet type-2 quasars and a control sample of quiescent early-type galaxies all at intermediate redshifts ($0.05 < z < 0.7$). They found that their radio galaxies were in denser environments than the quiescent galaxy population with a significance at the 3σ level. Kauffmann et al. (2008) have also found that their radio selected AGN sample reside in denser environments compared to their RQQ sample. They propose that the observed differences in environments is related to the type of gas accretion in the AGN, in the sense that radio AGN are found in denser environments and are primarily fuelled by

hot gas accretion, while optical AGN are found in less dense environments and cold gas accretion is the main source of fuel. The difference in the environmental density in this model would reflect the transition between cold gas accretion and hot gas accretion in dark matter halo mass of $\sim 10^{12}$ M$_\odot$ (Birnboim & Dekel 2003; Kereš et al. 2005; Croton et al. 2006). However, these are low redshift and low luminosity radio-detected AGN and so are difficult to directly compare to my high redshift radio-loud QSO sample.

My results are different to what was found in previous studies by McLure & Dunlop (2001b) and Wold et al. (2001). However, they only studied QSOs at low redshifts ($z < 0.8$) and have smaller sample of QSOs compared to my QSO sample; 21 RLQs and 20 RQQs (Wold et al., 2001), and 10 RGs, 10 RLQs and 13 RQQs (McLure & Dunlop, 2001b). Therefore, any differences between the environments of the RLQs and RQQs might be found using larger samples at higher redshifts.

6.5.3 Comparison with control sample of galaxies

I have compared the B$_{\mathrm{gq}}$ distributions of the galaxy control sample and the RLQ and RQQ samples. I found that, on average, the galaxy control sample are found in denser environments than the RQQ sample but not as dense environments as the RLQ sample. This is interesting because at low redshifts ($z < 0.4$), Serber et al. (2006) found that their spectroscopic sample of QSOs from SDSS, on scales from 25 kpc to 1 Mpc, are located in denser environments than their spectroscopic galaxy control sample. However, the radio loudness of their QSO sample is not determined, so it is difficult to directly compare their results to mine, but their

QSO and galaxy samples are matched in redshift so it does imply that QSOs are good tracers of dense regions at low redshifts, as well as high redshifts which my results show.

The RLQs seem to be associated with the most dense environments and thus are good tracers of the densest regions in the Universe. This is similar to what has been previously found by Ramos Almeida et al. (2013). They found that the environments between their RG sample and their galaxy control sample were different at a significance at the 3σ level. These results point to the idea that the high density environments of RLQs might be responsible for the radio jet production. Reasons for this will be discussed in the following sections.

6.5.4   Environment and radio luminosity

I find that both the density analysis in Chapter 5 and the B_{gq} spatial clustering amplitude shows that the RLQ sample resides in denser environments, on average, compared to the RQQ sample.

One possible reason for these differences could be that the radio-loud QSOs are influencing their environmental density, but this is implausible because the radio jets would have to influence galaxy formation on Mpc scales. It is more likely that the denser environments cause the QSOs to become more radio-loud. This could happen through the process of jet confinement, in which denser environments enhance synchrotron losses from radio jets, thereby making them brighter (Barthel & Arnaud, 1996). However, I do not find any significant correlation between radio luminosity and the B_{gq} values; if jet confinement were the sole

explanation for the observed differences between the AGN samples then I would expect there to be a correlation since the densest environments produce the most radio luminous AGN.

However, other studies such as those of Falder et al. (2010) and Donoso et al. (2010), have found some evidence for a correlation between radio luminosity and source overdensity, although this is only the case for the very radio luminous QSOs ($Log_{10}/WHz^{-1}sr^{-1} > 26$) in Falder et al. (2010) and for the RLAGN up to $10^{25.5}$ WHz^{-1} in Donoso et al. (2010). This suggests that there is not a clear picture whether radio luminosity does correlate with environmental density. It may be that a larger sample of VIDEO QSOs including more luminous radio-loud objects would also show this correlation.

6.5.5 Environment and black hole mass

Another possible reason for the environmental density differences between the RLQs and RQQs could be that they have black holes of different masses. Black hole masses have been found to be larger for RLQs, which typically have black hole masses $> 10^8$ M$_\odot$, whilst the RQQs have black hole masses $> 10^7$ M$_\odot$ (McLure & Jarvis, 2004). This implies that the RLQs reside in the largest dark matter halos, which would be found in the densest environments (Di Matteo et al., 2005), since the largest black holes would be found in the brightest galaxies (Kaspi et al., 2000). However, my sample of RLQs and RQQs are matched in absolute magnitude, a K-S test showed no significant differences between the absolute magnitude distributions. If the two samples had any significant differences between their black hole masses I would expect them to have significant

differences in their absolute magnitudes, assuming that the accretion is at a constant fraction of the Eddington luminosity. Falder et al. (2010) found using black hole (M_{BH}) measurements for their AGN sample that there were no significant differences between the black hole masses between the radio-loud and radio-quiet QSOs and so concluded that black hole mass could not explain why the RL/RQ samples resided in different density environments.

However, it could be that black hole needs to be more massive to produce a RLQ ($> 10^8$ $M_{\odot}$) but that there is more of a spread of black hole masses for the RQQs (Best et al. 2005; Baldi & Capetti 2010; Chiaberge & Marconi 2011). So there wouldn't be a clear divide between the black hole masses between RLQ and RQQs, which I find in my sample. This implies that the method of producing a RLQ is not as straight forward as them having larger black hole masses compared to the RQQs.

6.5.6 Environment and black hole spin

An alternative theory is that denser environments possibly have more galaxy mergers compared to the field which would produce a rapidly spinning SMBHs and thus provide more capability of powering a radio jet (Wilson & Colbert 1995; Sikora et al. 2007; Tchekhovskoy et al. 2010). Using semi-analytic models, Fanidakis et al. (2011) found that massive BHs ($M_{BH} > 5 \times 10^8$ $M_{\odot}$) that are hosted by giant elliptical galaxies are rapidly spinning. The most massive ellipticals would be found in the largest galaxy clusters and according to Fanidakis et al. (2011) these would have the largest black hole spin. This would produce more power for the radio jets and therefore they would be more radio-loud. This

is consistent with the fact that I find the most radio loud AGN in the densest environments. Chiaberge & Marconi (2011) found that RLQs are possibly produced by a combination of higher black hole mass ($> 10^8$ M$_\odot$) and higher black hole spin. Even though I don't find any evidence for a difference in black hole masses between my RLQ and RQQ samples, they could still reside in large black hole masses, since there isn't a clear divide between the black hole mass between RQQs and RLQs.

The dichotomy between the RLQ and RQQ could then be explained by the RLQs having a higher black hole spin. This could be explained by the RLQs having different merger histories compared to the RQQs. Possible reasons for the increased spin for the RLQs could be that they have more accretion (Volonteri et al., 2007b), although it probably only leads to moderate spin values (King et al., 2008). More likely that the higher spin values could be due to two similar sized black holes merging, which would be found in dry mergers (early type galaxy mergers) (Chiaberge & Marconi, 2011).

6.6   Summary

To be able to compare QSO environments that span a large range of redshifts I used the spatial clustering amplitude (B$_{gq}$). From this I was able to compare the QSOs' redshifts, K_s-band absolute magnitudes, radio luminosities and radio types with their B$_{gq}$ densities. The main conclusions are as follows.

1. I find that the RQQs and the RLQs have different B$_{gq}$ distributions at the 99.99 per cent level using a K-S test and a significance of 97 per cent difference in their median values after using a M-W test. The RLQs occupy

denser environments than the RQQs. This implies that the environments might be influencing the radio loudness of the QSOs.

2. When comparing the K_s-band absolute magnitude of the RLQs and the RQQs with their B_{gq} values I find that there is no correlation between these for either sample.

3. I have also compared the 1.4 GHz radio luminosities of the RLQs to their B_{gq} value, in order to investigate whether the most radio luminous radio-loud quasars occupy the densest environments; however, I find no significant correlation between these. This shows that jet confinement is not the reason behind the RLQ/RQQ dichotomy.

4. The mean of the B_{gq} values for the QSOs is 46 ± 14 with a median of 20 whilst the brightest galaxy sample has a mean of 31 ± 12 and a median of 10. Thus QSOs and the brightest galaxies are both good tracers of denser regions. However, the best tracers of dense regions are the RLQs that have a mean value of 131 ± 31 with a median of 101. This could be due to the RLQs having a higher black hole spin which would be more likely to be found in denser environments.

Chapter 7

Summary and Future Work

In this thesis I have presented the work that I have done over the past 3.5 years. This work has been focused on the environments of AGN and in particular the galaxies and the star formation in these environments. I have used two samples of AGN, one using observations from Spitzer and the other using data from the VIDEO survey. In this Chapter I summarise my main findings, in particular, the links between AGN, star formation and their environments in Section 7.1. I discuss possible future work in Section 7.2.

7.1   Summary

I have performed a density analysis on both the Spitzer observations of a sample of 169 AGN and a sample of 274 QSOs selected from VIDEO to investigate whether the AGN preferentially reside in overdense environments compared to the background level and whether the overdensities vary depending on the properties of the AGN, such as radio luminosity. I will discuss the main findings for the

Spitzer sample followed by the results using the VIDEO sample.

In Chapter 3, I used a density analysis to count the number of 24μm sources in the environments of 169 AGN (the sample of Falder et al. (2010)), which are split up into RGs, RLQs and RQQs. This AGN sample was chosen to span a narrow redshift range of $0.9 < z < 1.1$ which allows for a comparison between AGN environments at a single epoch. This avoids introducing a correction between luminosity and redshift. This sample was also selected to span 5 magnitudes in quasar optical luminosity, which allows for a comparison between the environmental densities of QSOs of different magnitudes. The RLQs and RQQs were selected in identical ways to ensure that there were no biases associated with the radio selection.

Falder et al. (2010) found that these AGN resided in 3.6μm overdense regions and that radio-loud AGN inhabited systematically denser environments. My work used 24μm data, which is sensitive to star formation, instead of 3.6μm, which is sensitive to more evolved stellar populations. I found that there is no significant overdensity of star-forming galaxies compared to the field. This might imply that there are processes in the AGN environments that are suppressing the star formation, such as feedback processes (Bower et al., 2006; Croton et al., 2006), or processes which are found in denser environments, such as galaxy interactions (Gunn & Gott, 1972; Larson et al., 1980; Moore et al., 1996; Oemler, 1976). However, it is difficult to determine whether any of these processes is affecting the level of star formation due to the different sensitivity limits of the 3.6μm and 24μm data. More sensitive observations are required to test this further.

As an extension to the density analysis for the Spitzer AGN sample I do find tentatively that the distribution of S(24μm/3.6μm) galaxy colours within the

vicinity of the RGs are different compared to the field and the QSO environments. The S(24μm/3.6μm) galaxy colours in the RG environments are drawn from different populations at a 3σ confidence level, when compared to the background SWIRE colours. They are also drawn from different populations at a 2.5σ confidence level, when compared to the galaxy colours detected around the QSOs. My RG sample consists of mainly HERGs, rather than LERGs, which are preferentially found in rich environments and consist of older stellar populations rather than star-forming galaxies (Hardcastle, 2004; Hardcastle et al., 2012). Therefore, the optical class of the RGs does not explain why they might be found in environments with older populations.

I next investigated the environments around a further sample of AGN in the VIDEO data using a similar technique. I found this sample using an artificial neural network which was described in detail in Chapter 4. In this Chapter I explained how I trained the artificial neural network using training data from VVDS, VIKING, SDSS and 2SLAQ, consisting of 1392 spectroscopically determined QSOs with spectroscopic redshifts and data in optical and near-infrared bands. I was able to define what is more likely a QSO and what is more likely a galaxy using the neural network which classifies each object. Using the training data I was able to determine that the efficiency of the ANNz classification was 95 per cent. I was able to classify 274 QSOs in the VIDEO data with $K_s < 21$.

In Chapter 4 I also compared the ANNz QSOs selection method to a colour selection method. I found that ANNz is capable of detecting ~ 80 per cent of the colour selected QSOs at $K_s = 21$. The colour selection method was able to identify fainter QSO candidates: however, it only classified 88 QSOs in the VIDEO data, whilst the ANNz selection method classified 274. Both of these

methods provide me with QSO samples at high redshifts, which I could then use to investigate the source overdensity in their environments.

In Chapter 5 I performed a density analysis on the ANNz QSOs and the colour-selected QSOs. Firstly, I found a significant overdensity of 3.36±1.140 galaxies Mpc^{-2} within 0.6 Mpc of the stacked ANNz QSOs at a significance of $\sim 3\sigma$. I was able to split the QSO sample up into radio-loud and radio-quiet using the VLA radio survey of Bondi et al. (2003) to investigate whether the RLQs resided in more overdense environments compared to the RQQs. I find a difference in source overdensity between the RLQs and the RQQs. The RLQs reside in overdensities of 10.63 ± 2.85 sources Mpc^{-2} within 0.6 Mpc of the stacked RLQs, compared to the RQQs, which reside in overdensities of 2.62 ± 1.243 sources Mpc^{-2}. The redshift distribution of the RLQ and RQQ samples are indistinguishable implying that this is a real physical difference. This is similar to what previous studies have found (Falder et al., 2010; Mayo et al., 2012; Wylezalek et al., 2013): radio-loud AGN reside in richer environments. I performed a similar analysis on the colour-selected QSOs and I did not find any significant overdensities. This might be due to the differences in redshift distributions of the colour-selected and ANNz-selected QSOs. In addition, the colour-selected sample is a lot smaller, so it may be that more data are needed to detect a significant overdensity in their environments.

In Chapter 6 I compared my density results to another density measurement, the spatial clustering amplitude ($\mathrm{B_{gq}}$) and found that the environments of the RLQs and the RQQs are statistically different. The RLQs and the RQQs have different $\mathrm{B_{GQ}}$ distributions at the 99.99 per cent level using a K-S test and a significance of 97 per cent difference in their median values after using a M-W

test. This provides further evidence that the environments of radio-loud AGN are different from those of the radio-quiet AGN.

Some earlier authors have failed to find differences between the environments of radio-loud and radio-quiet QSOs (McLure & Dunlop 2001b;Wold et al. 2001). However, these studies have a small sample of QSOs. I select both the RLQs and RQQs using the same method (ANNz) and have a larger sample of QSOs than these studies. These studies are also only investigating the environments of QSOs at low redshifts ($z < 0.8$), while my QSOs sample is at high redshifts ($0.5 < z < 3$). Older studies, such as Yee & Green (1984) and Ellingson et al. (1991) found that RLQs preferentially inhabited richer environments and recent studies, such as Donoso et al. (2010); Falder et al. (2010) and Ramos Almeida et al. (2013) have found significant differences between the environments of radio-loud and radio-quiet QSOs. Given my results and those of these authors previously, I conclude that the environments of RLQs and RQQs are different and this should be considered when investigating the mechanisms responsible for the differences seen between the different types of AGN.

An interpretation of these results could be that the denser environments are influencing the radio-loudness of an AGN through the process of jet confinement (Barthel & Arnaud, 1996); however, this is unlikely because I find no correlation between radio luminosity of the QSOs and environmental density, whereas this model would predict that the most radio-luminous objects would inhabit the densest environments. Another possibility could be that there is a difference between the black hole mass of the two samples. However, I find that they match in absolute magnitude; if their black hole masses were significantly different then their magnitudes would also be different, assuming that the accretion is at a

constant fraction of the Eddington luminosity. A final possible explanation could be that radio-loudness is related to black hole spin. The denser environments would have more galaxy mergers, which could produce rapidly spinning SMBHs and thus provide more capability of powering a radio jet (Wilson & Colbert 1995; Sikora et al. 2007). Such a model is difficult to test observationally.

I have extended the work on the ANNz QSOs by investigating the types of galaxies found in their environments, comparing to the field. I do not find any significant differences between the type of galaxies in the field and in the environment of either class of AGN. I might expect to see the level of star formation suppressed in denser environments through processes such as galaxy interactions and ram pressure stripping (Gunn & Gott 1972; Oemler 1976; Larson et al. 1980; Moore et al. 1996). However, I do not detect these processes in the environments of high redshift QSOs or galaxies. This may suggest that these processes have still yet to have an effect at high redshifts. However, due to limitations with the statistics I am unable to obtain conclusive results. Therefore, a larger sample is needed to improve upon the statistics which will be able to investigate the environments further.

I believe this Ph.D. has contributed to the field of extragalactic astronomy in the following ways:

- *Are AGN found to trace dense environments at high redshifts ($z > 1$)?*

  I have found that they do trace dense environments at high redshifts. However, bright galaxies are also good tracers of dense environments.

- *Do radio-loud AGN preferentially reside in dense environments?*

  I have found that radio-loud AGN do reside in dense environments when

compared to radio-quiet AGN: radio-loud AGN trace the densest environments I was able to detect in my study, significantly richer than those of either RQQ or bright galaxies. However, the processes responsible for these differences are still unknown, with a difference in black hole spin being one plausible explanation.

- *Does star formation evolve differently in high-redshift cluster environments (Stevens et al. 2010; Mayo et al. 2012) compared to the field?*

  I have not found any concrete evidence for a difference in star formation rates in high-redshift cluster environments compared to the field. The processes that suppress star formation in dense environments have not been found in my sample. This is possibly due to differences between dense environments found at high redshifts compared to those found at low redshifts, such as ram pressure stripping found in clusters at low redshifts (see Section 5.9).

- *Do AGN have any impact on star formation in their large scale-environments through feedback processes (Springel et al. 2005b; Hopkins et al. 2006)?*

  I obtained evidence for this, in that the radio galaxies in the Spitzer sample had marginally different galaxy colours in their environments compared to the field and the QSO samples. However, I find no evidence for a difference in the number of starburst galaxies in the environments of the VIDEO QSO sample compared to the field.

7.2 Future work

In this section I describe possible future work that could improve upon and extend my research.

An extension to Chapter 3 would be to use more robust observations of the $z \sim 1$ AGN sample to be able to probe down to lower levels of star formation and so to be able to compare the level of star formation in the AGN environments. This is currently possible because the $z \sim 1$ AGN sample has been observed using the FIR instruments on the *Herschel* space telescope.

Further work on Chapter 4 can be done to verify the ANNz selection method. This can be done by obtaining spectroscopic verification of the QSOs detected and determining their spectroscopic redshifts. This would confirm the ANNz selection method and determine the actual amount of contamination from galaxies.

The next step for the VIDEO project is to extend the density analysis, which was only performed on the VIDEO-XMM3 field, to all of the fields in VIDEO to investigate the environments of AGN further and provide the larger sample size that is needed. The photometric redshifts used in the project incorporate uncertainties in the work which spectroscopic redshift will improve upon. Therefore, obtaining spectroscopic redshifts for the galaxies in the vicinity of the QSOs would provide certainty that they are associated with the QSOs. This could be done on the individual environments of the most apparently overdense QSOs to reduce the number of galaxies needing spectroscopic redshifts.

Future telescopes, such as the European Extremely Large Telescope (E-ELT), will provide deeper observations which will enable astronomers to investigate the high redshift Universe in more detail. The E-ELT will be able to obtain star-

formation rates, stellar masses and ages which are only available for low redshift galaxies at the moment. This will enable us to investigate the processes that govern star formation and the relationship between AGN and their environments in more detail than previous telescopes. The James Webb Space Telescope (JWST), which will be the successor to the Spitzer Telescope, will provide astronomers with observations in the infra-red at unprecedented resolution and sensitivity. This telescope would provide observations which would improve upon the results in this thesis because they would be able to investigate the morphologies of the galaxies in the QSOs' environments and determine whether they evolve over cosmic time.

In the future these observations will be important to be able to link the observable Universe to cosmological theory. We will be able to find out the number density of clusters and how it varies with redshift, and to determine the number of AGN found in clusters and how they vary with density, with surveys that are large enough to provide statistically significant number of objects. Future data in the VIDEO survey and others will enable us to compare observations with current models, such as those of Angulo et al. (2012); Fanidakis et al. (2013), as a function of redshift. This is difficult to do because we do not have enough detected clusters throughout the redshift range.

References

Abazajian, K. N., Adelman-McCarthy, J. K., Agüeros, M. A., et al. 2009, ApJS, 182, 543 47, 48, 111

Abell, G. O. 1958, ApJS, 3, 211 31, 191

Adelman-McCarthy, J. K., Agüeros, M. A., Allam, S. S., et al. 2008, ApJS, 175, 297 105

Agertz, O., Teyssier, R., & Moore, B. 2011, MNRAS, 410, 1391 25

Alonso-Herrero, A., Rieke, M. J., Rieke, G. H., & Shields, J. C. 2000, ApJ, 530, 688 11

Angulo, R. E., Springel, V., White, S. D. M., et al. 2012, MNRAS, 425, 2722 31, 38, 181, 218

Antonucci, R. 1993, ARA&A, 31, 473 4, 13, 16, 18, 20

Archibald, E. N., Dunlop, J. S., Hughes, D. H., et al. 2001, MNRAS, 323, 417 12

Arnouts, S., Walcher, C. J., Le Fèvre, O., et al. 2007, A&A, 476, 137 146, 171

Baade, W. & Minkowski, R. 1954, The Observatory, 74, 130 2

Baldi, R. D. & Capetti, A. 2010, A&A, 519, A48 207

Baldry, I. K., Robotham, A. S. G., Hill, D. T., et al. 2010, MNRAS, 404, 86 121, 124, 139

Baldwin, J. A., Phillips, M. M., & Terlevich, R. 1981, PASP, 93, 5 12

Balogh, M. L., Wilman, D., Henderson, R. D. E., et al. 2007, MNRAS, 374, 1169 143

Banerji, M., Lahav, O., Lintott, C. J., et al. 2010, MNRAS, 406, 342 106

Barnes, J. E. & Hernquist, L. 1996, ApJ, 471, 115 28

Barthel, P. D. & Arnaud, K. A. 1996, MNRAS, 283, L45 36, 206, 214

Baugh, C. M. 2006, Reports on Progress in Physics, 69, 3101 27

Baugh, C. M., Cole, S., Frenk, C. S., & Lacey, C. G. 1998, ApJ, 498, 504 27

Baugh, C. M., Lacey, C. G., Frenk, C. S., et al. 2005, MNRAS, 356, 1191 23, 26

Becker, R. H., White, R. L., & Helfand, D. J. 1995, ApJ, 450, 559 53

Bekki, K. 2009, MNRAS, 399, 2221 184

Benson, A. J. & Bower, R. 2010, MNRAS, 405, 1573 25

Bentz, M. C., Peterson, B. M., Netzer, H., Pogge, R. W., & Vestergaard, M. 2009, ApJ, 697, 160 5

Bertin, E. & Arnouts, S. 1996, A&AS, 117, 393 42, 69

Bertone, G. & Merritt, D. 2005, Modern Physics Letters A, 20, 1021 21

Best, P. N., Kauffmann, G., Heckman, T. M., et al. 2005, MNRAS, 362, 25 207

Best, P. N., Lehnert, M. D., Miley, G. K., & Röttgering, H. J. A. 2003, MNRAS, 343, 1 34

Best, P. N., Longair, M. S., & Rottgering, H. J. A. 1996, MNRAS, 280, L9 54

Birnboim, Y. & Dekel, A. 2003, MNRAS, 345, 349 204

Black, A. R. S., Baum, S. A., Leahy, J. P., et al. 1992, MNRAS, 256, 186 15

Blandford, R. D. & McKee, C. F. 1982, ApJ, 255, 419 5

Blanton, M. R., Hogg, D. W., Bahcall, N. A., et al. 2003, ApJ, 592, 819 27

Bondi, M., Ciliegi, P., Zamorani, G., et al. 2003, A&A, 403, 857 45, 48, 49, 164, 213

Borgani, S. & Guzzo, L. 2001, Nature, 409, 39 21

Bower, R. G., Benson, A. J., Malbon, R., et al. 2006, MNRAS, 370, 645 27, 30, 184, 211

Bower, R. G., Lucey, J. R., & Ellis, R. S. 1992, MNRAS, 254, 601 141

Boyle, B. J., Shanks, T., Croom, S. M., et al. 2000, MNRAS, 317, 1014 105

Briel, U. G., Henry, J. P., & Boehringer, H. 1992, A&A, 259, L31 31

Brüggen, M. & Kaiser, C. R. 2002, Nature, 418, 301 27, 184

Burbidge, G. R., Burbidge, E. M., & Sandage, A. R. 1963, Reviews of Modern Physics, 35, 947 2

Burtscher, L., Meisenheimer, K., Tristram, K. R. W., et al. 2013, A&A, 558, A149 4

Butcher, H. & Oemler, Jr., A. 1984, ApJ, 285, 426 32, 184

Buttiglione, S., Capetti, A., Celotti, A., et al. 2010, A&A, 509, A6 12

Calzetta, E. & Hu, B. L. 1995, Phys. Rev. D, 52, 6770 24

Chandrasekhar, S. 1943, ApJ, 97, 255 26

Charlton, J. & Churchill, C. 2000, Quasistellar Objects: Intervening Absorption Lines, ed. P. Murdin 12

Chary, R. & Elbaz, D. 2001, ApJ, 556, 562 92, 96

Chen, K. & Halpern, J. P. 1989, ApJ, 344, 115 4

Chen, Y.-M., Kauffmann, G., Tremonti, C. A., et al. 2012, MNRAS, 421, 314 51

Chiaberge, M., Capetti, A., & Celotti, A. 1999, A&A, 349, 77 14

Chiaberge, M. & Marconi, A. 2011, MNRAS, 416, 917 207, 208

Chiu, K., Richards, G. T., Hewett, P. C., & Maddox, N. 2007, MNRAS, 375, 1180 128, 132, 139

Churazov, E., Sazonov, S., Sunyaev, R., et al. 2005, MNRAS, 363, L91 30

Churazov, E., Sunyaev, R., Forman, W., & Böhringer, H. 2002, MNRAS, 332, 729 27, 184

Cirasuolo, M., Celotti, A., Magliocchetti, M., & Danese, L. 2003, MNRAS, 346, 447 15

Cirasuolo, M., McLure, R. J., Dunlop, J. S., et al. 2010, MNRAS, 401, 1166 188

Clowe, D., Bradač, M., Gonzalez, A. H., et al. 2006, ApJ, 648, L109 21

Cole, S., Aragon-Salamanca, A., Frenk, C. S., Navarro, J. F., & Zepf, S. E. 1994, MNRAS, 271, 781 25

Collister, A. A. & Lahav, O. 2004, PASP, 116, 345 106, 107, 109

Comastri, A. 2004, in Astrophysics and Space Science Library, Vol. 308, Supermassive Black Holes in the Distant Universe, ed. A. J. Barger, 245 10

Condon, J. J., Cotton, W. D., Greisen, E. W., et al. 1998, AJ, 115, 1693 53

Coppin, K., Chapin, E. L., Mortier, A. M. J., et al. 2006, MNRAS, 372, 1621 84

Cowie, L. L., Songaila, A., Hu, E. M., & Cohen, J. G. 1996, AJ, 112, 839 27, 184

Cox, T. J., Jonsson, P., Somerville, R. S., Primack, J. R., & Dekel, A. 2008, MNRAS, 384, 386 50

Croom, S. M., Richards, G. T., Shanks, T., et al. 2009, MNRAS, 399, 1755 96

Croom, S. M., Smith, R. J., Boyle, B. J., et al. 2001, MNRAS, 322, L29 105

Croom, S. M., Smith, R. J., Boyle, B. J., et al. 2004, MNRAS, 349, 1397 48

Croton, D. J., Springel, V., White, S. D. M., et al. 2006, MNRAS, 365, 11 27, 30, 184, 204, 211

Dalla Vecchia, C., Bower, R. G., Theuns, T., et al. 2004, MNRAS, 355, 995 27, 30, 184

Dalton, G. B., Caldwell, M., Ward, A. K., et al. 2006, in Society of Photo-Optical Instrumentation Engineers (SPIE) Conference Series, Vol. 6269, Soci-

ety of Photo-Optical Instrumentation Engineers (SPIE) Conference Series 44

Davis, M., Efstathiou, G., Frenk, C. S., & White, S. D. M. 1985, ApJ, 292, 371 25

Deo, R. P., Richards, G. T., Nikutta, R., et al. 2011, ApJ, 729, 108 4

Di Matteo, P., Combes, F., Melchior, A.-L., & Semelin, B. 2007, A&A, 468, 61 50

Di Matteo, T., Springel, V., & Hernquist, L. 2005, Nature, 433, 604 206

Dicken, D., Tadhunter, C., Axon, D., et al. 2012, ApJ, 745, 172 50

Dolag, K., Borgani, S., Murante, G., & Springel, V. 2009, MNRAS, 399, 497 184

Donoso, E., Li, C., Kauffmann, G., Best, P. N., & Heckman, T. M. 2010, MNRAS, 407, 1078 206, 214

Dressler, A. 1980, ApJ, 236, 351 143

Dressler, A. & Gunn, J. E. 1983, ApJ, 270, 7 32

Dunlop, J. S., McLure, R. J., Kukula, M. J., et al. 2003, MNRAS, 340, 1095 11

Elbaz, D., Hwang, H. S., Magnelli, B., et al. 2010, A&A, 518, L29 96

Ellingson, E., Green, R. F., & Yee, H. K. C. 1991, ApJ, 378, 476 35, 214

Emerson, J. P., Sutherland, W. J., McPherson, A. M., et al. 2004, The Messenger, 117, 27 106

Fabian, A. C. 2012, ARA&A, 50, 455 29, 30

Fabian, A. C., Sanders, J. S., Allen, S. W., et al. 2011, MNRAS, 418, 2154 30

Falder, J. T., Stevens, J. A., Jarvis, M. J., et al. 2011, ApJ, 735, 123 34, 185

Falder, J. T., Stevens, J. A., Jarvis, M. J., et al. 2010, MNRAS, 405, 347 14, 30, 34, 35, 36, 52, 54, 68, 87, 88, 99, 102, 153, 165, 169, 181, 185, 203, 206, 207, 211, 213, 214

Fanaroff, B. L. & Riley, J. M. 1974, MNRAS, 167, 31P 15

Fanidakis, N., Baugh, C. M., Benson, A. J., et al. 2011, MNRAS, 410, 53 208

Fanidakis, N., Maccio, A. V., Baugh, C. M., Lacey, C. G., & Frenk, C. S. 2013, ArXiv e-prints 31, 38, 181, 218

Farouki, R. & Shapiro, S. L. 1981, ApJ, 243, 32 32

Fath, E. A. 1909, Popular Astronomy, 17, 504 1

Filippenko, A. V. & Terlevich, R. 1992, ApJ, 397, L79 11

Firth, A. E., Lahav, O., & Somerville, R. S. 2003, MNRAS, 339, 1195 106

Francis, P. J., Hewett, P. C., Foltz, C. B., et al. 1991, ApJ, 373, 465 7

Freedman, W. L., Madore, B. F., Stetson, P. B., et al. 1994, ApJ, 435, L31 31

Galametz, A., Stern, D., Stanford, S. A., et al. 2010, A&A, 516, A101 34, 36, 181

Gaspari, M., Brighenti, F., & Ruszkowski, M. 2013, Astronomische Nachrichten, 334, 394 30

Gavignaud, I., Bongiorno, A., Paltani, S., et al. 2006, A&A, 457, 79 47, 110

Geach, J. E., Simpson, C., Rawlings, S., Read, A. M., & Watson, M. 2007, MNRAS, 381, 1369 190

Genzel, R., Pichon, C., Eckart, A., Gerhard, O. E., & Ott, T. 2000, MNRAS, 317, 348 3

Ghez, A. M., Salim, S., Hornstein, S. D., et al. 2005, ApJ, 620, 744 3

Goodrich, R. W. 1995, ApJ, 440, 141 18

Goodrich, R. W. & Cohen, M. H. 1992, ApJ, 391, 623 4

Graham, J., Fabian, A. C., & Sanders, J. S. 2008, MNRAS, 386, 278 30

Groth, E. J. & Peebles, P. J. E. 1977, ApJ, 217, 385 190

Gull, S. F. & Northover, K. J. E. 1973, Nature, 244, 80 30

Gunn, J. E. & Gott, III, J. R. 1972, ApJ, 176, 1 33, 184, 211, 215

Guo, Q., White, S., Boylan-Kolchin, M., et al. 2011, MNRAS, 413, 101 25

Guth, A. H. & Pi, S.-Y. 1982, Physical Review Letters, 49, 1110 24

Hardcastle, M. J. 2004, A&A, 414, 927 103, 212

Hardcastle, M. J., Ching, J. H. Y., Virdee, J. S., et al. 2013, MNRAS, 429, 2407 12

Hardcastle, M. J., Ching, J. H. Y., Virdee, J. S., et al. 2012, ArXiv e-prints 103, 212

Hardcastle, M. J., Evans, D. A., & Croston, J. H. 2007, MNRAS, 376, 1849 12

Hatch, N. A., De Breuck, C., Galametz, A., et al. 2011a, MNRAS, 410, 1537 34

Hatch, N. A., De Breuck, C., Galametz, A., et al. 2011b, MNRAS, 410, 1537 37

Heckman, T. M. 1980, A&A, 87, 152 11, 12

Heckman, T. M., Smith, E. P., Baum, S. A., et al. 1986, ApJ, 311, 526 50

Henriksen, M. J. & Mushotzky, R. F. 1986, ApJ, 302, 287 21

Hewitt, A. & Burbidge, G. 1993, ApJS, 87, 451 2

Hildebrandt, H., Arnouts, S., Capak, P., et al. 2010, A&A, 523, A31+ 107

Hine, R. G. & Longair, M. S. 1979, MNRAS, 188, 111 12, 13

Hopkins, A. M. 2004, ApJ, 615, 209 38

Hopkins, A. M. & Beacom, J. F. 2006, ApJ, 651, 142 38

Hopkins, P. F., Cox, T. J., Kereš, D., & Hernquist, L. 2008, ApJS, 175, 390 12

Hopkins, P. F., Hernquist, L., Cox, T. J., et al. 2006, ApJS, 163, 1 28, 30, 39, 216

Hoyle, F. 1953, ApJ, 118, 513 24

Hutchings, J. B., Scholz, P., & Bianchi, L. 2009, AJ, 137, 3533 34

Ilbert, O., Arnouts, S., McCracken, H. J., et al. 2006, A&A, 457, 841 143, 146

Inskip, K. J., Best, P. N., Longair, M. S., & Röttgering, H. J. A. 2005, MNRAS, 359, 1393 54

Iovino, A., McCracken, H. J., Garilli, B., et al. 2005, A&A, 442, 423 47

Irwin, M. J., Lewis, J., Hodgkin, S., et al. 2004, in Society of Photo-Optical Instrumentation Engineers (SPIE) Conference Series, Vol. 5493, Society of Photo-Optical Instrumentation Engineers (SPIE) Conference Series, ed. P. J. Quinn & A. Bridger, 411–422 45

Ivezić, Ž., Menou, K., Knapp, G. R., et al. 2002, AJ, 124, 2364 14, 53, 55, 56, 165, 168

Ivison, R. J., Dunlop, J. S., Smail, I., et al. 2000, ApJ, 542, 27 37, 184

Jackson, N. & Rawlings, S. 1997, MNRAS, 286, 241 55

Jarvis, M. J., Bonfield, D. G., Bruce, V. A., et al. 2012, ArXiv e-prints 46

Jarvis, M. J., Bonfield, D. G., Bruce, V. A., et al. 2013, MNRAS, 428, 1281 45, 121, 122, 143, 146, 147

Jarvis, M. J., Rawlings, S., Willott, C. J., et al. 2001, MNRAS, 327, 907 54, 55

Jenkins, A., Frenk, C. S., White, S. D. M., et al. 2001, MNRAS, 321, 372 27

Johansson, P. H., Naab, T., & Burkert, A. 2009, ApJ, 690, 802 26, 50

Juneau, S., Glazebrook, K., Crampton, D., et al. 2005, ApJ, 619, L135 27

Kaiser, N. & Squires, G. 1993, ApJ, 404, 441 21

Kaspi, S., Smith, P. S., Netzer, H., et al. 2000, ApJ, 533, 631 5, 207

Kataoka, J., Stawarz, Ł., Takahashi, Y., et al. 2011, ApJ, 740, 29 13

Kauffmann, G., Colberg, J. M., Diaferio, A., & White, S. D. M. 1999a, MNRAS, 303, 188 27

Kauffmann, G., Colberg, J. M., Diaferio, A., & White, S. D. M. 1999b, MNRAS, 307, 529 27

Kauffmann, G. & Haehnelt, M. 2000, MNRAS, 311, 576 32

Kauffmann, G., Heckman, T. M., & Best, P. N. 2008, MNRAS, 384, 953 204

Kauffmann, G., Heckman, T. M., Tremonti, C., et al. 2003, MNRAS, 346, 1055 29

Kauffmann, G., White, S. D. M., & Guiderdoni, B. 1993, MNRAS, 264, 201 25

Kauffmann, G., White, S. D. M., Heckman, T. M., et al. 2004, MNRAS, 353, 713 34

Kellermann, K. I., Sramek, R., Schmidt, M., Shaffer, D. B., & Green, R. 1989, AJ, 98, 1195 13

Kereš, D., Katz, N., Weinberg, D. H., & Davé, R. 2005, MNRAS, 363, 2 204

Khachikian, E. Y. & Weedman, D. W. 1974, ApJ, 192, 581 10

Khochfar, S., Emsellem, E., Serra, P., et al. 2011, MNRAS, 417, 845 25

King, A. R., Pringle, J. E., & Hofmann, J. A. 2008, MNRAS, 385, 1621 208

Knapen, J. H. 2004, in Astrophysics and Space Science Library, Vol. 319, Penetrating Bars Through Masks of Cosmic Dust, ed. D. L. Block, I. Puerari, K. C. Freeman, R. Groess, & E. K. Block, 189 29

Kotilainen, J. K. 1993, Ap&SS, 205, 107 29

Krolik, J. H. & Begelman, M. C. 1988, ApJ, 329, 702 4

Kurk, J., Cimatti, A., Zamorani, G., et al. 2009, A&A, 504, 331 141

Lacey, C. & Cole, S. 1993, MNRAS, 262, 627 24

Lacy, M., Gates, E. L., Ridgway, S. E., et al. 2002, AJ, 124, 3023 28

Lacy, M., Laurent-Muehleisen, S. A., Ridgway, S. E., Becker, R. H., & White, R. L. 2001, ApJ, 551, L17 15

Lahav, O., Naim, A., Buta, R. J., et al. 1995, Science, 267, 859 107

Laing, R. A., Jenkins, C. R., Wall, J. V., & Unger, S. W. 1994, in Astronomical Society of the Pacific Conference Series, Vol. 54, The Physics of Active Galaxies, ed. G. V. Bicknell, M. A. Dopita, & P. J. Quinn, 201 12

Laing, R. A., Riley, J. M., & Longair, M. S. 1983, MNRAS, 204, 151 54

Larson, R. B., Tinsley, B. M., & Caldwell, C. N. 1980, ApJ, 237, 692 33, 184, 211, 215

Lawrence, A., Warren, S. J., Almaini, O., et al. 2007, MNRAS, 379, 1599 106, 142

Lidman, C., Rosati, P., Tanaka, M., et al. 2008, A&A, 489, 981 141

Lintott, C. J., Schawinski, K., Slosar, A., et al. 2008, MNRAS, 389, 1179 106

Longair, M. S. & Seldner, M. 1979, MNRAS, 189, 433 16, 187

Lonsdale, C. J., Smith, H. E., Rowan-Robinson, M., et al. 2003a, PASP, 115, 897 43, 67, 79

Lonsdale, C. J., Smith, H. E., Rowan-Robinson, M., et al. 2003b, PASP, 115, 897 142

Lynden-Bell, D. 1969, Nature, 223, 690 2

Madau, P., Ferguson, H. C., Dickinson, M. E., et al. 1996, MNRAS, 283, 1388 38

Maddox, N., Hewett, P. C., Péroux, C., Nestor, D. B., & Wisotzki, L. 2012, MNRAS, 424, 2876 130, 131, 133, 134, 135, 139

Maddox, N., Hewett, P. C., Warren, S. J., & Croom, S. M. 2008, MNRAS, 386, 1605 131, 134, 135

Magorrian, J., Tremaine, S., Richstone, D., et al. 1998, AJ, 115, 2285 3, 5

Martini, P., Regan, M. W., Mulchaey, J. S., & Pogge, R. W. 2003, ApJ, 589, 774 28

Mayo, J. H., Vernet, J., De Breuck, C., et al. 2012, A&A, 539, A33 30, 36, 39, 51, 181, 213, 216

McAlpine, K., Smith, D. J. B., Jarvis, M. J., Bonfield, D. G., & Fleuren, S. 2012, MNRAS, 423, 132 164

McLure, R. J. & Dunlop, J. S. 2001a, MNRAS, 327, 199 18

McLure, R. J. & Dunlop, J. S. 2001b, MNRAS, 321, 515 35, 187, 190, 191, 202, 203, 204, 214

McLure, R. J. & Dunlop, J. S. 2002, MNRAS, 331, 795 5, 7

McLure, R. J. & Jarvis, M. J. 2004, MNRAS, 353, L45 14, 206

McLure, R. J., Kukula, M. J., Dunlop, J. S., et al. 1999, MNRAS, 308, 377 11

Mei, S., Holden, B. P., Blakeslee, J. P., et al. 2006, ApJ, 644, 759 141

Melchior, P., Sutter, P. M., Sheldon, E. S., Krause, E., & Wandelt, B. D. 2013, ArXiv e-prints 21

Merritt, D. & Ferrarese, L. 2001, MNRAS, 320, L30 7

Mihos, J. C. & Hernquist, L. 1996, ApJ, 464, 641 50

Miley, G. & De Breuck, C. 2008, A&A Rev., 15, 67 15, 34

Mo, H., van den Bosch, F. C., & White, S. 2010, Galaxy Formation and Evolution 8

Mo, H. J. & White, S. D. M. 2002, MNRAS, 336, 112 27, 184

Moore, B., Katz, N., Lake, G., Dressler, A., & Oemler, A. 1996, Nature, 379, 613 32, 184, 211, 215

Mortlock, D. J., Patel, M., Warren, S. J., et al. 2012, MNRAS, 419, 390 106

Mortlock, D. J., Patel, M., Warren, S. J., et al. 2009, A&A, 505, 97 106

Naim, A. 1995, in Bulletin of the American Astronomical Society, Vol. 27, American Astronomical Society Meeting Abstracts, 1416 107

Neistein, E., Khochfar, S., Dalla Vecchia, C., & Schaye, J. 2012, MNRAS, 421, 3579 25

Nenkova, M., Ivezić, Ž., & Elitzur, M. 2002, ApJ, 570, L9 4

Netzer, H. & Laor, A. 1993, ApJ, 404, L51 5

Nicastro, F. 2000, ApJ, 530, L65 4

Norberg, P., Baugh, C. M., Hawkins, E., et al. 2002, MNRAS, 332, 827 27

Norberg, P., Baugh, C. M., Hawkins, E., et al. 2001, MNRAS, 328, 64 30, 183

Oemler, Jr., A. 1976, ApJ, 209, 693 33, 184, 211, 215

Oke, J. B. & Gunn, J. E. 1983, ApJ, 266, 713 56

Osterbrock, D. E. 1981, ApJ, 249, 462 18

Osterbrock, D. E. 1991, Reports on Progress in Physics, 54, 579 10

Osterbrock, D. E. & Bochkarev, N. G. 1989, Soviet Ast., 33, 694 2

Osterbrock, D. E. & Mathews, W. G. 1986, ARA&A, 24, 171 4

Overzier, R. A., Bouwens, R. J., Cross, N. J. G., et al. 2008, ApJ, 673, 143 34

Overzier, R. A., Miley, G. K., Bouwens, R. J., et al. 2006, ApJ, 637, 58 34

Owen, F. N. & Ledlow, M. J. 1994, in Astronomical Society of the Pacific Conference Series, Vol. 54, The Physics of Active Galaxies, ed. G. V. Bicknell, M. A. Dopita, & P. J. Quinn, 319 15

Page, M. J., Stevens, J. A., Mittaz, J. P. D., & Carrera, F. J. 2001, Science, 294, 2516 12

Papovich, C., Momcheva, I., Willmer, C. N. A., et al. 2010, ApJ, 716, 1503 142

Peebles, P. J. E. 1982, ApJ, 263, L1 24

Peiris, H. V., Komatsu, E., Verde, L., et al. 2003, ApJS, 148, 213 24

Percival, W. J., Miller, L., McLure, R. J., & Dunlop, J. S. 2001, MNRAS, 322, 843 18

Persic, M. & Salucci, P. 1995, ApJS, 99, 501 21

Peterson, B. M. 1993, PASP, 105, 247 5

Pilbratt, G. L., Riedinger, J. R., Passvogel, T., et al. 2010, A&A, 518, L1+ 96

Poggianti, B. M., Fasano, G., Bettoni, D., et al. 2009, ApJ, 697, L137 143

Postman, M., Franx, M., Cross, N. J. G., et al. 2005, ApJ, 623, 721 143

Press, W. H. & Schechter, P. 1974, ApJ, 187, 425 19, 26

Priddey, R. S., Ivison, R. J., & Isaak, K. G. 2008, MNRAS, 383, 289 37, 184

Quilis, V., Bower, R. G., & Balogh, M. L. 2001, MNRAS, 328, 1091 27, 184

Ramos Almeida, C., Bessiere, P. S., Tadhunter, C., et al. 2013, ArXiv e-prints 203, 205, 214

Ramos Almeida, C., Tadhunter, C. N., Inskip, K. J., et al. 2011, MNRAS, 410, 1550 50

Rawlings, S., Eales, S., & Lacy, M. 2001, MNRAS, 322, 523 54, 55

Rawlings, S., Lacy, M., Sivia, D. S., & Eales, S. A. 1995, MNRAS, 274, 428 68

Reed, D. S., Bower, R., Frenk, C. S., Jenkins, A., & Theuns, T. 2007, MNRAS, 374, 2 27

Rees, M. J. 1984, ARA&A, 22, 471 7

Rengelink, R. B., Tang, Y., de Bruyn, A. G., et al. 1997, A&AS, 124, 259 53

Richards, G. T., Myers, A. D., Gray, A. G., et al. 2009, ApJS, 180, 67 105

Richards, G. T., Strauss, M. A., Fan, X., et al. 2006, AJ, 131, 2766 144

Richstone, D. O. & Schmidt, M. 1980, ApJ, 235, 361 144

Rieke, G. H., Alonso-Herrero, A., Weiner, B. J., et al. 2009, ApJ, 692, 556 51

Ripley, B. D. 1981, Spatial statistics 107

Ripley, B. D. 1988, Statistical inference for spatial processes 107

Robson, I. 1996, Active galactic nuclei 11, 12

Rosati, P., Tozzi, P., Ettori, S., et al. 2004, AJ, 127, 230 141

Rosati, P., Tozzi, P., Gobat, R., et al. 2009, A&A, 508, 583 141

Rudy, R. J. & Willner, S. P. 1983, ApJ, 267, L69 18

Saintonge, A., Tran, K., & Holden, B. P. 2008, ApJ, 685, L113 52

Salpeter, E. E. 1964, ApJ, 140, 796 2

Scannapieco, C., White, S. D. M., Springel, V., & Tissera, P. B. 2009, MNRAS, 396, 696 25

Schaye, J., Dalla Vecchia, C., Booth, C. M., et al. 2010, MNRAS, 402, 1536 25

Schechter, P. 1976, ApJ, 203, 297 188

Schmidt, G. D., Peterson, B. M., & Beaver, E. A. 1978, ApJ, 220, L31 2

Schmidt, M. 1963, Nature, 197, 1040 2, 105

Schmidt, M. & Green, R. F. 1983, ApJ, 269, 352 10, 11

Schneider, D. P., Hall, P. B., Richards, G. T., et al. 2005, AJ, 130, 367 59, 145, 146

Schödel, R., Ott, T., Genzel, R., et al. 2003, ApJ, 596, 1015 3

Seldner, M. & Peebles, P. J. E. 1978, ApJ, 225, 7 16

Serber, W., Bahcall, N., Ménard, B., & Richards, G. 2006, ApJ, 643, 68 205

Seyfert, C. K. 1943, ApJ, 97, 28 1, 10

Sheth, R. K., Mo, H. J., & Tormen, G. 2001, MNRAS, 323, 1 27

Shields, J. C. 1992, ApJ, 399, L27 11

Sijacki, D. & Springel, V. 2006, MNRAS, 366, 397 27, 184

Sikora, M., Stasińska, G., Kozieł-Wierzbowska, D., Madejski, G. M., & Asari, N. V. 2013, ApJ, 765, 62 13

Sikora, M., Stawarz, Ł., & Lasota, J.-P. 2007, ApJ, 658, 815 14, 207, 215

Silk, J. & Rees, M. J. 1998, A&A, 331, L1 29

Skrutskie, M. F., Cutri, R. M., Stiening, R., et al. 2006, AJ, 131, 1163 105

Somerville, R. S., Primack, J. R., & Faber, S. M. 2001a, MNRAS, 320, 504 23, 26

Somerville, R. S., Primack, J. R., & Faber, S. M. 2001b, MNRAS, 320, 504 27

Springel, V. 2005, MNRAS, 364, 1105 25

Springel, V., Di Matteo, T., & Hernquist, L. 2005a, ApJ, 620, L79 28

Springel, V., Di Matteo, T., & Hernquist, L. 2005b, ApJ, 620, L79 30, 39, 216

Stanford, S. A., Eisenhardt, P. R., Brodwin, M., et al. 2005, ApJ, 634, L129 141

Stanford, S. A., Romer, A. K., Sabirli, K., et al. 2006, ApJ, 646, L13 141

Stevens, J. A., Ivison, R. J., Dunlop, J. S., et al. 2003, Nature, 425, 264 37, 184

Stevens, J. A., Jarvis, M. J., Coppin, K. E. K., et al. 2010, MNRAS, 405, 2623
37, 39, 184, 216

Stevens, J. A., Page, M. J., Ivison, R. J., Smail, I., & Carrera, F. J. 2004, ApJ,
604, L17 37, 184

Stringer, M. J., Brooks, A. M., Benson, A. J., & Governato, F. 2010, MNRAS,
407, 632 25

Surace, J. A., Shupe, D. L., Fang, F., et al. 2005, in Bulletin of the American
Astronomical Society, Vol. 37, 1246 43

Tadhunter, C., Holt, J., González Delgado, R., et al. 2011, MNRAS, 412, 960 50

Tanaka, M., Finoguenov, A., & Ueda, Y. 2010, ApJ, 716, L152 142

Tanaka, M., Kodama, T., Arimoto, N., et al. 2005, MNRAS, 362, 268 143

Tchekhovskoy, A., Narayan, R., & McKinney, J. C. 2010, ApJ, 711, 50 207

Tingay, S. J., Jauncey, D. L., Reynolds, J. E., et al. 1996, in Astronomical Society
of the Pacific Conference Series, Vol. 100, Energy Transport in Radio Galaxies
and Quasars, ed. P. E. Hardee, A. H. Bridle, & J. A. Zensus, 215 16

Tregillis, I. L., Jones, T. W., & Ryu, D. 2001, ApJ, 557, 475 14

van Albada, T. S., Bahcall, J. N., Begeman, K., & Sancisi, R. 1985, ApJ, 295,
305 21, 22

van Breukelen, C., Clewley, L., Bonfield, D. G., et al. 2006, MNRAS, 373, L26

142

van Breukelen, C., Simpson, C., Rawlings, S., et al. 2009, MNRAS, 395, 11 142

Vardoulaki, E., Rawlings, S., Hill, G. J., et al. 2010, MNRAS, 401, 1709 54, 55

Venemans, B. P., McMahon, R. G., Walter, F., et al. 2012, ApJ, 751, L25 106

Venemans, B. P., McMahon, R. G., Warren, S. J., et al. 2007, MNRAS, 376, L76 106

Volonteri, M., Sikora, M., & Lasota, J.-P. 2007a, ApJ, 667, 704 14

Volonteri, M., Sikora, M., & Lasota, J.-P. 2007b, ApJ, 667, 704 208

von Hippel, T., Storrie-Lombardi, L. J., Storrie-Lombardi, M. C., & Irwin, M. J. 1994, MNRAS, 269, 97 106

Wake, D. A., Nichol, R. C., Eisenstein, D. J., et al. 2006, MNRAS, 372, 537 48

Wandel, A. 1999, ApJ, 519, L39 18

Warren, S. J., Hambly, N. C., Dye, S., et al. 2007, MNRAS, 375, 213 106

Werner, M. W., Roellig, T. L., Low, F. J., et al. 2004, ApJS, 154, 1 42

White, R. L., Helfand, D. J., Becker, R. H., Glikman, E., & de Vries, W. 2007, ApJ, 654, 99 15, 54

White, S. D. M. & Frenk, C. S. 1991, ApJ, 379, 52 25

White, S. D. M. & Rees, M. J. 1978, MNRAS, 183, 341 24, 26

Whittle, M. 2000, Seyfert Galaxies, ed. P. Murdin 10

Wiita, P. J. 2006, ArXiv Astrophysics e-prints 16

Willott, C. J., McLure, R. J., & Jarvis, M. J. 2003, ApJ, 587, L15 54, 55

Wilson, A. S. & Colbert, E. J. M. 1995, ApJ, 438, 62 207, 215

Wittman, D. M., Tyson, J. A., Kirkman, D., Dell'Antonio, I., & Bernstein, G. 2000, Nature, 405, 143 21

Wold, M., Armus, L., Neugebauer, G., Jarrett, T. H., & Lehnert, M. D. 2003,

AJ, 126, 1776 34

Wold, M., Lacy, M., Lilje, P. B., & Serjeant, S. 2001, MNRAS, 323, 231 35, 187, 203, 204, 214

Wylezalek, D., Galametz, A., Stern, D., et al. 2013, ApJ, 769, 79 34, 36, 181, 213

Yee, H. K. C. & Green, R. F. 1984, An imaging survey of fields around quasars. II - The association of galaxies with quasars 35, 214

Yee, H. K. C. & Green, R. F. 1987, ApJ, 319, 28 35

Yee, H. K. C. & López-Cruz, O. 1999, AJ, 117, 1985 191

York, D. G., Adelman, J., Anderson, Jr., J. E., et al. 2000, AJ, 120, 1579 106

Zamfir, S., Sulentic, J. W., & Marziani, P. 2008, MNRAS, 387, 856 15

Zamfir, S., Sulentic, J. W., Marziani, P., & Dultzin, D. 2007, in Bulletin of the American Astronomical Society, Vol. 39, American Astronomical Society Meeting Abstracts, 798 14

Zehavi, I., Zheng, Z., Weinberg, D. H., et al. 2005, ApJ, 630, 1 30, 183

Zel'dovich, Y. B. & Novikov, I. D. 1964, Soviet Physics Doklady, 9, 246 2

Zwicky, F. 1933, Helvetica Physica Acta, 6, 110 21